Design and Fabrication of High Speed,
Long Wavelength, Semiconductor Lasers

by

John Gilmary Wasserbauer

ECE Technical Report #94-08

Department of Electrical and Computer Engineering
University of California at Santa Barbara
March 1994

UNIVERSITY OF CALIFORNIA

Santa Barbara

Design and Fabrication of High Speed, Long Wavelength, Semiconductor Lasers

A dissertation submitted in partial satisfaction of
the requirements for the degree of

Doctor of Philosophy

in

Electrical and Computer Engineering

by

John Gilmary Wasserbauer

Committee in Charge:

Professor John E. Bowers, Chairperson

Professor Evelyn L. Hu

Professor Larry A. Coldren

Professor Nadir Dagli

The Dissertation of John Gilmary Wasserbauer
is approved

_____
Professor Evelyn L. Hu

_____
Professor Larry A. Coldren
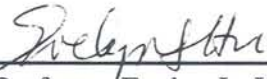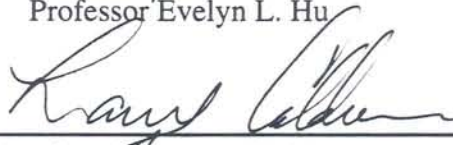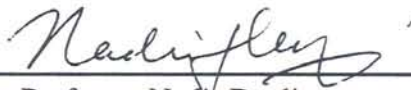
_____
Professor Nadir Dagli

_____
Professor John E. Bowers, Chairperson

March 1994

Design and Fabrication of High Speed,
Long Wavelength, Semiconductor Lasers

Electrical and Computer Engineering Department
University of California, Santa Barbara
Santa Barbara, California 93106

Acknowledgments

Figuratively speaking, good science is not done in a vacuum. Thus, I have many people to thank for helping me to produce this dissertation. Chief among them is my advisor, Professor John E. Bowers, whose time and patience were essential for me to complete this work. Prof. Bowers was especially helpful in finding funding for essential equipment and supplies and in making industry and academic collaborations possible, without which this research would never have happened. Thanks also to my Committee members, Profs. Coldren, Dagli and Hu, for the many suggestions for improving the dissertation and making sense of the results.

This dissertation incorporates the work of many theorists, including many from U. C., Santa Barbara. In particular I'd like to thank Radhakrishnan Nagarajan for many illuminating discussions on the physics of semiconductor lasers, especially those regarding his theory of carrier transport in multi-quantum well devices. Takuya Ishikawa made a major contribution with his extension of carrier transport theory to long wavelength, MQW systems and performed some excellent modeling on the lasers described herein. Scott Corzine patiently explained the intricacies of gain calculations and provided a program for calculating gain in MQW lasers. Professor. Kroemer provided useful discussions regarding heterobarrier and thermionic emission calculations. Dubravko Babic was a great general resource on device physics and superior counsel on mathematical and programming issues. I would also like to thank Greg Snider for providing a program to calculate band diagrams and Anish Goyal for much help in programming mode calculations.

Device fabrication is both an art and a science and there are many who do it well at UCSB. For invaluable help with all aspects of device fabrication I extend my

iv

To my Grandparents,
whose sacrifice and vision of a better life
has resulted in increasing levels of education and opportunity
for two generations.

Vita

18 June, 1962: Born in Cleveland, Ohio

May 1984: B.S. Materials Science and Engineering, Cornell University

September 1986: D.E.A., Electrical Engineering, École Centrale de Lyon, France

March 1994: Ph.D., Electrical Engineering, U.C., Santa Barbara

1986 - 1993: Research Assistant, Department of Electrical and Computer Engineering, University of California, Santa Barbara

Publications

1. J. E. Bowers, J. Wasserbauer, D. Crawford, S. Zehr and K. Hess, "Semi-Insulating InP Layers: Growth, Processing and Devices," INVITED PAPER, International Conference on InP and Related Materials for Advanced Electronic and Optical Devices, paper C-1, March 1989.

2. J. E. Bowers, D. L. Crawford, Y. G. Wey, R. Nagarajan, and J. Wasserbauer, "High Speed Lasers and Photodetectors," AFCEA Defense Fiber Optics Conference, INVITED PAPER, McLean, VA, March 1990.

3. J. G. Wasserbauer, T. Fukushima, J. E. Bowers, S. Zehr and R. T. Huang, "High Speed Semi-Insulating GaInAsP Laser Processing", InP and Related Materials Conference, paper TuB4, Denver, CO, April 1990.

4. T. Fukushima, J. Wasserbauer, and J. E. Bowers, "The Advantage of Compressive Strain for InGaAs/InP Multiple Quantum Well Lasers," Postdeadline paper, International Semiconductor Laser Conference, paper PD-4, Davos, Switzerland, September 1990.

5. J. Wasserbauer, T. Fukushima, J. E. Bowers, S. Zehr, and R. T. Huang, "High Speed Semi-Insulating Planar Buried Heterostructure Lasers for Microwave Transmission," DARPA/RADC Conference on Optics in Microwave Radars, Monterey, CA., December 1990.

6. J. E. Bowers, D. J. Derickson, R. J. Helkey, A. Mar, J. G. Wasserbauer, and Yih-Guei Wey, "Comb and Signal Generation Above 100 GHz Using Optoelectronics," Photonic Systems for Antenna Applications Conference, Monterey, CA, December 1991.

7. D. J. Derickson, J. G. Wasserbauer, R. J. Helkey, A. Mar, and J. E. Bowers, "A Comparison of Colliding Pulse and Self-Colliding Pulse Monolithic Cavity Mode Locked Semiconductor Lasers", paper ThB3, Optical Fiber Conference, San Jose, CA, February 1992.

8. D. J. Derickson, R. J. Helkey, A. Mar, J. G. Wasserbauer, J. E. Bowers, D. Coblentz, T. Tanbun-Ek, and R. Logan, "Comparison of Colliding Pulse and Self-Colliding Pulse Mode-Locked Semiconductor Lasers," submitted to *Elect. Lett.*, February 1992.

9. D. J. Derickson, R. J. Helkey, A. Mar, J. G. Wasserbauer, and J. E. Bowers, "Design of Multi-Section Mode-Locked Semiconductor Lasers with Intra-Waveguide Saturable Absorbers," 1992 Integrated Photonics Research Topical Meeting, paper WC3, New Orleans, LA, April 1992.

10. J. G. Wasserbauer, J. E. Bowers, M. Hafich and G. Robinson, "Specific Contact Resistivity of InGaAs/InP p-Isotype Heterojunctions", InP and Related Materials Conference, paper THP 27, Newport, RI, April 1992.

11. R. J. Helkey, D. J. Derickson, A. Mar, J. G. Wasserbauer, and J. E. Bowers, "Colliding Pulse Effects in Mode Locked Semiconductor Diode Lasers," Quantum Electronics and Laser Science Conference (CLEO), paper JThB2, Anaheim, CA, May 1992.

12. D. J. Derickson, R. J. Helkey, A. Mar, J. B. Wasserbauer, W. B. Jiang, and J. E. Bowers, "Mode-Locked Semiconductor Lasers, Short Pulse Small Package," *Optics and Photonics News*, vol. 3, no. 5, pp. 14-20, May 1992.

13. D. J. Derickson, R. J. Helkey, A. Mar, J. G. Wasserbauer, and J. E. Bowers, "Microwave and Millimeter Wave Signal Generation Using Mode-Locked Semiconductor Lasers With Intra-Waveguide Saturable Absorbers," IEEE MTT International Microwave Symposium Digest, paper V-2, pp. 753-756, Albuquerque, NM, June 1992.

14. R. J. Helkey, D. J. Derickson, J. R. Karin, A. Mar, J. G. Wasserbauer, and J. E. Bowers, "Colliding Pulse Effects in Mode-locked Semiconductor Lasers," submitted to *J. of the Optical Society of America B*, August 1992.

15. J. G. Wasserbauer, D. J. Derickson, K. Giboney, R. J. Helkey, J. R. Karin, A. Mar, and J. E. Bowers, "Integrated Optical Transmitters and Receivers Using Multi-Segment Laser Processes," IEEE Lasers and Electro-optics Society Meeting on Integrated Optoelectronics, paper ThC1, Santa Barbara, CA, August 1992.

16. R. J. Helkey, D. J. Derickson, A. Mar, J. Wasserbauer, J. E. Bowers, and R. L. Thornton, "Repetition Frequency Stabilization of Passively Mode-Locked Semiconductor Lasers," *Electron. Lett.*, vol. 28, no. 20, pp. 1920-1922, September 1992.

17. M. Ishikawa, R. Nagarajan,T. Fukushima, J. G. Wasserbauer, and J. E. Bowers, "Long Wavelength High Speed Semiconductor Lasers With Carrier Transport Effects," *J. Quantum Electron.,* vol. 28, no. 10, pp. 2230-2241, October 1992.

18. D. J. Derickson, R. J. Helkey, A. Mar, J. R. Karin, J. G. Wasserbauer, and J. E. Bowers, "Short Pulse Generation Using Multi-Segment Mode-Locked Lasers," *J. Quantum Electron.,* vol. 28, no. 10, pp. 2186-2202, October 1992.

19. D. Derickson, R. Helkey, A. Mar, J. Wasserbauer, and J. E. Bowers, "Mode-Locked Semiconductor Lasers," accepted *Microwave Journal,* November 1992.

20. R. J. Helkey, D. J. Derickson, A. Mar, J. G. Wasserbauer, J. E. Bowers, "Millimeter Wave Signal Generation Using Semiconductor Diode Lasers," *Microwave and Optical Technology Letters*, vol. 6, no. 1, pp. 1-5, January 1993.

Abstract

Design and Fabrication of High Speed,
Long Wavelength, Semiconductor Lasers

by

John Gilmary Wasserbauer

The design of high-speed InGaAsP/InP lasers operating at 1.30 and 1.55 μm is considered from two perspectives: optimization of the external parasitics and optimization of the active area.

The intrinsic limits to high-speed modulation for bulk and MQW lasers are explored with special attention paid to thermal effects, carrier transport effects and doping. Theoretical models are used to predict optimum design parameters for each case. A comprehensive approach to the design and fabrication of high speed laser diodes is outlined. Fabrication considerations for several laser structures are discussed as well as experimental optimization of some laser parameters.

Reduction of the parasitic contact resistance is achieved through evaluations of advanced metallization schemes, while reduction of the parasitic capacitance is achieved through the use of MOCVD regrown semi-insulating layers. We measure the non-negligible heterointerface resistance and show how it can be minimized through appropriate doping and/or grading of the interface.

Finally, experimental evidence for thermal, transport and doping effects are presented. Modulation bandwidths of 17 GHz for undoped MQW and 20 GHz for doped MQW lasers are demonstrated. From these results, the most promising structure for high-speed operation is identified.

Table of Contents

List of Figures

xiv

List of Tables

List Of Symbols

a	non-radiative recombination coeffecient
a_0	lattice constant
A	fractional decrease of g_0 with T
A^{**}	modified Richardson constant $(=120(m_{lh}^* + m_{hh}^*)/m_0)$
α_a	active layer absorption loss
α_c	cladding layer absorption loss
α_i	internal loss
α_m	distributed mirror loss
b	spontaneous recombination coefficient
β	spontaneous emission factor
c	Auger recombination coefficient
C_p	parallel capacitance
χ	transport factor $(=1 + \tau_{tr}/\tau_{tr})$
d	thickness of the active layer
d_{end}	width of end resistance contact
d_{fr}	etch depth per fringe
d_{SI}	thickness of the semi-insulating InP layer
D	electric flux density, proportionality constant between f_r^2 and $\sqrt{P}$
$D_{n,p,a}$	electron, hole, ambipolar diffusion coefficient
Δ	total built-in and applied voltages at a heterointerface
E	electric field
E_g	energy gap
E_f	Fermi level
E_{fc}, E_{fv}	conduction, valence band quasi-Fermi level
E_c, E_v	conduction, valence band energy level
$\Delta E_c, \Delta E_v$	bandgap discontinuity of conduction, valence band
$\delta E_c, \delta E_v$	bandgap discontinuity ratio of conduction, valence band

E_B	energy barrier height
E_t	energy of the electron trap levels
E_{odd}, E_{even}	lowest even and odd bound state energies of a two-well system
η_i	internal quantum efficiency
ε	gain compression factor, dielectric permitivity
f_r	resonance frequency
f_{tr}	transport cutoff frequency
f_{RC}	parasitic cutoff frequency
f_{3dB}	3 dB bandwidth
$f_{3dB\,max}$	maximum 3 dB bandwidth
f_c, f_v	conduction, valence band Fermi functions $(\bar{f}_v = 1 - f_v)$
G, G_0	material gain (0 - steady state)
g, g_0	material differential gain (0 - steady state)
g_{0a}	steady state material differential gain at ambient temperature
γ	damping factor
γ_0	dc offset in γ-f_r^2 relationship
Γ	optical confinement factor
h	Planck's constant
$h\nu$	photon energy
i	small signal variation of the bias current
I	bias current
I_{act}	current through the active area
I_{leak}	leakage current
I_{th}	threshold current
J, J_0	injected current density
J_n, J_p	electron, hole current density
J_{nom}	nominal current density
J_{th}	threshold current density
$J_{thermionic}$	thermionic emission current density

k	Bolzmann constant
K	K factor, proportionality constant between γ and f_r^2
l	degeneracy of the trap level E_t
L	cavity length, gap width for TLM patterns
L_w	quantum well width
L_U, L_1, L_2	undoped layer thickness
L_s	series inductance
L_t	transfer length
L_x	x-axis intercept of TLM plot
λ	wavelength
λ_0	laser emission wavelength
$\lambda_{barrier}$	barrier material wavelength
λ_{SCH}	SCH material wavelength
m^*	effective mass
m_0	rest mass of the electron
m_c^*, m_v^*	conduction, valence band effective mass
m_{lh}^*, m_{hh}^*	light hole, heavy hole effective mass
$\mu_{n,p}$	electron, hole mobility
n_r	refractive index
n	carrier (electron) density, small signal variation of electron number
N, N_0	electron number in active area (0 - steady state)
n_{th}	threshold carrier density
n_{tr}	transparency carrier density
n_{loss}	optical loss carrier density ($n_{loss} = n_{th} - n_{tr}$)
N_t	electron trap density
N_A	acceptor concentration
N_d	background electron concentration
ω	angular frequency
ω_r	angular resonance frequency

p	hole concentration
P, P_0	output power per facet (0 - steady state)
P_{max}	maximum dc output power
Φ_{Bp}	height of the valence band barrier at a metal-semiconductor interface
Ψ	band bending parameter
π	pi (= 3.1415926)
q	electron charge
r_c	specific contact resistance
r_i	specific interface resistance
R	mirror reflectivity, resistance
R_c	contact resistance
R_e	resistance of the InP between TLM contacts
R_{end}	end resistance
R_L	diode resistance per unit length
R_s	series resistance, sheet resistance
R_{sc}	sheet resistance of the conducting layer underneath TLM contacts
R_{th}	thermal resistance
ρ	bulk resistivity
ρ_c, ρ_v	conduction, valence band density of states
s	small signal variation of the total photon number
s_n	small signal amplitude of white noise source
S, S_0	total photon number (0 - steady state)
S', S_0'	photon density (0 - steady state)
S_n	white noise photon number
t_{well}	quantum well thickness
$t_{barrier}$	barrier thickness
t_{SCH}	SCH thickness
T	temperature
T_a	ambient temperature
T_0	threshold current characteristic temperature

Chapter 1
Introduction

1.1 Background

Since their invention some 30 years ago semiconductor lasers have carved an important niche in the field of fiber optic telecommunications. Their compact size, reliability and ease of modulation make them ideal sources for both local and long-distance applications. Both GaAs and InP-based lasers have found widespread use in the laboratory and in industry. While GaAs lasers are well suited for short-haul or multimode fiber systems, InP is the material of choice for medium and long-haul, high bit-rate systems. This is due to the fact that InGaAsP/InP lasers can produce emission wavelengths of 1.3 and 1.55 μm, which are the minimum dispersion and minimum attenuation windows of single mode optical fibers, respectively. With the advent of dispersion shifted fiber and erbium-doped amplifiers, the operating wavelength of 1.55 μm has taken on additional importance.

Almost from the start, single mode optical fibers have fulfilled their promise of nearly limitless bandwidth; that is, the amount of information that may be transmitted through them per unit time. The challenge to researchers and engineers has been to develop lasers that can utilize more and more of that capacity. Thus, InGaAsP/InP lasers have been the subject of intense research. The goal of this research has been to improve the ability to directly modulate these lasers at high speed.

1

1.2 Limits to High Speed Operation

In designing high speed lasers there are many parameters which must be optimized simultaneously. These parameters may be grouped into two general categories, extrinsic and intrinsic. The traditional definition of extrinsic with regard to semiconductor lasers is more or less all things that affect the external parasitics. This includes such parameters as electrical parasitics, current confinement, and thermal impedance. The intrinsic parameters are those material and structural parameters which affect the resonance frequency, such as photon density, differential gain, gain compression and photon lifetime. For the purposes of organization we will arbitrarily label as intrinsic everything that has to do with the active area, and extrinsic everything outside of the active area. This definition is not perfectly precise, however, since parameters such as the optical confinement factor and the waveguide loss depend on the composition of the active area as well as the surrounding material. Parameters such as these, which cross the line between extrinsic and intrinsic, will be grouped along with the extrinsic parameters.

The five main limits to the speed of any semiconductor laser, whether bulk or quantum well, are (1) electrical parasitics, (2) current leakage, (3) thermal heating, (4) gain compression due to optical non-linearity and (5) transport effects. Figure 1.1 illustrates the complex interaction between the causes and the effects that reduce the overall modulation bandwidth.

We consider first the extrinsic device. Many laser designs are limited by electrical parasitics, namely the parallel combination of diode resistance and parasitic capacitance. The main sources of diode resistance are the metal/semiconductor contact resistance, the p-cladding layer resistance and the resistance due to

Causes	Effects
Electrical Parasitics ──────►	Low Frequency Rolloff
Current Leakage	Reduced Photon Density*
Thermal Effects	Increased Threshold*
Undoped Layer Diffusion†	Reduced Differential Gain*
Thermionic Emission†	
Non-uniform Injection†	
Gain Compression ──────►	Increased Damping
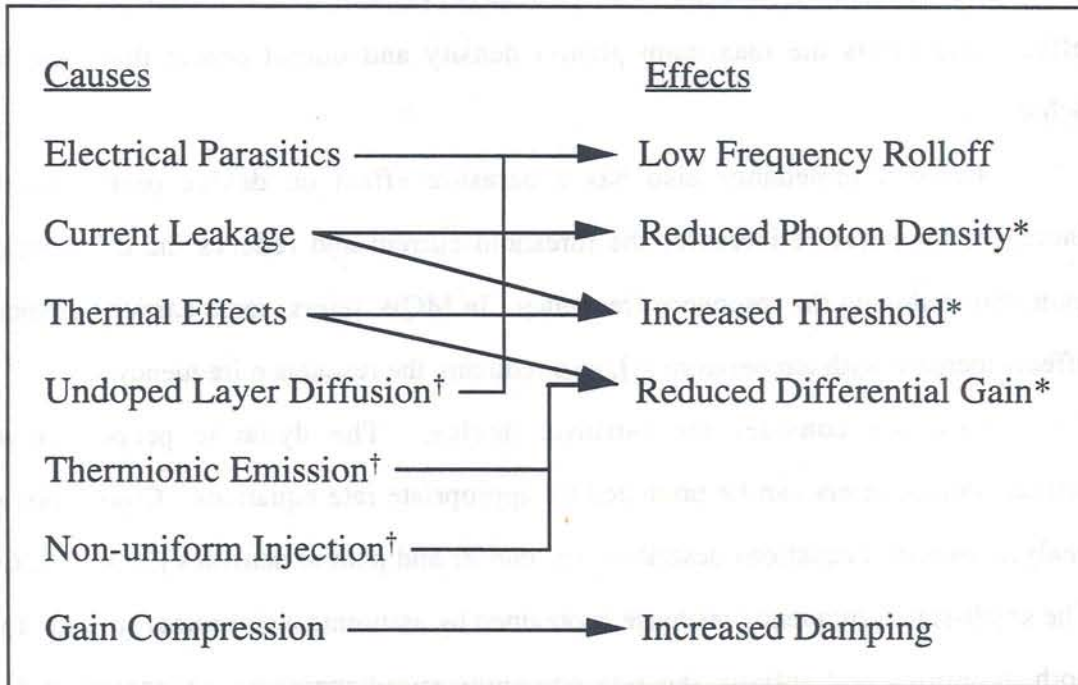
Figure 1.1   The relationships between causes and effects resulting in limited modulation bandwidth in semiconductor lasers. † Carrier transport processes and effects. * Effects which directly reduce the resonance frequency. Note: To a minor degree, gain compression also reduces the resonance frequency directly. Its major effect, however, is on the damping.

heterointerfaces. Additional resistance can come from the substrate and n-side contact, although in most cases these are negligible. The principal sources of parasitic capacitance are the contact to substrate capacitance and the depletion capacitance of reverse biased p-n junctions. Minor additional sources include the diffusion capacitance of the active area and the space-charge capacitance. The laser packaging may add additional resistance or capacitance and also inductance.

Current leakage may be considered an external parasitic. Current which circumvents or escapes the active area raises the threshold current, increases thermal

3

effects and limits the maximum photon density and output power that may be achieved.

Thermal impedance also has a parasitic effect on device performance. Increased temperature increases the threshold current and reduces the differential gain, thus reducing the resonance frequency. In MQW lasers, some carrier transport effects increase with temperature [1], also reducing the resonance frequency.

Next we consider the intrinsic device. The dynamic properties of semiconductor lasers can be predicted by appropriate rate equations. Conventional analysis uses two equations describing the carrier and photon densities [2, 3, 4, 5, 6]. The small-signal frequency response is obtained by assuming a sinusoidal solution for both quantities and solving the rate equations simultaneously. A second order transfer function may then be written between the small-signal input current and the small-signal photon density. The transfer function exhibits a characteristic resonance frequency and damping rate, which may be written in terms of the intrinsic device parameters [1],

$$f_r = \frac{1}{2\pi} \sqrt{\frac{g_0 S_0'}{\tau_p (1 + \varepsilon S_0')}}$$

$$\gamma = \frac{g_0 S_0'}{(1 + \varepsilon S_0')} + \frac{\varepsilon S_0'}{\tau_p (1 + \varepsilon S_0')}.$$

where g_0 is the material differential gain, S_0' is the photon density, τ_p is the cavity photon lifetime, and ε is the gain compression factor. The gain compression factor phenomenologically describes the saturation of gain (and differential gain) at high photon densities. Gain compression has been attributed primarily to spectral hole burning [7, 8, 9], and transient carrier heating [10, 11]. Neglecting external parasitics,

4

the 3 dB modulation bandwidth is proportional to the ratio of the square of the resonance frequency to the damping rate. This proportionality constant is commonly referred to as the K factor [12], and is given by $K = 4\pi^2(\tau_p + \varepsilon/g_0)$. The maximum modulation bandwidth is then given as $f_{3dB\,max} = 8.8/K$. From the above relations we see that high differential gain, large photon density, small photon lifetime and small gain compression factor are desirable for large modulation bandwidths.

In addition to gain compression effects, quantum well lasers may be subject to carrier transport effects [13]. The physical processes of diffusion, tunneling and thermionic emission can lead to a reduction in the effective or dynamic differential gain. Further, multi-quantum well (MQW) lasers may suffer from non-uniform carrier injection, causing additional reduction in the overall differential gain [1].

1.3 Dissertation Organization

In addition to this introduction, this dissertation is organized into five chapters and an appendix.

Chapter 2 examines each of the limits to high speed operation in detail. For each case a design approach to maximizing the modulation bandwidth is outlined. Electrical parasitics are examined first, followed by transverse and lateral device parameters. Next, the longitudinal device is considered. A resonance frequency model is developed which includes thermal and current leakage effects. This model is used to calculated the 3 dB bandwidth as a function of cavity length. The model shows that there exists an optimum cavity length for maximum modulation bandwidth and that its value is different for bulk and MQW laser structures.

A review of the current theories of high speed modulation of semiconductor lasers is then presented, with particular attention paid to the intrinsic limits of

modulation bandwidth. First the various models proposed to explain enhanced gain compression and the effects of transport are listed. A more detailed discussion of transport theory follows in Section 2.6, including the analytic solution applied to a single quantum well laser. The implications of transport theory for relative intensity noise and the relationship between damping and resonance frequency are discussed in Section 2.7. Transport theory is then extended to multi-quantum well devices and its implications for the optimization of active area design for high-speed modulation are discussed. In Section 2.10 the effects of doping the active layer on the performance of InGaAsP/InP lasers is discussed. Here the theoretical and experimental basis for the observed improvement of modulation bandwidth with doping is described. Finally, the effects of doping on the problems of carrier transport and non-uniform injection are considered qualitatively. Figure 1.2 summarizes the present approach to high speed laser design.

Chapter 3 addresses the issues of parasitic capacitance and current leakage. The problem of minimizing these two design parameters simultaneously hinges on the science and technology of semi-insulating InP expitaxy. As the understanding and quality of semi-insulating material has improved, the design of lasers employing semi-insulating current blocking layers has evolved considerably. For this reason, a review is given of the current understanding of carrier transport and dopant diffusion processes in SI InP material. Armed with this knowledge, the advantages and disadvantages of the various laser designs are discussed. Finally, we describe the fabrication process for an advanced laser design, the cap mesa buried heterostructure (CMBH) laser.

Extrinsic Device	Intrinsic Device
Low Parasitics	High Differential Gain
Low Contact Resistance	Quantum Well Active Areas
Low Heterojunction Resistance	Strain
Low Parasitic Capacitance	p-Type Active Area Doping
Small Current Leakage	High Photon Density
Appropriate Blocking Layer Structure	Small Cavity Volume
	Strong Index Guiding
Good Regrowth	Short Photon Lifetime
Small Thermal Effects	Short Cavity Length
Small Electrical Resistance	Reduced Transport Effects
Small Thermal Resistance	QW and SCH Optimization
Low Threshold	p-Type Active Area Doping

Figure 1.2   High speed laser requirements and some practical approaches.

We begin Chapter 4 with a discussion of the primary requirements of ohmic contacts to p-type InP and related materials. In the following three sections we describe three important approaches to achieving low resistance, ohmic contacts and use the transmission line method to characterize them. First we consider an alloy of Au and Be (0.9% Be) as a replacement for alloys of Au and Zn (typically 5 - 10% Zn) as a general purpose contact metal. For InGaAs contact layers two other metallizations are investigated: a Pd/Zn sandwich for layers in which additional doping is needed, and Ti/Pt for layers with very high doping. The correlation between contact microstructure and specific contact resistance, r_c, will be explored in all three cases.

Another potential source of series resistance is the heterojunction between the contact and cladding layers of a laser. The second part of Chapter 4 addresses this issue by using a variation of the transmission line method to measure the specific interface resistance, r_i. It is found experimentally that a large increase in r_c occurs when the current is forced through the heterojunction. This increase is attributed to the specific interface resistance. The dependence of r_i on the doping and grading of the heterojunction is also investigated. A theoretical model based on thermionic emission is developed and used to explain these results. These results have particular importance for high-speed *p-i-n* photodetectors and vertical cavity surface emitting lasers, where carrier transport across heterobarriers can have highly detrimental effects.

Chapter 5 presents the measured and theoretical results as the investigation has proceeded from external parasitics to intrinsic device design. The approach has been to first reduce the device parasitics so as to be able to study other high-speed limitations. Only then have other limits, such as carrier transport effects, become observable. A method of overcoming transport limitations by uniform doping of the active area is explored. The focus then turns to the optimization of the cavity length for high-speed operation. A remarkable difference in the modulation bandwidth dependence on cavity length is observed between bulk and MQW designs. Finally, the cavity length optimized bulk and multi-quantum well active area lasers are compared as directly as possible to determine the best possible structure for high speed operation.

Chapter 6 concludes this work and offers some view on the best possible structure for the realization of high-speed semiconductor lasers in the InGaAsP

system. Some thoughts are given for future theoretical and experimental investigation in this subject.

The Appendix gives a brief review of the transmission line model (TLM) for ohmic contacts. This model is used extensively in Chapter 4 to measure the specific contact resistance and forms the basis for a technique used to measure the specific heterointerface resistance.

References

1. M. Ishikawa, T. Fukushima, R. Nagarajan, and J. E. Bowers, "Temperature Dependence of Damping in High-Speed Quantum-Well Lasers", *Appl. Phys. Lett.*, vol. 61, pp. 396-398, 1992.

2. R. S. Tucker, "High-Speed Modulation of Semiconductor Lasers," *J. Lightwave Technol.*, vol. 21, pp. 1180-1192, 1985.

3. K. Y. Lau, and A. Yariv, "Ultra-High Speed Semiconductor Lasers," *J. Quantum Electron.*, vol. 21, pp. 121-138, 1985.

4. C. B. Su and V. A. Lanzisera, "Ultra-High-Speed Modulation of 1.3 μm InGaAsP Diode Lasers," *J. Quantum Electron.*, vol. 22, pp. 1568-1578, 1986.

5. J. E. Bowers, "High Speed Semiconductor Laser Design and Performance," *Solid-State Electron.*, vol. 30, pp. 1-11, 1987.

6. G. P. Agrawal, "Effect of Gain and Index Nonlinearities on Single-Mode Dynamics in Semiconductor Lasers," *J. Quantum Electron.*, vol. 26, pp. 1901-1909, 1990.

7. G. P. Agrawal, "Effect of Nonlinear Gain on Single-Frequency Behaviour of Semiconductor Lasers," *Electron. Lett.*, vol. 22, pp. 696-670, 1986.

8. M. Asada, and Y. Suematsu, "Density-Matrix Theory of Semiconductor Lasers with Relaxation Broadening Model - Gain and Gain Suppression in Semiconductor Lasers," *IEEE J. Quantum Electron.*, vol. QE-21, pp. 434-442, 1985.

9. R. Olshansky, D. M. Fye, J. Manning, and C. B. Su, "Effect of Nonlinear Gain on the Bandwidth of Semiconductor Lasers," *Electron. Lett.,* vol. 21, pp. 496-497, 1985.

10. M. P. Kesler and E. P. Ippen, "Subpicosecond Gain Dynamics in GaAlAs Laser Diodes," *Appl. Phys. Lett.*, vol. 51, pp. 1765-1767, 1987.

11. B. Gomatam, and A. P. DeFonzo, "Theory of Hot Carrier Effects on Nonlinear Gain in GaAs-AlGaAs Lasers and Amplifiers," *J. Quantum Electron.*, vol. 26, pp. 1689-1704, 1990.

12. R. Olshansky, P. Hill, V. Lanzisera, and W. Powazinik, "Universal Relationship Between Resonant Frequency and Damping Rate of 1.3 μm InGaAsP Semiconductor Lasers," *Appl. Phys. Lett.*, vol. 50, pp. 653-655, 1987.

13. R. Nagarajan, T. Fukushima, S. W. Corzine, and J. E. Bowers, "Effects of Carrier Transport on High Speed Quantum Well Lasers," *Appl. Phys. Lett.*, vol. 59, pp. 1835-1837, 1991.

Chapter 2

Extrinsic and Intrinsic Modulation Limits and Overall Design Approach

2.1 Electrical Parasitics

One of the main causes of limited modulation bandwidth common to all types of semiconductor lasers is electrical parasitics. In the simplest model of a laser diode [1], electrical parasitics cause a rolloff in the frequency response which may be written as

$$M(\omega) = \left(\frac{1}{1 + j\omega\tau_{RC}} \right),$$

where $\tau_{RC} = 1/R_s C_p$ and R_s and C_p are the series resistance and parallel capacitance of the laser diode, respectively. A characteristic 3 dB rolloff frequency may then be derived as

$$f_{3dB} = \frac{1}{2\pi R_s C_p}.$$

The major sources of series resistance include p-contact and heterobarrier resistance and p-cladding resistance. The major sources of parallel capacitance are the bondpad and blocking layer capacitances. One of the major thrusts of this research has been to reduce the device parasitics in order to be able to observe and address the other fundamental limitations of high-speed lasers, such as carrier transport effects.

For a 3 dB parasitic frequency of greater than 30 GHz, typical values of C_p must be below 1 pF while R_s values should be limited to less than 5 Ω. The approach

12

used to reduce the parasitic capacitance problem is to minimize bondpad areas, employ thick dielectric layers and replace high-capacitance, reverse-biased *p-n* junctions with low-capacitance, semi-insulating layers. Semi-insulating layers and parasitic capacitance reduction are treated in detail in Chapter 3. The approach used in this work to reducing the parasitic resistance problem is both structural, such as designing lasers with wide contact layers, and material, such as investigating various metallizations and doping schemes. Also investigated is the resistance of the heterointerface between *p*-contact and cladding layers. For the first time the magnitude of the specific interface resistance is measured and it is shown how this can be minimized. Contact and heterointerface resistance are treated in detail in Chapter 4.

In practice, the electrical parasitics of the laser mount must also be taken into account in order to avoid further degradation of the modulation response. In particular, the inductance of the bondwire between the laser and microwave transmission line must be minimized. The total parasitic inductance must be limited to 0.5 nH for the parasitic frequency limit to exceed 20 GHz. A well designed and carefully fabricated laser mount can avoid these problems to a large degree. Some methods of achieving this are given in Chapter 3.

2.2 Lateral and Transverse Device Structure

A subset of all extrinsic parameters directly affect the resonance frequency, which, without parasitic or transport limits, is directly proportional to the modulation bandwidth. Neglecting carrier transport, gain compression, and current leakage the expression for angular resonance frequency is written [2]

13

$$\omega_r^2 = g_0 \eta_i \frac{\Gamma}{dwL} \frac{(I - I_{th})}{q} = 2 \frac{g_0}{hv} \frac{\Gamma}{V} \frac{(\alpha_m + \alpha_i)}{\alpha_m} P,$$

In the expression on the near right, ω_r has been written in terms of the bias current above threshold, $I - I_{th}$. Here, η_i is the internal quantum efficiency, Γ is the optical confinement factor, d and w are the active layer thickness and width, respectively, L is the cavity length ($V = dwL$), and q is the electron charge. On the far right, ω_r has been written in terms of the output power per facet, P. α_i and α_m are the distributed internal and mirror losses, respectively, and hv is the photon energy. The majority of the terms in the above expressions are interdependent. For the moment we will focus exclusively on the terms which depend on the lateral and transverse dimensions of the waveguide. We now discuss how each of these terms varies with d and w, and then describe how they may be optimized together to increase the maximum resonance frequency of the laser.

The confinement factor, Γ, depends heavily on the choice of active and cladding materials as well as on the thickness and width of the active area. In general, Γ increases with d and w. Γ also depends heavily on the type of waveguide structure used, and is typically an order of magnitude larger for strongly index guided structures than for weakly index guided or gain guided structures. We therefore restrict our attention to buried heterostructures in which the active area is surrounded on all sides by low index InP material.

The distributed internal loss, α_i, depends heavily on the confinement factor, and therefore on all of the variables mentioned above. In the limit of small absorption, α_i may be written

$$\alpha_i = \Gamma \alpha_a + (1 - \Gamma) \alpha_c,$$

14

where α_a and α_c are the active layer and cladding layer absorption losses, respectively. It should be noted that the absorption losses are a sensitive function of wavelength, bandgap, and doping. Furthermore, Koren *et al.* [3] have noted that α_i is dependent on carrier density, and therefore is also a function of L. In either case, the equation for internal loss predicts that the internal loss drops considerably as the waveguide dimensions are reduced. This trend has been confirmed experimentally [3].

The distributed mirror losses, α_m, depend heavily on the length of the cavity, L, and, to a lesser extent, on the mirror reflectivities, R. For equal mirror reflectivities the expression for mirror loss is written,

$$\alpha_m = \frac{1}{L}\ln\left(\frac{1}{R}\right).$$

The mirror reflectivity varies only slightly with the effective index of the waveguide, which depends on the same parameters as the confinement factor. Thus, the major factor in determining α_m is the cavity length.

The threshold current, I_{th}, depends on all of the aforementioned parameters in a nonlinear fashion. A qualitative understanding of these results may be obtained by linearizing the gain near threshold. In a simplified treatment Bowers and Wilt [4] have shown that the threshold current may be approximated by

$$I_{th} = dwL\left[\frac{B}{A} + \frac{\alpha_i + \alpha_m}{A\Gamma} + 0.4\left(\frac{B}{A} + \frac{\alpha_i + \alpha_m}{A\Gamma}\right)^{3/2}\right],$$

where A and B are constants related to the linear gain. Typical values of A and B are 0.05 cm-μm/A and 100 cm^{-1}, respectively. The model assumes no non-radiative recombination due to surface states and defects, no scattering losses, and no Auger

15

recombination in the SCH or barrier layers. Note that the threshold current is directly proportional to the volume of the active area. Thus, the threshold current is expected to decrease with decreasing d and w until the point where the confinement factor becomes too small, at which point the threshold current begins to increase. A good waveguide design balances these two factors in order to minimize I_{th}.

In summary, good lateral and transverse waveguide design for high speed lasers must take into account many interrelated factors. From the preceding discussion we can define a figure of merit for the design of the lateral and transverse waveguide dimensions. For a specific cavity length, d and w may be optimized together by maximizing the term

$$\frac{\Gamma}{dwI_{th}}.$$

Although the threshold current is directly proportional to L, the optimum values of d and w for high speed operation will not change considerably with cavity length. The above term ignores the effects of device resistance, which may cause parasitic and thermal effects which reduce the overall modulation bandwidth. These effects will be included in the next section. We now explore the effects of cavity length and mirror loss, which greatly influence the attainable values of resonance frequency.

2.3 Cavity Length and Mirror Loss

It has been shown that the maximum relaxation oscillation frequency for a laser can be increased through the use of high reflectivity mirrors [5, 6]. The decrease in I_{th} caused by higher facet reflectivities results in higher obtainable values of $I - I_{th}$ and therefore results in increased resonance frequencies. However, significant improvements in the resonance frequency occur only near threshold, where the effect

16

of lowering I_{th} is greatest. At current levels of many times the threshold value, the relative improvement of ω_0 due to $I - I_{th}$ becomes very small. Conversely, lowering the facet reflectivity will increase I_{th}, thus reducing the obtainable values of $I - I_{th}$. Using a temperature and current leakage dependent model, Cheng *et al.* [7] have shown that the typical as-cleaved InP facet reflectivity of 0.30 is very close to ideal for high-speed lasers and that only a marginal improvement in bandwidth can be achieved by applying coatings.

The cavity length, L, may be shortened to decrease the photon lifetime and increase the photon density. This has been demonstrated experimentally for bulk lasers where the highest modulation bandwidths to date for 1.3 μm bulk lasers have been obtained with cavity lengths of 100 - 130 μm [8]. However, as the distributed mirror losses increase, the threshold gain increases and the differential gain is reduced. The competition between photon lifetime and differential gain leads to an optimum cavity length for high speed operation. Since the gain versus carrier density characteristics are different for bulk and QW lasers, the optimum cavity lengths for maximum bandwidth will also differ. In the remainder of this section we will model this behavior empirically.

The following model is an adaptation and extension of the work done by Cheng *et al.* [7]. The cavity length and temperature dependent threshold current may be expressed phenomenologically as

$$I_{th}(L,T) = I_{th0}(L)f(T),$$

where $I_{th0}(L) = I_{th}(L,T_a)/f(T_a)$ and T_a is the ambient temperature. $f(T)$ may be written as

$$f(T) = \exp\left(\frac{T_a + IVR_{th}}{T_0}\right),$$

where I is the total current passing through the device, V is the total voltage across the device, R_{th} is the thermal resistance, and T_0 is the characteristic temperature of the threshold current. The total current passing through the diode is simply $I = I_{act} + I_{leak}$. Assuming the leakage path acts like a diode in parallel with the active area, the leakage current may be expressed as

$$I_{leak} = I\left[1 - \exp(-V/V_L)\right],$$

where $V = V_{th} + IR_s$. V_L is the characteristic turn-on voltage of the leakage current, V_{th} is the threshold voltage and R_s is the series resistance. To fully account for the effect of cavity length we write the device resistance as

$$R_s = R_{s,300}\left(\frac{300\mu m}{L}\right),$$

where $R_{s,300}$ is chosen arbitrarily to be 6 Ω.

The temperature and injected current dependent differential gain may be written as

$$g_0 = g_{0a}f(T)f(I_{th}),$$

where g_{0a} is the differential gain at ambient temperature, $f(T)$ is the temperature dependence and $f(I_{th})$ the threshold current dependence of the differential gain. $f(T)$ may be written as [7]

$$f(T) = 1 - AIVR_{th}.$$

where A is a constant. In general, $f(I_{th})$ is a complex function of the injected current. Figure 2.1 (a) shows the material gain and differential gain of bulk and single quantum well active areas as functions of the nominal current density, J_{nom},

18
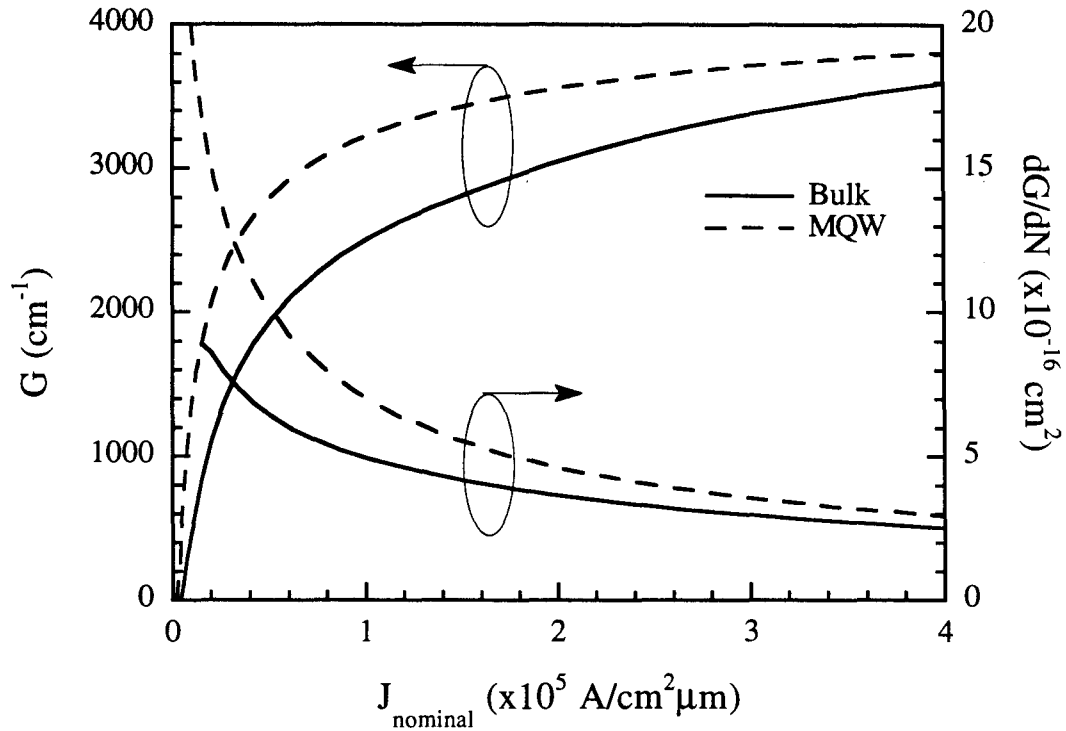
Figure 2.1 (a) Calculated dependence of gain and differential gain on nominal current density for
bulk and MQW structures.

calculated according to References [9] (bulk) and [10] (SQW). The threshold current
may be calculated from the gain data through the use of the threshold condition,

$$G\Gamma = \alpha_i + \alpha_m,$$

where G is the material gain. The variation of threshold current with cavity length
calculated from the gain data of Figure 2.1 (a) is shown in Figure 2.1 (b). In
comparing the two gain curves of Figure 2.1 (a) we find that the gain for quantum
well lasers rises more quickly at low bias currents and saturates at lower relative bias
currents than the gain for the bulk active area. This is due to the splitting of the hole
degeneracy in the valence band and the effect of strain leading to a more symmetric
density of states between conduction and valence bands. The material differential

19
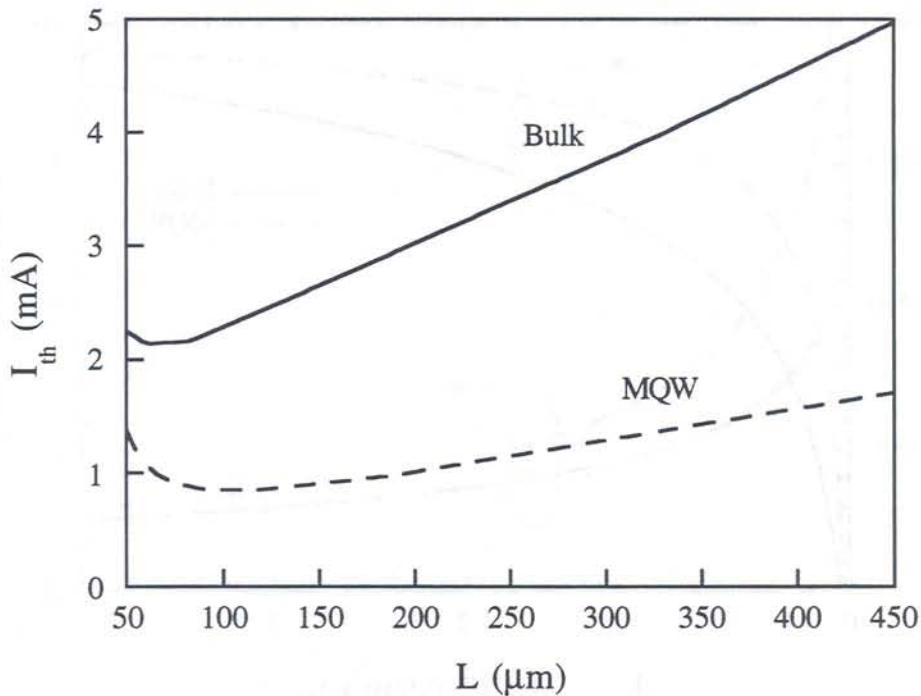
Figure 2.1 (b)   Calculated threshold current versus cavity length for bulk and MQW structures.

gain corresponding to these gain curves is also shown in Figure 2.1. It decreases

sublinearly with increasing nominal current density. For bulk lasers the g_0 is

approximately proportional to $1/I_{th}$. For MQW lasers $f(I_{th})$ is more complex. In the

following calculations the actual calculated gain data are used to determine both J_{nom}

and g_0 for each structure.

Using these equations the resonance frequency may be calculated for any

given current density. The parameters used in the calculation are given in Table 2.1.

Figure 2.2 shows the calculated power and resonance frequencies of both bulk and

MQW lasers as a function of bias current. The bulk laser structure consisted of a 100

nm active area (λ = 1.55 µm) and symmetric SCH layers of 100 nm each (λ = 1.30

µm). The MQW laser structure consisted of seven, 8.6 nm wells with 1%

compressive strain ($In_{0.79}Ga_{0.21}As_{0.75}P_{0.25}$), 8 nm barriers ($\lambda$ = 1.25 µm) and 100 nm

20

symmetric SCH layers ($\lambda = 1.25$ μm). For both bulk and MQW lasers the peak in the resonance frequency curve occurs well before the power output saturates. This is due to the reduction in differential gain and the increase in leakage current as the power output is increased. Furthermore, the peak resonance frequency for MQW lasers occurs at a lower bias current than for bulk lasers. This is due to the greater sensitivity of the MQW differential gain to the injected carrier concentration.

Parameter	Symbol	Value
Operation Wavelength	λ_0	1.55 μm
Active Region Width	w	1.0 μm
Mirror Reflectivity	R	0.30
Active Area Loss	α_a	30 cm^{-1}
Cladding Layer Loss	α_c	5 cm^{-1}
Gain Compression Factor	ε	2.4×10^{-17} cm^{-3}
Series Resistance @ 300 μm	R_s	6 Ω
Thermal Resistance @ 300 μm	R_{th}	100 K/W
Voltage at Threshold	V_{th}	1.5 V
Leakage Turn-On Voltage	V_L	2.7 V
Ambient Temperature	T_a	300 K^{-1}
Characteristic Temperature	T_0	60 K^{-1}
Fractional Decrease of g_0 with Temperature	A	3×10^{-3} K^{-1}
Optical Confinement Factor for Bulk, MQW	Γ	0.20, 0.11

Table 2.1   Typical values of the parameters used in the calculated modulation response of Figures 2.2 and 2.3.

21
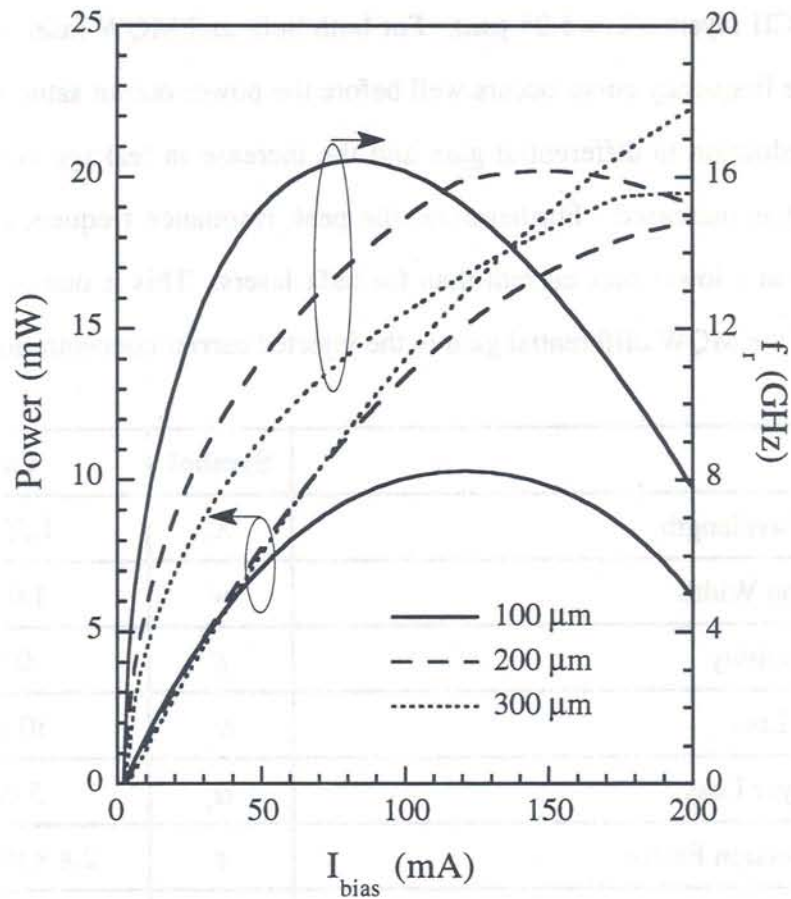
Figure 2.2 (a) Calculated power output and resonance frequency as a function of dc bias current for bulk lasers of various cavity lengths.

We now investigate the effect of cavity length on the resonance frequency of the laser. It will be shown that, due to the nature of the gain curves, the optimum cavity length for MQW lasers is longer than that of bulk lasers. Figure 2.3 illustrates the effect of cavity length on resonance frequency for both bulk and MQW lasers. The points have been taken at optimum output power for each cavity length. The optimum cavity length for the bulk laser is less than 100 μm, whereas the optimum cavity length for the MQW laser is over 100 μm. Note that the optimum cavity length
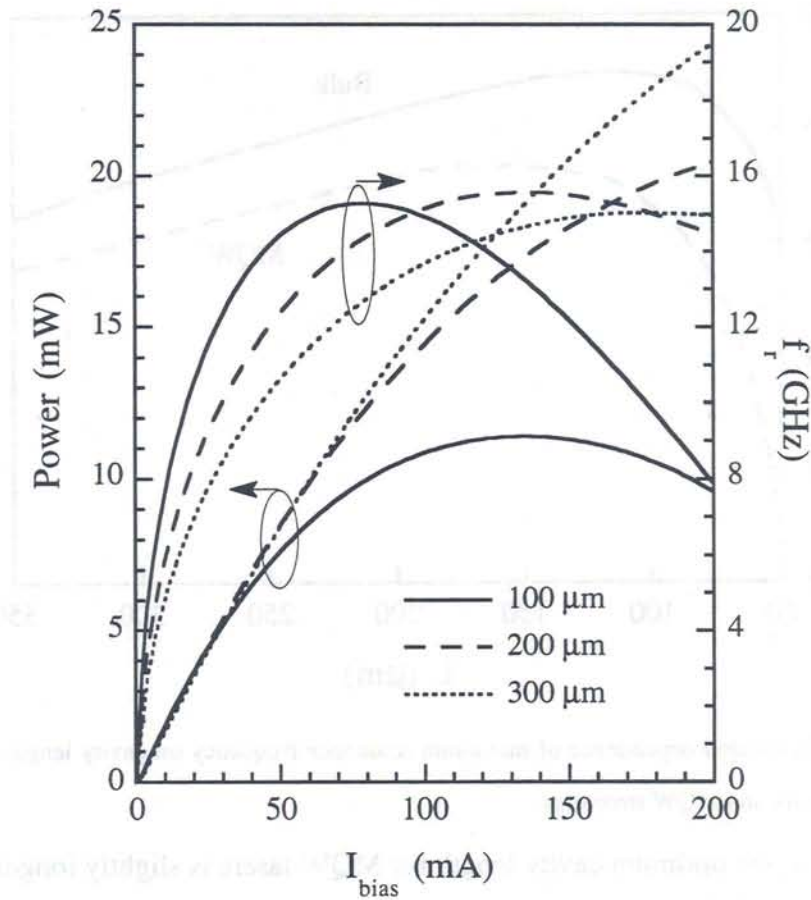
Figure 2.2 (b) Calculated power output and resonance frequency as a function of dc bias current for

MQW lasers of various cavity lengths.

corresponds roughly to the minimum in the respective threshold current for each

structure.

In summary, the resonance frequency of the laser is dependent on the mirror

reflectivity and cavity length. While increasing the mirror reflectivity can provide

some improvement in the resonance frequency near threshold, the optimum value for

the maximum resonance frequency remains near the as-cleaved value of

approximately 0.3. Due to the difference in differential gain and threshold
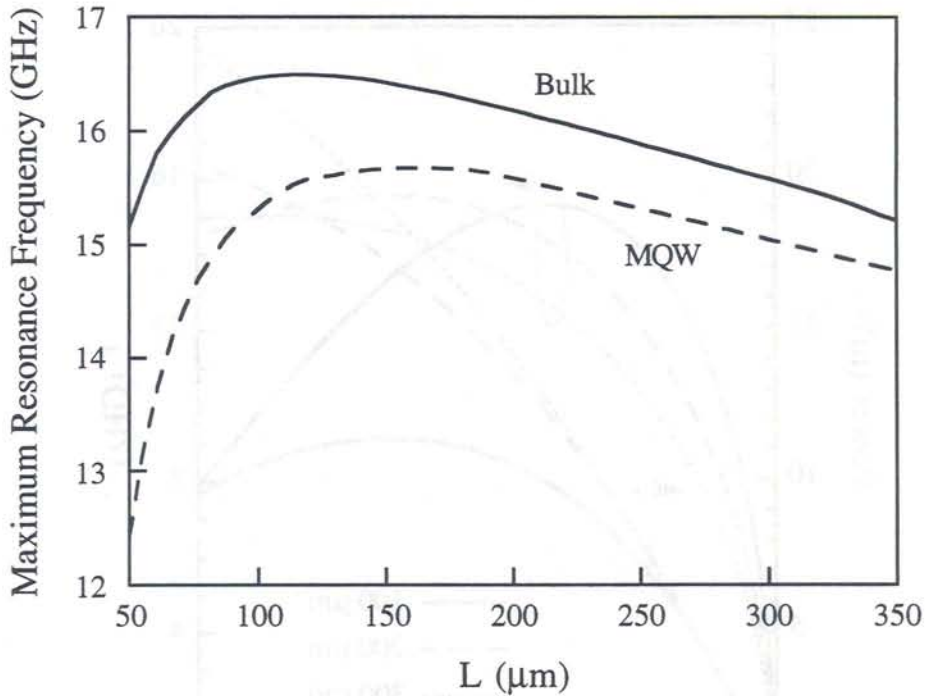
Figure 2.3   Calculated dependence of maximum resonance frequency on cavity length for typical bulk and MQW structures.

characteristics, the optimum cavity length for MQW lasers is slightly longer than that for bulk lasers.

2.4   Current Leakage

High output power is obtained by increasing the injected current, I, and reducing the threshold current, I_{th}. The maximum modulation bandwidths are experimentally observed near the maximum output power, $P_{0\,max}$. However, $P_{0\,max}$ may be indirectly limited by current leakage, and therefore requires a structure with good current confinement. One of the most common methods of current confinement in the InP system is the use of regrown, reverse-biased p-n junctions. p-n junctions provide excellent current blocking for a large range of operating voltages and

temperatures. However, p-n junctions also have an inherently high diffusion capacitance. This diffusion capacitance can be as high as several tens of pF, depending on the size and structure of the laser. This limits their usefulness in high speed laser structures. Special processing techniques, such as a mesa isolation [11] or an air bridge structure [12], may be used to reduce the diffusion capacitance to acceptable levels. However, these techniques tend to reduce the planarity and possibly the thermal conductivity of these devices.

To avoid these problems the use of regrown semi-insulating (SI) InP layers has been investigated extensively. Thick SI layers provide adequate current blocking characteristics and a much smaller parasitic capacitance than p-n junctions. Due to the nature of carrier injection in insulators and the phenomenon of double carrier injection, however, the current blocking capability of SI InP material is more sensitive to operating voltage and temperature than that of p-n junctions. In addition, there is the problem of enhanced dopant diffusion between Zn and Fe doped layers. Both of these problems require careful laser design in order to minimize their effects. The theoretical and practical approaches to employing semi-insulating material in semiconductor lasers will be discussed in Chapter 3.

The first four sections of this chapter have outlined the extrinsic limits to high speed operation. In the remainder of this chapter we turn to the intrinsic limits. We begin with some background, and follow with a discussion of transport and doping issues.

2.5   Theory of High Speed Modulation

Prior to the evolution of materials growth techniques that allowed for the fabrication of high quality quantum well (QW) structures, came the recognition that

25

such QW structures had potential advantages for high-speed semiconductor lasers. It was predicted that the increased differential gain of single and multiple quantum well structures would lead to enhancements of the slope of the resonance frequency versus the square root of the output power relative to bulk lasers [13, 14]. The addition of strain was predicted to further increase the resonance frequency due to an additional increase in differential gain [15]. Assuming an arbitrary maximum output power, Suemune et al. [15] predicted that modulation bandwidths up to 90 GHz might be possible. However, until recently, the many attempts to fabricate high-speed lasers with MQW active areas in both the GaAs and InP systems have fallen short of even the more modest predictions.

For some time it has been generally accepted that the primary intrinsic limitation to modulation bandwidth in QW lasers is the enhancement of gain compression relative to bulk lasers. Among the theories proposed to explain non-linear gain are spectral hole burning [16, 17, 18], a carrier density grating within the laser's cavity [19, 20], carrier heating [21, 22], quantum confinement [23], and strain [24]. Much controversy has ensued over the experimental verification of these theories. The pump/probe measurements of Kesler and Ippen [25], for example, support carrier heating, while some four-wave mixing measurements support the spectral hole burning model [26]. These and other methods have been used to determine the value of ε. Reported values of ε for 1.3 μm lasers have fallen in the range of 0.3×10^{-17} cm^{-3} to 4.5×10^{-17} cm^{-3}. For 1.55 μm lasers the reported range is 1.3×10^{-17} cm^{-3} to 6.7×10^{-17} cm^{-3}. The ratio $\varepsilon_{QW} / \varepsilon_{bulk}$ for reported [27] values of ε_{bulk} (1.5×10^{-17} cm^{-3}) is around 3 or 4. However, there is experimental evidence that ε is independent of the laser structure, and is even unaffected by the inclusion of strain,

26

compressive or tensile, in the quantum wells [28, 29, 30, 31]. Whatever the case, the relative enhancement of ε for quantum well lasers cannot not completely explain the observed modulation bandwidths achieved in quantum well lasers to date. Because of this, two models based on the transport and distribution of charge carriers have been proposed, the well-barrier hole burning model [32, 33], and the carrier transport model [34]. The latter has been shown to explain bandwidth limitations in GaAs/AlGaAs [35] lasers as well as InGaAsP/InP QW lasers [36]. Part of the purpose of this work is to demonstrate the usefulness of the transport model in the design of long-wavelength, MQW lasers for high speed applications. We begin by deriving an expression for carrier transport across a multilayer undoped region, such as those found on the p-side of many long-wavelength MQW lasers. The following review of transport theory is intended to emphasize the physics of carrier transport and outline the fundamental design parameters which must be optimized in order to achieve large modulation bandwidth.

2.6 Transport Across A Multilayer Undoped Region

Figure 2.4 shows the active area structure and doping of a typical MQW separate confinement heterostructure (SCH) laser. The active area consists of one or more quantum wells surrounded by an intermediate bandgap (SCH) region. The SCH region, in turn is surrounded by cladding regions of InP. The cladding regions are typically doped, whereas the SCH and quantum wells are not. In addition, there may be an undoped or "doping setback" layer in the p-type cladding adjacent to the active layer. This is true of all of the structures fabricated in this study, and the reasons for this are discussed in Chapter 5.

27
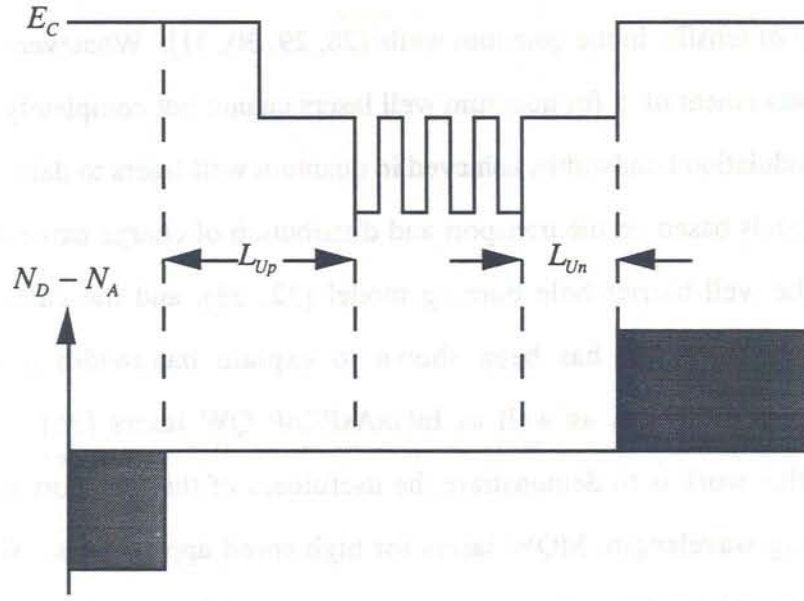
Figure 2.4   Band structure and doping levels of a typical undoped MQW active area. L_{Up} and L_{Un} are the p-side and n-side doping setback layers, respectively.

The dynamic distribution of carriers throughout the active area consists of two parts. First, carriers are transported from the highly doped cladding layers to the quantum well and are then captured by the well. Second, in MQW systems, carriers are transported from well to well via a combination of thermionic emission and tunneling. The transport time of holes and electrons across an undoped SCH were first derived by Nagarajan et al. [35] under the assumptions of ambipolar injection. In this section we will extend this formalism to include two layers of different composition, mobility and diffusion coefficient.

We begin with the current density equations for electrons and holes containing the contributions due to drift and diffusion,

$$J_n = q\mu_n nE + qD_n \frac{\partial n}{\partial x}$$

$$J_p = q\mu_p pE - qD_p \frac{\partial p}{\partial x}.$$

28

Using the Einstein relation $D/\mu = kT/q$ these become,

$$J_n = qD_n\left(\frac{qnE}{kT} + \frac{\partial n}{\partial t}\right)$$

$$J_p = qD_p\left(\frac{qpE}{kT} - \frac{\partial p}{\partial t}\right).$$

Taking the derivative with respect to x gives

$$\frac{\partial J_n}{\partial x} = qD_n\left(\frac{qn}{kT}\frac{\partial E}{\partial x} + \frac{qE}{kT}\frac{\partial n}{\partial x} + \frac{\partial^2 n}{\partial x^2}\right)$$

$$\frac{\partial J_p}{\partial x} = qD_p\left(\frac{qp}{kT}\frac{\partial E}{\partial x} + \frac{qE}{kT}\frac{\partial p}{\partial x} - \frac{\partial^2 p}{\partial x^2}\right).$$

Taking the current continuity equations we have

$$\frac{\partial n}{\partial t} = \frac{1}{q}\frac{\partial J_n}{\partial x} - U_{n,p}$$

$$\frac{\partial p}{\partial t} = -\frac{1}{q}\frac{\partial J_p}{\partial x} - U_{n,p}.$$

Substituting from above gives

$$\frac{\partial n}{\partial t} = D_p\left(\frac{qn}{kT}\frac{\partial E}{\partial x} + \frac{qE}{kT}\frac{\partial n}{\partial x} - \frac{\partial^2 n}{\partial x^2}\right) - U_{n,p}$$

$$\frac{\partial p}{\partial t} = -D_p\left(\frac{qp}{kT}\frac{\partial E}{\partial x} + \frac{qE}{kT}\frac{\partial p}{\partial x} - \frac{\partial^2 p}{\partial x^2}\right) - U_{n,p}.$$

Assuming high injection conditions, $n \approx p$, and charge neutrality, $\partial E/\partial x = 0$, the above equations can be combined. The electric field term, E, can be eliminated to give the following equation under steady state conditions, i.e. $\partial n/\partial t = \partial p/\partial t = 0$,

$$\frac{\partial^2 p}{\partial x^2} - \frac{D_n + D_p}{2D_n D_p}U_{n,p} = 0.$$

Assuming that the recombination rate is determined by an ambipolar lifetime, $U_{n,p} = p/\tau_a$, we have

$$\frac{\partial^2 p}{\partial x^2} - \frac{p}{D_a \tau_a} = 0,$$

where $D_a = 2D_n D_p/(D_n + D_p)$ is the ambipolar diffusion coefficient. Setting $L_p = \sqrt{D_p \tau_p}$, then

$$\frac{\partial^2 p}{\partial x^2} - \frac{p}{L_p^2} = 0.$$

The general solution is

$$p(x) = A e^{x/L_p} + B e^{-x/L_p}.$$

Now suppose we have a two layer system, each layer having a different length and hole mobility as illustrated in Figure 2.5. We inject holes from the left and place a quantum well on the right.
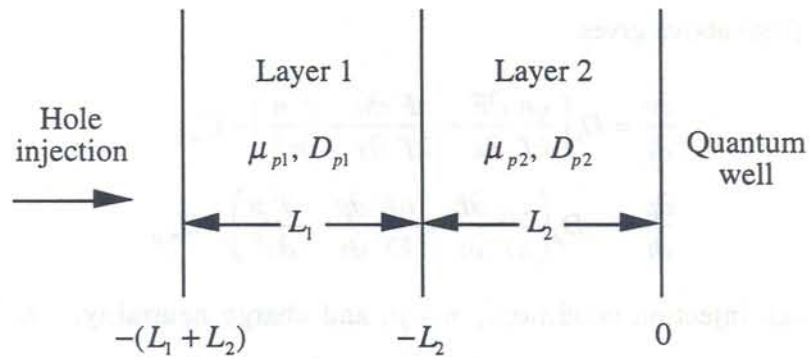
Figure 2.5   Schematic of undoped, two layer system for carrier transit time model.

The general solution in each layer may be written

$$p_1(x) = A e^{x/L_{p1}} + B e^{-x/L_{p1}}$$
$$p_2(x) = C e^{x/L_{p2}} + D e^{-x/L_{p2}}.$$

30

There are four boundary conditions: (i) at the left interface, where $E = 0$, the current density is equal to the diffusion of carriers away from the interface, (ii) at the center interface the carrier density must be continuous and, since there are no sources or sinks of carriers, (iii) the current densities must be equal. Finally, (iv) at the right interface, the carrier density is equal to the carrier density in the quantum well, p_w. In mathematical terms, these conditions are written

$$\text{(i)} \quad x = -(L_1 + L_2) \qquad\qquad J_0 = -qD_{p1}\frac{dp_1}{dx}\bigg|_{-(L_1+L_2)}$$

$$\text{(ii)} \quad x = -L_2 \qquad\qquad p_1 = p_2$$

$$\text{(iii)} \quad x = -L_2 \qquad\qquad J_1 = J_2$$

$$-qD_{p1}\frac{dp_1}{dx}\bigg|_{-L_2} = -qD_{p2}\frac{dp_2}{dx}\bigg|_{-L_2}$$

$$\text{(iv)} \quad x = 0 \qquad\qquad p_2 = p_w.$$

Substituting the general solutions in these expressions yields the following four equations for the coefficients A, B, C and D.

$$\text{(i)} \qquad\qquad -Ae^{-L_T/L_{p1}} + Be^{L_T/L_{p1}} = \frac{J_0 L_{p1}}{qD_{p1}}$$

$$\text{(ii)} \qquad Ae^{-L_2/L_{p1}} + Be^{L_2/L_{p1}} = Ce^{-L_2/L_{p2}} + De^{L_2/L_{p2}}$$

$$\text{(iii)} \quad Ae^{-L_2/L_{p1}} - Be^{L_2/L_{p1}} = \frac{D_{p2}L_{p1}}{D_{p1}L_{p2}}\left[Ce^{-L_2/L_{p2}} - De^{L_2/L_{p2}}\right]$$

$$\text{(iv)} \qquad\qquad C + D = p_w$$

where $L_T = L_1 + L_2$ and J_0 is the injected current density at $x = -L_T$. We can write this in matrix form as follows,

$$
\begin{pmatrix}
-e^{-L_T/L_{p1}} & e^{L_T/L_{p1}} & 0 & 0 \\
e^{-L_2/L_{p1}} & e^{L_2/L_{p1}} & -e^{-L_2/L_{p2}} & -e^{L_2/L_{p2}} \\
e^{-L_2/L_{p1}} & -e^{L_2/L_{p1}} & -\alpha e^{-L_2/L_{p2}} & \alpha e^{L_2/L_{p2}} \\
0 & 0 & 1 & 1
\end{pmatrix}
\begin{pmatrix} A \\ B \\ C \\ D \end{pmatrix}
=
\begin{pmatrix} \dfrac{J_0 L_{p1}}{qD_{p1}} \\ 0 \\ 0 \\ P_w \end{pmatrix},
$$

where $\alpha = D_{p2}L_{p1}/D_{p1}L_{p2}$. We are only interested in $p_2(x)$ so we need only solve for C and D. The solutions are $C = \det_3(M)/\det(M)$ and $D = \det_4(M)/\det(M)$, where $\det(M)$ is the determinant of the coefficient matrix above and $\det_i(M) = \det(M)$ with the vector on the right hand side substituted for the i-th column of M. Now

$$
\det(M) = -\alpha \exp\left(\frac{L_1}{L_{p1}} + \frac{L_2}{L_{p2}}\right) - \alpha \exp-\left(\frac{L_1}{L_{p1}} + \frac{L_2}{L_{p2}}\right)
$$

$$
= -\alpha(e^{\beta} + e^{-\beta}) = -2\alpha \cosh\beta,
$$

where $\beta = (L_1/L_{p1} + L_2/L_{p2})$ and

$$
\det_3(M) = \alpha p_w e^{\beta} + \frac{J_0 L_{p1}}{qD_{p1}}
$$

$$
\det_4(M) = \alpha p_w e^{-\beta} - \frac{J_0 L_{p1}}{qD_{p1}}.
$$

Thus C and D become

$$
C = \frac{-\alpha p_w e^{\beta} + \dfrac{J_0 L_{p1}}{qD_{p1}}}{-2\alpha \cosh\beta} = \frac{p_w e^{\beta} - \dfrac{J_0 L_{p2}}{qD_{p2}}}{2\cosh\beta}
$$

$$
D = \frac{\alpha p_w e^{-\beta} - \dfrac{J_0 L_{p1}}{qD_{p1}}}{-2\alpha \cosh\beta} = \frac{-p_w e^{-\beta} + \dfrac{J_0 L_{p2}}{qD_{p2}}}{2\cosh\beta}.
$$

The current flowing into the quantum well under steady state conditions is

$$
I_w = -qD_{p2}A\frac{dp_2}{dx}\bigg|_0 = -\frac{qD_{p2}A}{L_{p2}}(C - D)
$$

$$= I_0 \operatorname{sech}\beta - \frac{qD_{p2}Ap_w}{L_{p2}}\tanh\beta,$$

where w is the width of the active area, L is the cavity length and $A = Lw$. The differential transport factor, α_{tr}, can be defined as

$$\alpha_{tr} = \frac{\partial I_w}{\partial I_0} = \operatorname{sech}\beta.$$

The quantity of interest is the small-signal value of α_{tr}. The expression for this can be derived by letting

$$L_{p1} \to \sqrt{\frac{L_{p1}^2}{1 + j\omega\tau_{p1}}} \text{ and } L_{p2} \to \sqrt{\frac{L_{p2}^2}{1 + j\omega\tau_{p2}}}.$$

The small signal expression then becomes

$$\alpha_{tr,\,\text{small signal}} = \operatorname{sech}\left(\frac{L_1}{L_{p1}}\sqrt{1 + j\omega\tau_{p1}} + \frac{L_2}{L_{p2}}\sqrt{1 + j\omega\tau_{p2}} \right)$$

$$= \operatorname{sech}\left[\left(\frac{L_1^2}{L_{p1}^2} + j\omega\frac{L_1^2}{D_{p1}} \right)^{1/2} + \left(\frac{L_2^2}{L_{p2}^2} + j\omega\frac{L_2^2}{D_{p2}} \right)^{1/2} \right]$$

$$= \operatorname{sech}\left[\left(j\omega\frac{L_1^2}{D_{p1}} \right)^{1/2} + \left(j\omega\frac{L_2^2}{D_{p2}} \right)^{1/2} \right],$$

where we have assumed $L_1^2 \ll L_{p1}^2$ and $L_2^2 \ll L_{p2}^2$. Using the Taylor expansion for sech this further simplifies to

$$\alpha_{tr,\,\text{small signal}} = \frac{1}{1 + \frac{1}{2}\left[\left(j\omega\frac{L_1^2}{D_{p1}} \right)^{1/2} + \left(j\omega\frac{L_2^2}{D_{p2}} \right)^{1/2} \right]^2}$$

$$= \frac{1}{1 + j\omega\left(\frac{L_1^2}{2D_{p1}} + \frac{L_2^2}{2D_{p2}} + \frac{L_1 L_2}{\sqrt{D_{p1}D_{p2}}} \right)},$$

33

Assuming a small signal solution of the form $\alpha_{tr,\,small\,signal} = \left(1 + j\omega\tau_{tr}\right)^{-1}$, the transport time may be written as

$$\tau_{tr} = (\tau_{p1}^{1/2} + \tau_{p2}^{1/2})^2,$$

where

$$\tau_{p1} = \frac{L_1^2}{2D_{p1}} \text{ and } \tau_{p2} = \frac{L_2^2}{2D_{p2}}.$$

Let's examine the solution for a special case. Let us assume that $D_{p1} = D_{p2} = D_p$. Then

$$\tau_{tr} = \frac{(L_1 + L_2)^2}{2D_p} = \frac{L_T^2}{2D_p}.$$

The transport through two layers of equal carrier mobility reduces to the case of transport through a single, uniform layer of thickness L_T. These results apply to all of the undoped lasers fabricated in this study, in which the undoped setback layer spans two different material compositions.

2.7 Transport Theory

The theory of transport effects in semiconductor lasers began with the discovery of the structure dependence of gain recovery dynamics in MQW optical amplifiers by Eisenstein *et al.* [37]. Based on these studies Nagarajan [38] and Sharfin *et al.* [39] first introduced the concept of carrier transport into the rate equations. The small signal solution to the modified rate equations was first derived by Nagarajan *et al.* [35]. We will adopt the formalism of Reference [35] with one exception: here, the SCH region influences only the optical confinement factor, whereas carrier transport depends only on the thickness and composition of the doping setback layer(s). We begin with the rate equations for a single quantum well

34

laser structure with a doping setback layer and separate confinement layer. The rate equations for the carrier number in the undoped region, U, and the active region, N, and the photon number in the active region, S, are written as [35]

$$\frac{dU}{dt} = \frac{I}{q} - \frac{U}{\tau_{rU}} - \frac{U}{\tau_{tr}} + \frac{N}{\tau_{te}}$$

$$\frac{dN}{dt} = \frac{U}{\tau_{tr}} - \frac{N}{\tau_{rN}} - \frac{N}{\tau_{te}} - \frac{G(N)S}{1+\varepsilon S}$$

$$\frac{dS}{dt} = \frac{G(N)S}{1+\varepsilon S} - \frac{S}{\tau_p} + \frac{\beta N}{\tau_{rN}} + S_n,$$

where I is the injection current, q is the electron charge, τ_{rU} and τ_{rN} are the carrier recombination lifetimes in the undoped layer and active area, $G(N)$ is the carrier number dependent gain function, ε is the gain compression factor, τ_p is the photon lifetime, β is the spontaneous emission factor and S_n is a white noise source. We have used the carrier and photon numbers for simplicity.

To obtain the small signal solution we assume a sinusoidal variation of the injection current, carrier and photon numbers and gain. Mathematically this is done by making the following substitutions: $I = I_0 + ie^{j\omega t}$, $U = U_0 + ue^{j\omega t}$, $N = N_0 + ne^{j\omega t}$, $S = S_0 + se^{j\omega t}$, $S_n = s_n e^{j\omega t}$, and $G = G_0 + g_0 ne^{j\omega t}$. s_n is a frequency independent constant related to the Schawlow-Townes linewidth [40]. Here we assume that when the small-signal carrier number amplitude, n, is small enough $G(N)$ may be considered linear about the steady state operating point N_0. g_0 is defined as the slope of $G(N)$ at the operating point. It must be noted that g_0 is also a function of the operating point, and varies inversely with N_0, thus accounting for gain saturation at higher carrier numbers. The results of substitution may be put into matrix form as follows [36]:

35

$$A(\omega) \begin{pmatrix} u \\ n \\ s \end{pmatrix} = \begin{pmatrix} a_{11} - j\omega & a_{12} & 0 \\ a_{21} & a_{22} - j\omega & a_{23} \\ 0 & a_{32} & a_{33} - j\omega \end{pmatrix} \begin{pmatrix} u \\ n \\ s \end{pmatrix} = - \begin{pmatrix} I/q \\ 0 \\ S_n \end{pmatrix},$$

where

$$a_{11} = -\frac{1}{\tau_{rN}} - \frac{1}{\tau_{dc}}, \; a_{12} = \frac{1}{\tau_{te}}, \; a_{21} = \frac{1}{\tau_{te}},$$

$$a_{22} = -\frac{1}{\tau_{rN}} - \frac{1}{\tau_{dc}} - \frac{g_0 S_0}{1 + \varepsilon S_0}, \; a_{23} = -\frac{G(N_0)}{(1 + \varepsilon S_0)^2},$$

$$a_{32} = \frac{g_0 S_0}{1 + \varepsilon S_0} + \frac{\beta}{\tau_{rN}}, \; a_{33} = \frac{G(N)}{(1 + \varepsilon S_0)^2} - \frac{1}{\tau_p},$$

and g_0 is the differential gain at the steady-state carrier number N_0.

The steady-state carrier quantities U_0, N_0, S_0, and I_0 can be calculated at a given output power, P_0, from the gain function $G(N)$, the steady-state solution of the photon density equation,

$$\frac{G(N)}{1 + \varepsilon S_0} = \frac{1}{\tau_p},$$

where we have ignored the Langevin noise and spontaneous emission terms, and the relation $S_0 = 2 P_0 \Gamma \tau_p (\alpha_m + \alpha_i)/(h\nu\alpha_m)$ Conversely, the output power and steady-state photon and carrier numbers may be calculated using the same three equations by first choosing a steady-state current injection level.

With a knowledge of the steady-state carrier and photon numbers the modulation response may be calculated. The modulation response normalized to the response at zero (dc) frequency, $M(\omega)$, is given by [36],

$$M(\omega) = \det A(0)/\det A(\omega)$$

$$= \frac{A_0}{(-j\omega)^3 + A_2(-j\omega)^2 + A_1(-j\omega) + A_0},$$

36

where $\det A(\omega)$ is the determinant of the matrix $A(\omega)$, and

$$A_0 = a_{11}a_{22}a_{33} - a_{11}a_{23}a_{32} - a_{12}a_{21}a_{33}$$
$$A_1 = a_{11}a_{22} + a_{22}a_{33} + a_{33}a_{11} - a_{12}a_{21} - a_{23}a_{32}$$
$$A_2 = a_{11} + a_{22} + a_{33}.$$

The denominator of $M(\omega)$ is a third order polynomial of $(-j\omega)$ and $M(\omega)$ can be fitted to an expression of the following form,

$$M(\omega) = \frac{\omega_{tr}}{\omega_{tr} + j\omega} \frac{\omega_0^2}{\omega_0^2 - \omega^2 + j\omega\gamma}.$$

This expression is the same as for the case of a bulk laser [41] with an additional term in front. This term represents a rolloff in the response due to carrier transport across the undoped setback region with characteristic rolloff frequency $\omega_{tr} = 1/\tau_{tr}$. It has the same form as the frequency response of parasitic elements and is therefore indistinguishable from the rolloff due to device parasitics.

In the case of a single quantum well case, various simplifying assumptions may be made which allow for an analytic solution to the modulation response. Assuming a negligible recombination rate in the undoped region, $U/\tau_{rU} \ll U/\tau_{tr}$, and $\omega\tau_{tr} \ll 1$, leads to [35]

$$\omega_{tr} = \frac{1}{\tau_{tr}}$$

$$\omega_0^2 = \frac{(g_0/\chi)S_0}{\tau_p(1+\varepsilon S_0)}\left(1+\frac{\varepsilon}{g_0\tau_n}\right)$$

$$\gamma = \frac{(g_0/\chi)S_0}{1+\varepsilon S_0} + \frac{\varepsilon S_0}{\tau_p(1+\varepsilon S_0)} + \frac{1}{\chi\tau_n},$$

where

$$\chi = 1 + \frac{\tau_{tr}}{\tau_{te}}.$$

37

The results of a rate equation analysis without transport can be recovered by setting $\chi = 1$. Conclusions we can draw from the above results are that (1) transport through the undoped layer can produce an additional, parasitic-like rolloff in the modulation response, (2) the effective differential gain can be reduced by, χ, an amount proportional to the ratio of the transport time to the thermionic emission time. Therefore it is important to minimize the transport through the undoped layer (by reducing its thickness, for example) and increase the thermionic emission time from the wells.

Figure 2.6 is an example of a calculated modulation response with and without carrier transport. A significant low frequency rolloff can be seen for the response curve with transport. The resonant peak shifts toward lower frequency and is damped by the transport effect. The 3 dB bandwidth is drastically reduced by the rolloff and damping due to carrier transport.

2.8 Relative Intensity Noise and K Factor

The relative amplitude noise (RIN) spectrum is derived by eliminating the pump term from the rate equations and looking at the frequency response due to the noise source alone. Thus, $N(\omega) = \det A_{33}(\omega)/\det A(\omega)$ where $\det A_{33}(\omega)$ is defined as the determinant of the matrix obtained by substituting the source vector into the third column of A. The result is [36]

$$N(\omega) = -s_n \frac{(-j\omega)^2 + B_1(-j\omega) + B_0}{(-j\omega)^3 + A_2(-j\omega)^2 + A_1(-j\omega) + A_0},$$

where

$$B_0 = a_{11}a_{22} - a_{12}a_{21}$$
$$B_1 = a_{11} + a_{22}.$$

38
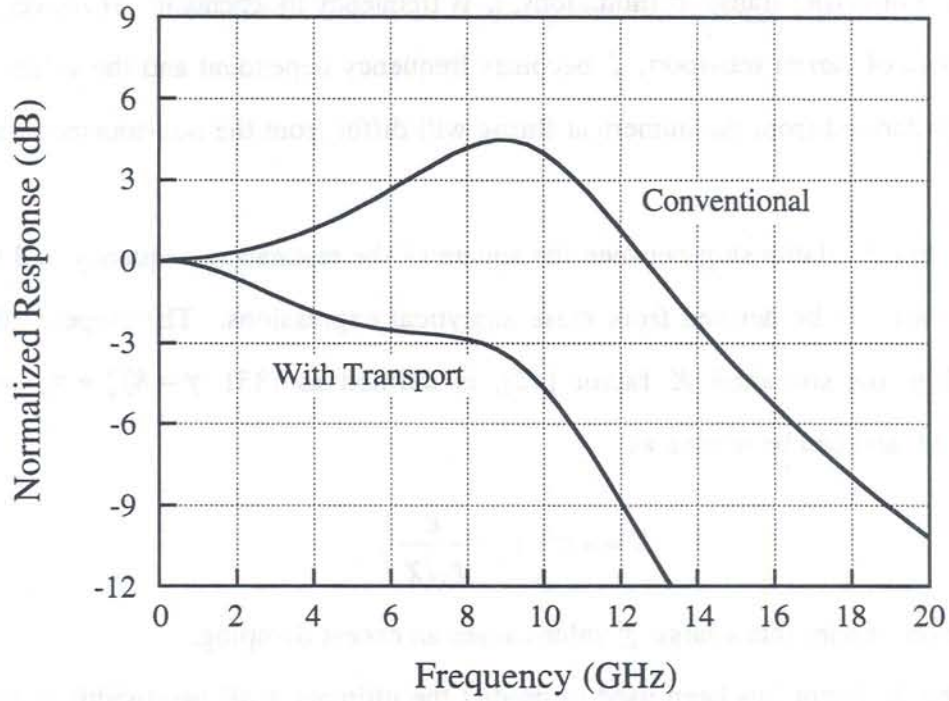
Figure 2.6   Calculated modulation response with and without carrier transport effects.

The relative intensity noise is then defined as the square of twice the small signal amplitude divided by the steady state photon density,

$$RIN(\omega) = \frac{4|N(\omega)|^2}{S_0^2}.$$

Since it is a dc measurement, the *RIN* spectrum has been used to determine the parasitic-free resonance frequency and damping coefficient [36, 37]. This is done by fitting the *RIN* spectrum to an equation of the form

$$RIN(\omega) = C\frac{\zeta + \omega^2}{(\omega_0^2 - \omega^2)^2 + (\omega\gamma)^2}.$$

where $\zeta = \gamma + a_{33}$ and C is a constant related to the Schawlow-Townes linewidth. Note that this expression contains no terms related to the transport frequency, ω_{tr}. In

39

the absence of carrier transport limitations, ζ is frequency independent. However, in the presence of carrier transport, ζ becomes frequency dependent and the values of ω_0 and γ derived from the numerical fitting will differ from the non-transport case [39].

A linear relationship between the square of the resonance frequency and the damping rate can be derived from these analytical expressions. The slope of this relationship, the so-called K factor [42], is defined as [35] $\gamma = K f_0^2 + \gamma_0$ with $f_0 = \omega_0 / 2\pi$ and can be written as

$$K = 4\pi^2 \left(\tau_p + \frac{\varepsilon}{g_0/\chi} \right).$$

This relation implies that a large χ value causes an excess damping.

The K factor has been used to predict the ultimate 3 dB bandwidth of bulk and MQW lasers [42, 43]. It is important to note, however, that in the presence of significant transport effects the K factor determined from noise measurements *cannot* predict the 3 dB bandwidth [44, 45]. It is for this reason that all of the 3 dB bandwidths in this work were determined from actual modulation response measurements. Furthermore, K factor measurements determined from *RIN* or frequency subtraction methods cannot distinguish between reduced differential gain due to either gain compression or carrier transport.

2.9 Adding Quantum Wells

One way to increase the differential gain of a quantum-well laser is to increase the number of quantum wells. To first order, the total gain and differential gain increase linearly with the number of quantum wells. However, transport effects tend to diminish the benefits of increasing the number of quantum wells in two ways: (1)

40

slow carrier transport between wells can cause a non-uniform carrier distribution among the wells, which can lead to gain saturation in some wells and insufficient pumping in others and (2) slow carrier transport between wells can lead to an additional low frequency rolloff similar to that of the undoped region adjacent to the active area.

To extend the transport model to include multiple quantum wells, the rate equations must be modified to account for the carriers in each well and each barrier [46]. Strictly speaking, carrier numbers in two and three dimensional states must be counted separately. Figure 2.7 shows the physical processes that must be accounted for. These include transport across the undoped and SCH regions, capture by the quantum well, thermionic emission from the well, well to barrier transport, barrier-to-well transport and well-to-well tunneling. Here we will present a simplified treatment in which carrier capture times and well-to-well diffusion times are small compared to thermionic emission times. Furthermore, we will assume that both the transport time from one well to the next and the spontaneous carrier lifetime are independent of the number of carriers in the well. Under these assumptions the coupled rate equations for a MQW laser are [46]

$$\frac{dU_1}{dt} = \frac{I}{q} - \frac{U_1}{\tau_{rU}} - \frac{U_1}{\tau_{tr}} + \frac{N_1}{\tau_{te}}$$

$$\frac{dN_i}{dt} = \frac{N_{i-1} - N_i}{\tau_T} - \frac{N_i - N_{i+1}}{\tau_T} - \frac{N_i}{\tau_{rN}} - \frac{G_i S_i}{1 + \varepsilon S_i}$$

$$\frac{dU_2}{dt} = -\frac{U_2}{\tau_{rU}} - \frac{U_2}{\tau_{tr}} + \frac{N_m}{\tau_{te}}$$

$$\frac{dS}{dt} = \sum_{i=1}^{m} \frac{\Gamma_i G_i}{1 + \varepsilon S_i} S - \frac{S}{\tau_p} + \beta \sum_{i=1}^{m} \frac{N_i}{\tau_{rN}}.$$

41
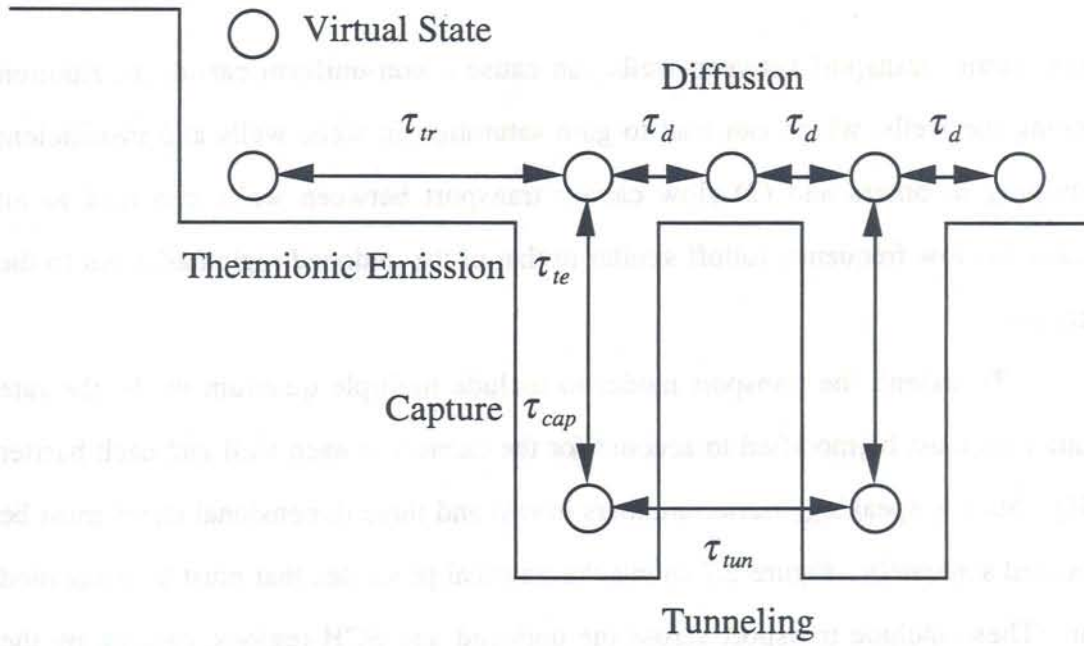
Figure 2.7   Carrier transport processes in a MQW laser. After Ishikawa *et al.* [46].

with $1 \le i \le m$, $N_0/\tau_T = U_1/\tau_{tr}$ and $N_{m+1}/\tau_T = U_2/\tau_{tr}$. I is the injection current, q the electron charge, and τ_T the interwell transport time. All other parameters are as defined previously. Note that N_i and S_i are the number of carriers and the number of photons *in the i-th well*, respectively, and $S = \sum S_i$ is the photon number in the active region consisting of m wells.

By making the small signal substitutions as in the single quantum well case, we arrive at the following equations for steady state operation,

$$\frac{U_{01}}{\tau_{rU}} + \frac{U_{01}}{\tau_{tr}} - \frac{N_{01}}{\tau_{te}} = \frac{I}{q}$$

$$-\frac{N_{0i-1} - N_{0i}}{\tau_T} + \frac{N_{0i} - N_{0i+1}}{\tau_T} + \frac{N_{0i}}{\tau_{rN}} + \frac{G_{0i}S_{0i}}{1 + \varepsilon S_{0i}} = 0$$

$$\frac{U_{02}}{\tau_{rU}} + \frac{U_{02}}{\tau_{tr}} - \frac{N_{0m}}{\tau_{te}} = 0$$

$$\sum_{i=1}^{m} \frac{\Gamma_i G_{0i}}{1 + \varepsilon S_{0i}} S_0 - \frac{S_0}{\tau_p} + \beta \sum_{i=1}^{m} \frac{N_{0i}}{\tau_{rN}} = 0,$$

42

and for the small signal terms,

$$j\omega u_1 = \frac{i}{q} - \frac{u_1}{\tau_{rU}} - \frac{u_1}{\tau_{tr}} + \frac{n_1}{\tau_{te}}$$

$$j\omega n_i = \frac{n_{i-1} - n_i}{\tau_T} - \frac{n_i - n_{i+1}}{\tau_T} - \frac{n_i}{\tau_{rN}} - \frac{S_{0i}g_i n_i}{1 + \varepsilon S_{0i}} - \frac{G_{0i}s_i}{(1 + \varepsilon S_{0i})^2}$$

$$j\omega u_2 = -\frac{u_2}{\tau_{rU}} - \frac{u_2}{\tau_{tr}} + \frac{n_m}{\tau_{te}}$$

$$j\omega s = \sum_{i=1}^{m} \left[\frac{\Gamma_i S_0 g_i}{1 + \varepsilon S_{0i}} n_i + \frac{\Gamma_i G_{0i}}{(1 + \varepsilon S_{0i})^2} s \right] - \frac{s}{\tau_p} + \beta \sum_{i=1}^{m} \frac{n_i}{\tau_{rN}}.$$

The steady-state equations can be solved self-consistently to obtain the dc operating point carrier and photon numbers. Once these quantities are known, the small signal solution may be calculated to find the modulation response. This is necessarily a purely numerical calculation. However, it is possible to understand the quantitative results with qualitative analysis.

Figure 2.8 shows an example of the steady state solution for the carrier distribution of a 10 quantum well laser for a bias current of 100 mA [46]. Near threshold the carrier number is fairly similar between wells. As the bias current is increased, however, the carrier distribution becomes increasingly non-uniform. This is because stimulated emission reduces the carrier lifetime to the order of the well-to-well transport time. The wells near the p side have the largest number of carriers. This non-uniform carrier distribution has several consequences for high speed operation of laser diodes. First and foremost, a non-uniform carrier distribution saturates the gain in some wells and can reduce the overall differential gain significantly. This implies that increasing the number of wells does not necessarily increase the differential gain. Also, the carrier distribution uniformity depends heavily on the structure of the quantum well. Therefore, the well width, barrier width,

43
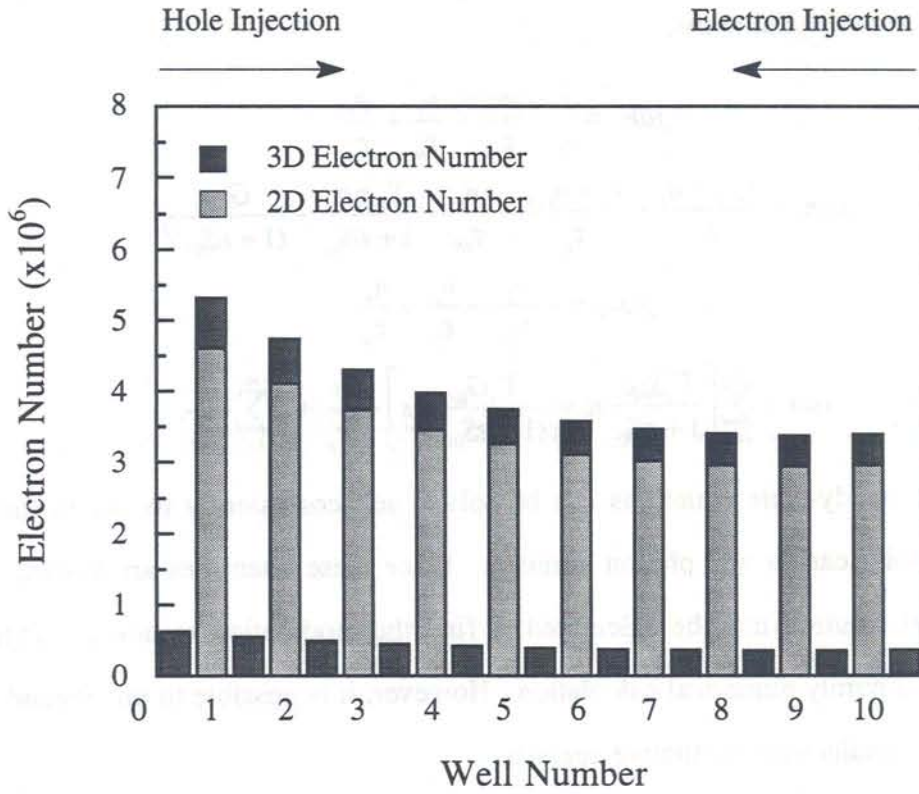
Figure 2.8   Calculated carrier distribution of electrons in a 10-QW laser at a bias current of 100 mA. The barrier material wavelength is 1.2 μm, the barrier width is 10 nm, and the output power is 29 mW per facet. The short bars between the wells indicate carrier numbers in the barrier and SCH regions. After Ishikawa *et al.* [46].

and barrier height are parameters that must be optimized in order to achieve high modulation bandwidth.

The parameter of greatest importance in determining the uniformity of carrier injection is the well-to-well transport time, τ_w. Figure 2.9 shows the variation of τ_w as a function of the wavelength of the barrier material for various barrier widths. A smaller transport time implies a more uniform carrier distribution. The variation of well width with barrier height for an emission wavelength of 1.55 μm is also shown. It is seen that the transport time for any given barrier height saturates at a barrier

44
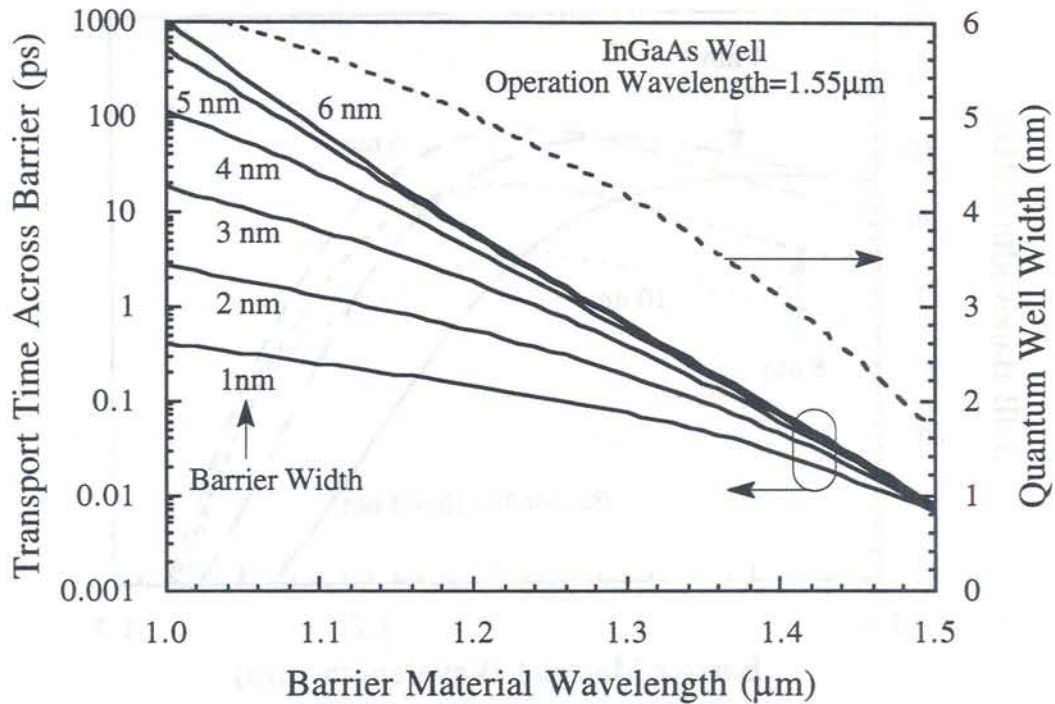
Figure 2.9   Well-to-well transport time as a function of barrier material wavelength for various
              barrier widths. The dashed line represents the well width necessary for a lasing
              wavelength of 1.55 μm. After Ishikawa *et al.* [46].

width of about 6 nm. Assuming the diffusion time across the barrier is small
compared to the tunneling and thermionic emission times, thicker barriers do not
increase τ_w.

The barrier height affects the well-to-well transport time through the
thermionic emission time. For an InGaAs well there is a one to one correspondence
between the well width and the barrier height for an emission wavelength of 1.55 μm
(dashed line of Figure 2.9). The well width increases with barrier height. Since the
thermionic emission time scales linearly with well width and exponentially with
barrier height, reducing the barrier height decreases the thermionic emission time

45
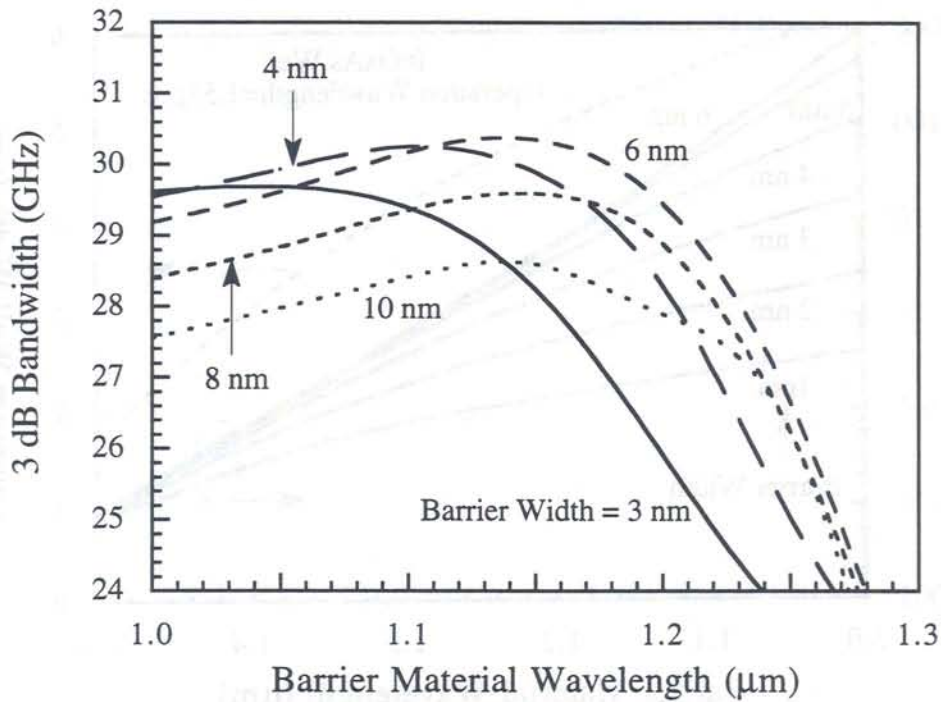
Figure 2.10   Maximum 3 dB bandwidth and optimum number of wells as a function of the barrier material wavelength. The kinks in the 3 dB bandwidth curves occur when the top of the miniband reaches the top of the well. After Ishikawa *et al.* [46].

dramatically. While this improves carrier uniformity, it has a detrimental effect on the effective differential gain through the χ factor derived previously. Thus there exists an optimum barrier height for maximum 3 dB bandwidth. Figure 2.10 shows the variation of maximum 3 dB bandwidth and optimum number of wells with the barrier material wavelength. For a barrier width of 10 nm the maximum bandwidth occurs at a barrier material wavelength of 1.24 - 1.26 μm. The optimum number of wells in this case is 13. The calculation is made for barrier widths of 5 and 15 nm as well.
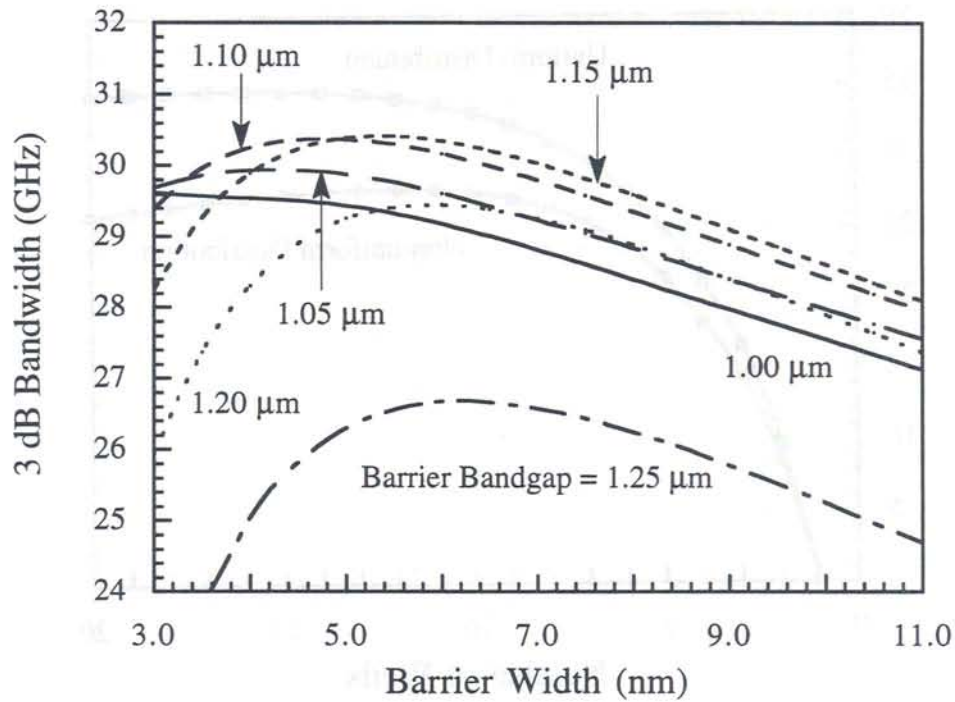
Figure 2.11   Maximum 3 dB bandwidth and optimum number of wells as a function of the barrier width. After Ishikawa *et al.* [46].

The barrier width also affects the well-to-well transport time through the tunneling time. In general, thinner barriers reduce the tunneling and overall transport times. However, as the barrier width is reduced the coupling between wells becomes stronger. Eventually band-splitting occurs which increases the threshold and, coupled with a large number of wells, changes the two-dimensional density of states to a three-dimensional-like density of states thus reducing the differential gain. There is therefore a lower limit to the barrier width for maximum bandwidth. Figure 2.11 shows the variation of maximum 3 dB bandwidth and optimum number of wells with the barrier width. The maximum bandwidths all occur at barrier widths of 10 nm or less.

47
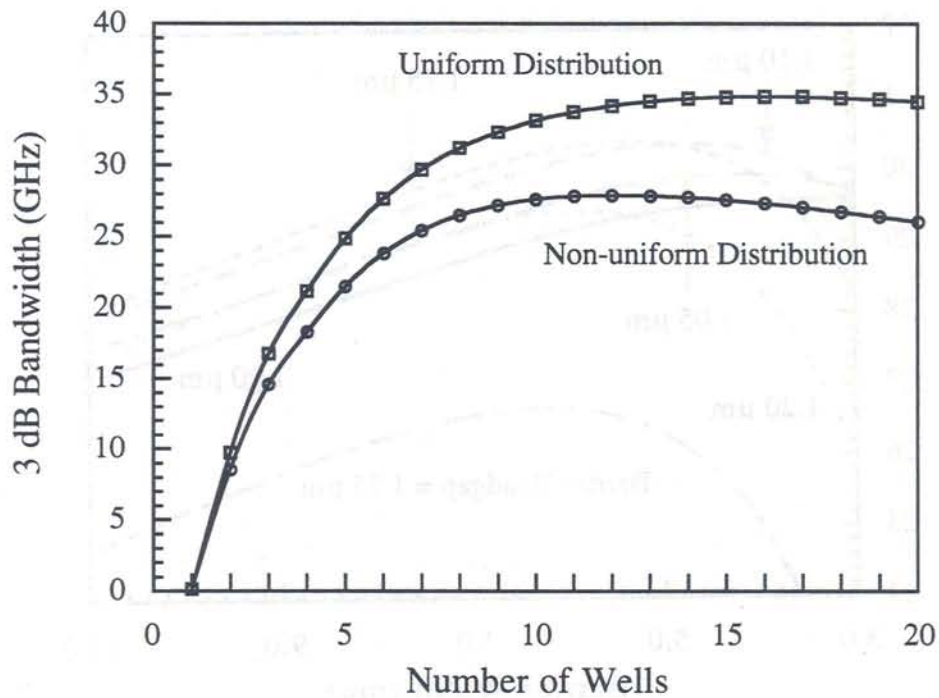
Figure 2.12   Optimized maximum modulation bandwidth as a function of the number of wells for
the case of uniform and non-uniform carrier distributions. After Ishikawa *et al.* [46].

Figure 2.12 shows the optimized maximum modulation bandwidth as a function of the number of wells for the case of uniform and non-uniform carrier distribution. Table 2.2 lists the typical parameters that were used in the calculation. The major results of including non-uniform carrier injection into the transport equations are (1) the differential gain and resonance frequency do not increase indefinitely with an increasing number of quantum wells, leading to an optimum number of wells for maximum bandwidth for any particular material system, and (2) the maximum obtainable bandwidth for optimized wells and number of wells is less than that predicted for the same structure assuming uniform carrier injection.

48

Parameter	Symbol	Value
Operation Wavelength	λ_0	1.55 μm
Active Region Width	w	1.0 μm
Cavity Length	L	300 μm
Mirror Reflectivity	R	0.35
Internal Loss	α_i	10 cm^{-1}
Gain Compression Factor	ε	1×10^{-17} cm^{-3}
Electron Capture Time	τ_{cap}^e	0.1 ps
Hole Capture Time	τ_{cap}^h	0.1 ps
Spontaneous Lifetime	τ_{sp}	1.0 ns
Spontaneous Emission Factor	β	1×10^{-4}
Bandgap Discontinuity Ratio of Conduction Band	δE_c	0.39
Optical Confinement Factor	Γ	structure dependent

Table 2.2   Typical values of the parameters used in the calculated modulation response.

2.10 Active Area Doping

The effects of active layer doping on the performance of InGaAsP/InP lasers have been investigated experimentally [47, 48, 49] and theoretically [50]. Using a threshold carrier density measurement technique, Su *et al.* [47] measured the differential gain, g_0, at lasing threshold. It was found that the differential gain is a strong function of the active layer doping. For a *p*-type doping level of 2.5×10^{18} cm^{-3} g_0 was found to increase by a factor of 4 to 5 over the undoped case. It was also found that the threshold carrier density, n_{th}, decreased slightly with the doping level

49

as predicted by Nelson *et al.* [51]. Despite this reduction in n_{th}, the threshold current density, J_{th}, was found to increase. J_{th} is given by the rate equation

$$\frac{J_{th}}{qd} = \frac{n_{th}}{\tau_n},$$

where d is the active layer thickness. The carrier lifetime, τ_n, is described by

$$1/\tau_n = a + bn + cn^2,$$

where a, b and c are the recombination coefficients relating to non-radiative, spontaneous and Auger recombination, respectively. The increase of J_{th} with p-doping has been attributed to a reduction in the carrier lifetime due to an increase in the non-radiative recombination rate. This has been confirmed experimentally [52, 53]. An increase in the modulation bandwidth of p-doped active area lasers has been observed in both bulk [47, 54, 55, 56] and MQW [57, 58] lasers, and has been attributed to the increased differential gain and reduced carrier lifetime.

The reduction of threshold carrier density can be understood by examining the expression for optical gain in a direct bandgap semiconductor. The material will become transparent when the separation of the quasi-Fermi levels, E_{fc} and E_{fv}, becomes equal to the photon energy, or

$$E_{fc} - E_{fv} = \hbar\omega.$$

This implies that there must be a simultaneous, non-equilibrium electron and hole density. In other words, the maximum slope of the quasi-Fermi function must be at or beyond the band edge in at least one band. The carrier density at which this occurs is known as the transparency carrier density, n_{tr}, and its magnitude is fundamentally related to the density of states, ρ_c and ρ_v of a given material. The band edge transparency condition for four different simplistic situations is shown in Figure 2.13.

50

(a)

(b)

(c)
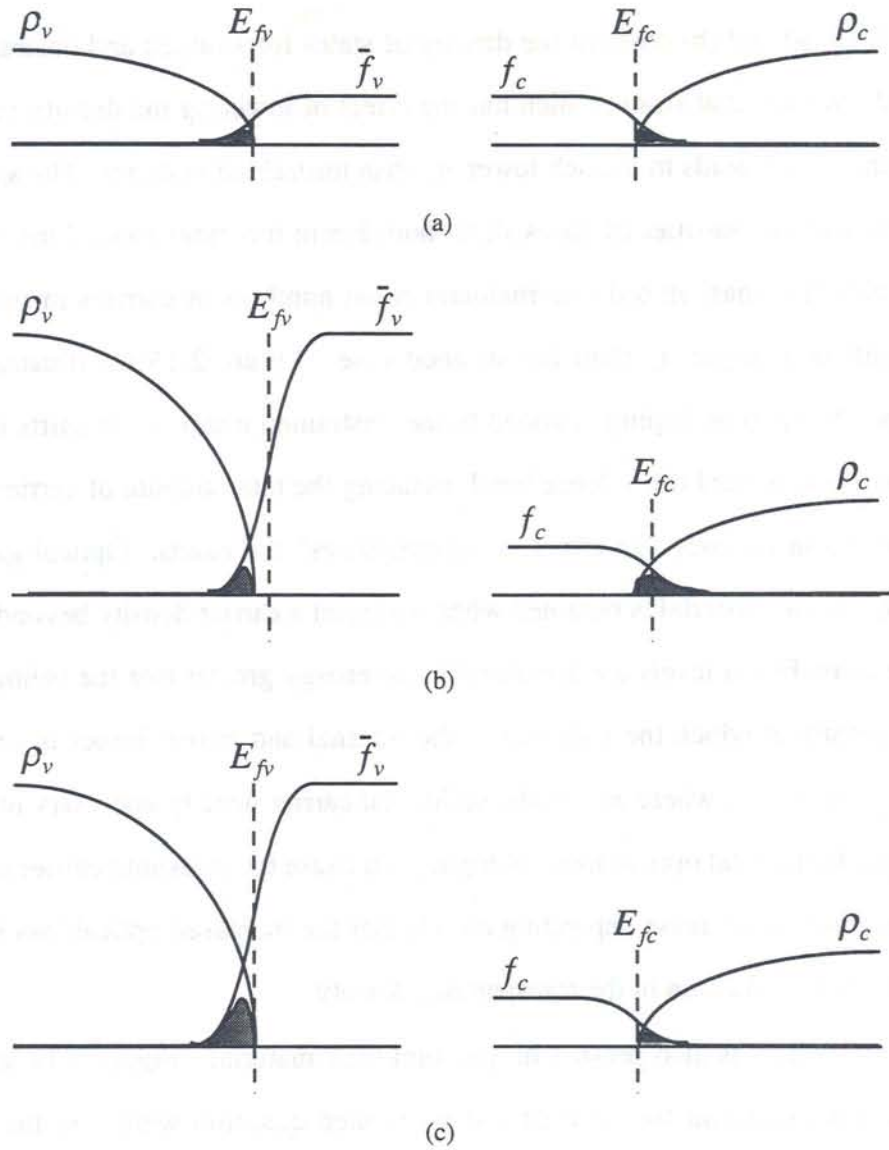
Figure 2.13 Band edge transparency condition $(E_{fc} - E_{fv} = E_g)$ illustrated for three different idealized cases of bulk material. (a) $m_v^* = m_c^*$, undoped. (b) $m_v^* = 3m_c^*$, undoped. (c) $m_v^* = 3m_c^*$, p-doped. The density of states, ρ_c and ρ_v for each case assume parabolic bands. The carrier filling of each band is illustrated by the shaded overlap region between the Fermi function and the density of states. The 'hole' Fermi function, $\bar{f}_v = 1 - f_v$, is used in the figure for clarity. After Corzine *et al.* [59].

Figure 2.13 (a) and (b) contrast the density of states for strained and unstrained bulk material. We see that strain, which has the effect of lowering the density of states in the valence band, leads to a much lower n_{tr} than unstrained material. The asymmetry of the unstrained densities of states shifts both Fermi functions toward the band with lighter effective mass in order to maintain equal numbers of carriers in both bands. The result is a larger n_{tr} than the strained case. Figure 2.13 (c) illustrates what happens when p-type doping is added to the unstrained material. It shifts the Fermi functions back toward the valence band, reducing the total amount of carriers needed to achieve transparency. In effect, it "symmetrizes" the bands. Optical gain at the band edge of the material is obtained when we inject a carrier density beyond n_{tr} such that the quasi-Fermi levels are separated by an energy greater that the bandgap. The carrier density at which the gain equals the internal and mirror losses is simply n_{th}. Thus $n_{th} = n_{tr} + n_{loss}$, where n_{loss} is the additional carrier density necessary to produce gain equal to the total optical loss. p-doping can cause the threshold carrier density to either increase or decrease depending on whether the increased optical loss is greater or less than the reduction in the transparency density.

This effect is also present in quantum well material. Figure 2.14 shows the transparency condition for strained and unstrained quantum wells. In the strained material the bands are similar. In addition, the density of states is reduced due to quantum confinement. Both of these effects contribute to the lowering of n_{tr}. In the case of unstrained quantum wells, ρ_c and ρ_v, while both reduced, are still unsymmetric. This may be compensated for by heavily doping the material p-type. In real, strained material with $\Delta a_0 / a_0$ on the order of 1% the bands are not completely symmetric. Thus, some level of doping is beneficial for reducing n_{tr}.

52
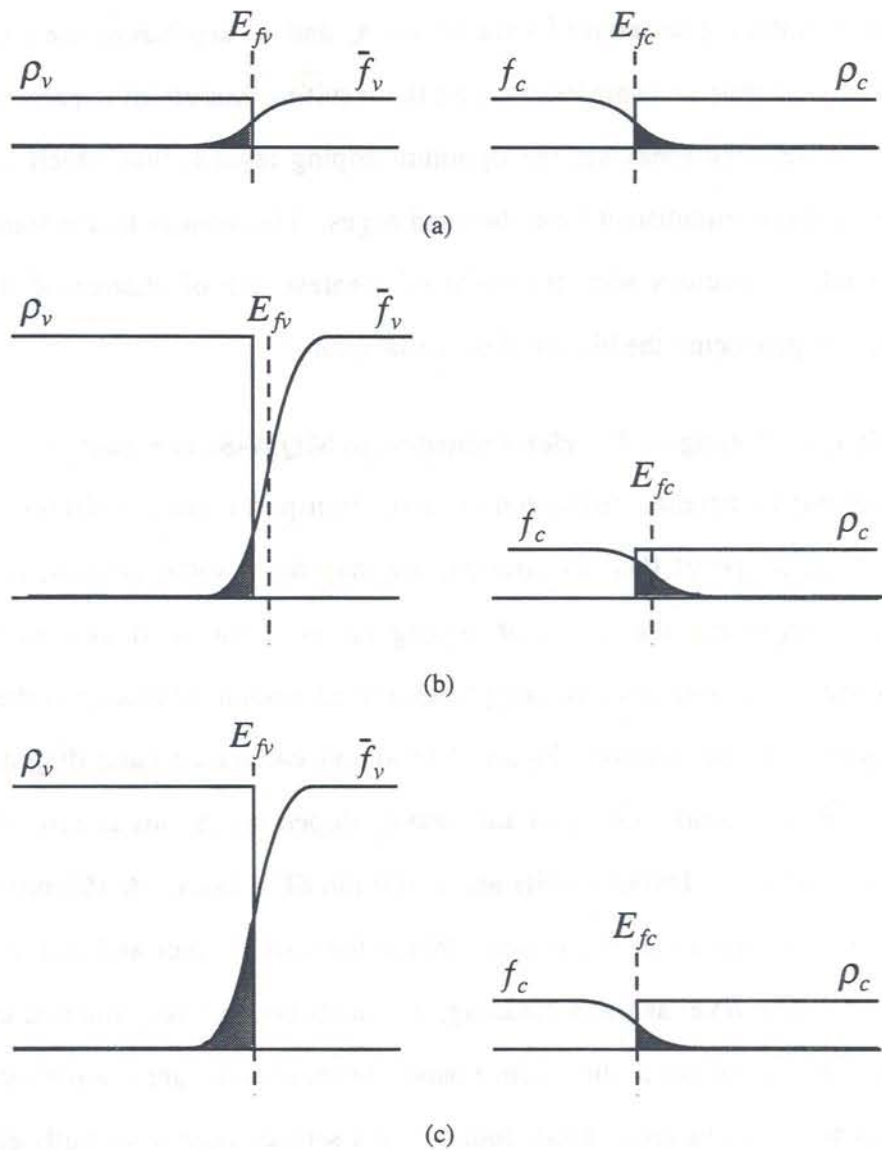
Figure 2.14 Band edge transparency condition $(E_{fc} - E_{fv} = E_g)$ illustrated for three different idealized cases of MQW material. (a) $m_v^* = m_c^*$, undoped. (b) $m_v^* = 3m_c^*$, undoped. (c) $m_v^* = 3m_c^*$, p-doped. The density of states, ρ_c and ρ_v, for each case assume parabolic bands. The carrier filling of each band is illustrated by the shaded overlap region between the Fermi function and the density of states. The 'hole' Fermi function, $\bar{f}_v = 1 - f_v$, is used in the figure for clarity. After Corzine *et al.* [59].

The amount of doping necessary for the lowest n_{tr} and n_{th} depends on the amount and type of strain, tensile or compressive, and the resulting amount of asymmetry in the bands. Qualitatively speaking, the optimum doping level is that which makes the quasi-Fermi levels equidistant from the band edges. This assures that at transparency the band edge coincides with the point of greatest rate of change of the Fermi function, thus producing the highest differential gain.

2.11 Effects of Doping on Carrier Transport in MQW-SCH Structures

Although a detailed discussion of carrier transport under conditions of doping is beyond the scope of this dissertation, we may draw some general, qualitative conclusions regarding the effect of doping on SCH transport and well-to-well transport times. In both cases doping places a fixed amount of charge in the SCH or MQW layers. As an example, Figure 2.15 shows calculated band diagrams for a typical MQW laser under undoped and heavily doped conditions at zero bias. The active area contains 7 InGaAs wells and a 100 nm SCH layer. A 100 nm undoped setback layer is located on the p side. When the spacer layer and active area are doped to the same level as the p-cladding, the bands become very flat and the Fermi level is pushed very close to the valence band. There is no longer a depletion layer in or adjacent to the active area. Thus, doping of the setback layer essentially eliminates the transport time associated with an undoped setback layer. While this may seem obvious to the device designer, it is another matter entirely to achieve this technologically without seriously degrading other aspects of the device performance. A possible solution to this problem is discussed in Chapter 5.

Assuming that the diffusion time across the barrier is negligible compared to the thermionic emission time out of the well, then the overall effect of doping on the
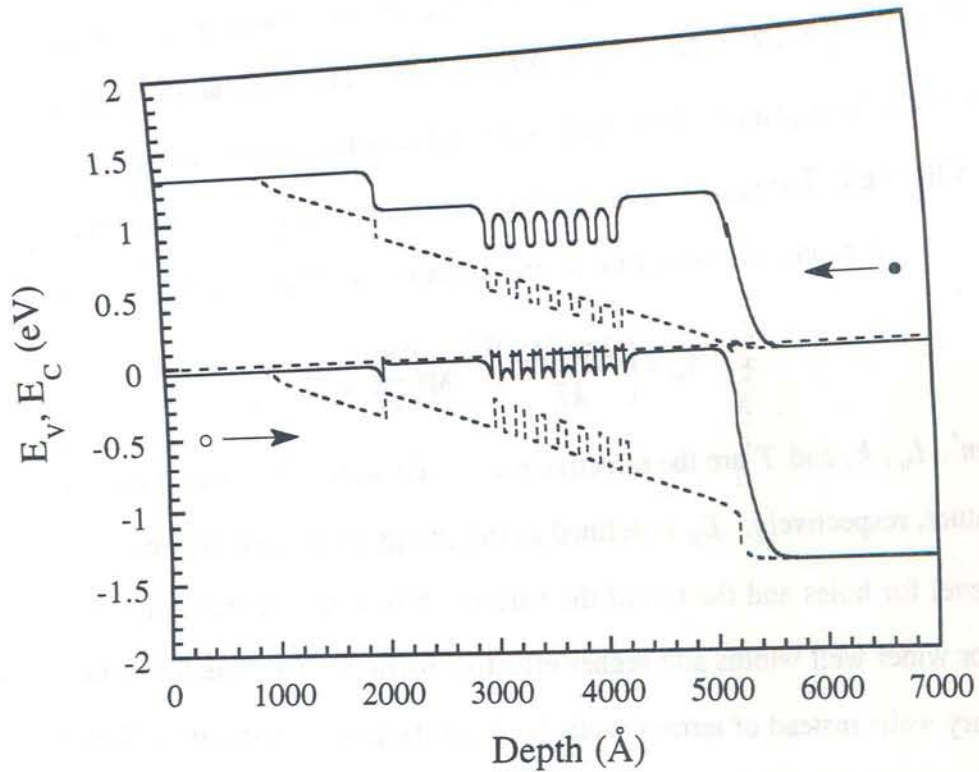
Figure 2.15   Calculated band diagrams for typical MQW laser at zero bias. The dotted lines
represent the undoped case and the solid lines the doped case. The Fermi level is
constant at zero energy throughout the device.

well-to-well transport time is much smaller than its effect on the SCH transport time.

The well-to-well transport time, τ_T consists of two parts: a tunneling time, τ_{tun}, and

a thermionic emission time, τ_{te}. The tunneling and thermionic emission processes

work in parallel. Thus, the total well-to-well transport time may be written as

$$\frac{1}{\tau_T} = \frac{1}{\tau_{tun}} + \frac{1}{\tau_{te}}.$$

The expression for tunneling time is given by

$$\tau_{tun} = \frac{h}{2}(E_{odd} - E_{even}),$$

55

where h is Plank's constant and E_{even} and E_{odd} are the lowest even and odd bound state energies of a two well system, respectively. The even and odd bound state energies depend only on the heterojunction band offsets, the effective masses and the width of the well. The tunneling time is therefore independent of doping level.

The thermionic emission time from a quantum well [60] τ_{te} is,

$$\tau_{te} = \left(\frac{2\pi m^* L_w^2}{kT} \right)^{1/2} \exp\left(\frac{E_B}{kT} \right),$$

where m^*, L_w, k, and T are the effective mass, well width, Boltzmann constant, and temperature, respectively. E_B is defined as the energy difference between the quasi-Fermi level for holes and the top of the barrier. It is seen that the emission time is larger for wider well widths and higher effective barriers. This has led to the use of quaternary wells instead of ternary wells [61] and the proposed use of InGaAlAs as a barrier material [57]. Under high injection conditions the quasi-Fermi level sits very near the first quantized level for holes and changes very little with applied bias. Thus, the barrier for thermionic emission, E_B, is fairly constant and independent of doping. We conclude that, under high injection conditions, both τ_{tun} and τ_{te} are independent of doping, which results in a doping-independent well-to-well transport time.

To summarize, the main effect of doping on carrier transport is to reduce the transport time from the point of carrier injection to the quantum well. The well-to-well transport time remains largely unaffected.

2.12 Overall Design Approach

We have described the fundamental extrinsic and intrinsic limits to high speed modulation of semiconductor lasers. Our approach will be to use both structural and material methods to reduce the electrical parasitics. We will minimize the parasitic

capacitance by using small bondpad areas on thick dielectric layers. In addition, we will employ semi-insulating current blocking layers instead of reverse-biased *p-n* junctions to reduce C_p. A discussion of semi-insulating layers and the results of current leakage measurements will be given in Chapter 3, leading to the conclusion that the CMBH family of structures is most appropriate for making high speed lasers. The laser fabrication process employing thick dielectric layers is described in Chapter 3. For the parasitic resistance we will employ wide *p*-contacts and advanced metallization schemes to reduce its contribution to the total series resistance. We will also demonstrate how the effect of the specific interface resistance can be reduced by employing high doping and graded bandgap layers. The results of the metallization and heterointerface experiments will be described in Chapter 4.

We have discussed design methods for optimizing the resonance frequency for both extrinsic (outside the active area) and intrinsic (within the active area) parameters. For the extrinsic case, we have shown how the individual design parameters vary with waveguide dimensions and described the complex interaction between them. A figure of merit for designing the transverse and lateral dimensions of the waveguide was given. We have further demonstrated how cavity length and mirror reflectivity can be optimized for high-speed operation. For the intrinsic case we have discussed transport and other limits to high-speed modulation. From the theory we conclude that it is important to reduce the width of the undoped layer near the active area in order to avoid low-frequency rolloff effects. Furthermore, for MQW lasers it is important to simultaneously optimize the number and width of the wells and the height and width of the barriers. Finally, we have discussed the advantages and disadvantages of doping the active area, both on the material

57

parameters, such as the transparency carrier density and differential gain, and on structural limitations, such as carrier transport effects. In this way we have outlined an approach to reducing each extrinsic and intrinsic limitation, thereby maximizing the modulation bandwidth of these lasers.

58

References

1. R. S. Tucker, "High-Speed Modulation of Semiconductor Lasers," *J. Lightwave Tech.*, vol. LT-3, pp. 1180-1192, 1985.

2. K. Y. Lau and A. Yariv, "Ultra-High-Speed Semiconductor Lasers," *J. Quantum Electron.*, vol. 21, pp. 121-138, 1985.

3. U. Koren, B. I. Miller, Y. K. Su, T. L. Koch, and J. E. Bowers, "Low Internal loss Separate Confinement Heterostructure InGaAs/InGaAsP Quantum Well Laser," *Appl. Phys. Lett.*, vol. 51, pp. 1744-1746, 1987.

4. J. E. Bowers and D. P. Wilt, "Optimum Design of 1.55-μm Double Heterostructures and Ridge-Waveguide Lasers," *Optics Lett.*, vol. 9, pp. 330-332, 1984.

5. A. Mar, P. A. Morton, and J. E. Bowers, "Optimum Facet Reflectivity for High Speed Lasers," *Electron. Lett.*, vol. 26, pp. 1382-1384, 1990.

6. A. Mar, J. E. Bowers, R. T. Huang, D. Wolf, W. H. Cheng, C. L. Jiang, R. Agarwal, and D. Renner, "High-Speed, Low-Threshold InGaAsP Semi-Insulating Buried Crescent Lasers," *Indium Phosphide and Related Materials Conference*, Newport, R. I., 1992, paper THE3.

7. W. H. Cheng, A. Mar, J. E. Bowers, R. T. Huang, and C. B. Su, "High-Speed 1.3 μm InGaAsP Fabry-Perot Lasers for Digital and Analog Applications," *IEEE J. Quantum Electron.*, vol. 29, pp. 1660-1667, 1993.

8. E. Meland, R. Holmstrom, J. Schlafer, R. B. Lauer, W. Powazinik, "Extremely High Frequency (24 GHz) InGaAsP Diode Lasers with Excellent Modulation Efficiency," *Electron. Lett.*, vol. 26, pp. 1827-1829, 1990.

9. G. P. Agrawal and N. K. Dutta, Long-Wavelength Semiconductor Lasers, Van Nostrand Reinhold, 1986, pp. 70-94.

10. S. W. Corzine, R. H. Yan, and L. A. Coldren, "Theoretical Gain in Strained InGaAs/AlGaAs Quantum Wells Including Valence Band Mixing Effects," *Appl. Phys. Lett.*, vol. 57, pp. 2835-2837, 1990.

11. Y. Sakakibara, H. Higuchi, E. Oomura, Y. Nakajima, Y. Yamamoto, K. Goto, H. Namziaki, K. Ikeda, and W. Susaki, "High-Power 1.3 μm InGaAsP P-Substrate Buried Crescent Lasers," *J. Lightwave Technol.*, vol. LT-3, pp. 978-983, 1985.

12. T. R. Chen, P. C. Chen, C. Gee, and N. Barchaim, "A High-Speed InGaAsP/InP DFB Laser With An Air Bridge Contact Configuration," *IEEE Photon. Technol. Lett.*, vol. 5, pp. 1-3, 1993.

13. Y. Arakawa and A. Yariv, "Theory of Gain, Modulation Response, and Spectral Linewidth in Quantum Well Lasers," *IEEE J. Quantum Electron.*, vol. QE-21, pp. 1666-1674, 1985.

14. Y. Arakawa and A. Yariv, "Quantum Well Lasers - Gain, Spectra, Dynamics," *J. Quantum Electron.*, vol. 22, pp. 1887-1899, 1986.

15. I. Suemune, L. A. Coldren, M. Yamanishi, and Y. Kan, "Extremely Wide Modulation Bandwidth in a Low Threshold Current Strained Quantum Well Laser," *Appl. Phys. Lett.*, vol. 53, pp. 1378-1380, 1988.

16. G. P. Agrawal, "Effect of Nonlinear Gain on Single-Frequency Behaviour of Semiconductor Lasers," *Electron. Lett.*, vol. 22, pp. 696-670, 1986.

17. M. Asada and Y. Suematsu, "Density-Matrix Theory of Semiconductor Lasers with Relaxation Broadening Model - Gain and Gain Supression in Semiconductor Lasers," *IEEE J. Quantum Electron.*, vol. QE-21, pp. 434-442, 1985.

60

18. R. Olshansky, D. M. Fye, J. Manning, and C. B. Su, "Effect of Nonlinear Gain on the Bandwidth of Semiconductor Lasers," *Electron. Lett.,* vol. 21, pp. 496-497, 1985.

19. C. B. Su, "Dielectric Grating Induced by Cavity Standing Wave as a New Explanation of Origin of Nonlinear Gain in Semiconductor Lasers," *Electron. Lett.*, vol. 24, pp. 370-371, 1988.

20. C. B. Su, "Nonlinear Gain Caused by Cavity Standing Wave Dielectric Grating as an Explanation fo the Relationship Between Resonance Frequency and Damping Rate of Semiconductor Diode Lasers," *Appl. Phys. Lett.,* vol. 53, pp. 950-952, 1988.

21. M. P. Kesler and E. P. Ippen, "Subpicosecond Gain Dynamics in GaAlAs Laser Diodes," *Appl. Phys. Lett.*, vol. 51, pp. 1765-1767, 1987.

22. B. Gomatam and A. P. DeFonzo, "Theory of Hot Carrier Effects on Nonlinear Gain in GaAs-AlGaAs Lasers and Amplifiers," *J. Quantum Electron.*, vol. 26, pp. 1689-1704, 1990.

23. T. Takahashi and Y. Arakawa, "Nonlinear Gain Effects in Quantum Well, Quantum Well Wire, and Quantum Well Box Lasers," *J. Quantum Electron.*, vol. 27, pp. 1824-1829, 1991.

24. A. Ghiti and E. P. O'Reilly, "Nonlinear Gain Effects in Strained-Layer Lasers," *Electron. Lett.*, vol. 26, pp. 1978-1980, 1990.

25. M. P. Kesler and E. P. Ippen, "Subpicosecond Gain Dynamics in GaAlAs Laser Diodes," *Appl. Phys. Lett.*, vol. 51, pp. 1765, 1987.

26. J. Eom, C. B. Su, W. Rideout, R. B. Lauer, and J. S. LaCourse, "Determination of the Gain Nonlinearity Time Constant in 1.3 μm Semiconductor Lasers," *Appl. Phys. Lett.*, vol. 58, pp. 234-236, 1991.

27. L. D. Westbrook, N. C. Fletcher, D. M. Cooper, M. Stevenson, and P. C. Sprudens, "Intensity Noise in 1.5 μm GaInAs Quantum Well Buried Heterostructure Lasers," *Electron. Lett.*, vol. 25, pp. 1183-1184, 1989.

28. Y. Hirayama, M. Morinaga, N. Suzuki, and N. Nakamura, "Extremely Reduced Nonlinear K-Factor in High-Speed Strained Layer Multiquantum Well DFB Lasers," *Electron. Lett.*, vol. 27, pp. 875-876, 1991.

29. T. Fukushima, J. E. Bowers, R. A. Logan, T. Tanbun-Ek, and H. Temkin, "Effect of Strain on the Resonant Frequency and Damping Factor in InGaAs/InP Multiple Quantum Well Lasers," *Appl. Phys Lett.*, vol. 58, pp. 1244-1246, 1991.

30. R. Nagarajan, T. Fukushima, J. E. Bowers, R. S. Geels, and L. A. Coldren, "Single Quantum Well Strained InGaAs/GaAs Lasers with Large Modulation Bandwidth and Low Damping," *Electron. Lett.*, vol. 27, pp. 1058-1059, 1991.

31. J. Shimizu, H. Yamada, S. Murata, A. Tomita, M. Kitamura, and A. Suzuki, "Optical-Confinement-Factor Dependencies of the K Factor, Differential Gain, and Nonlinear Gain Coefficient for 1.55 μm InGaAs/InGaAsP MQW and Strained-MQW Lasers," *Photon. Tech. Lett.*, vol. 3, pp. 773-776, 1991.

32. W. F. Sharfin, J. Schlafer, W. Rideout, B. Elman, R. B. Lauer, J. LaCourse, and F. D. Crawford, "Anomalously High Damping in Strained InGaAs-GaAs Single Quantum Well Lasers," *Photon. Tech. Lett.*, vol. 3, pp. 193-195, 1991.

33. W. Rideout, W. F. Sharfin, E. S. Koteles, M. O. Vassell, and B. Elman, "Well-Barrier Hole Burning in Quantum Well Lasers," *Photon. Tech. Lett.*, vol. 3, pp. 784-786, 1991.

34. R. Nagarajan, T. Fukushima, S. W. Corzine, and J. E. Bowers, "Effects of Carrier Transport on High Speed Quantum Well Lasers," *Appl. Phys. Lett.*, vol. 59, pp. 1835-1837, 1991.

62

35.   R. Nagarajan, M. Ishikawa, T. Fukushima, R. S. Geels, and J. E. Bowers, "High Speed Quantum-Well Lasers and Carrier Transport Effects," *J. Quantum Electron.*, vol. 28, pp. 1990-2008, 1992.

36.   M. Ishikawa, R. Nagarajan, T. Fukushima, J. Wasserbauer, and J. E. Bowers, "Long Wavelength High Speed Semiconductor Lasers with Carrier Transport Effects," *J. Quantum Electron.*, vol. 28, pp. 2230-2241, 1992.

37.   G. Eisenstein, J. M. Wiesenfeld, M. Wegener, G. Sucha, D. S. Chemla, S. Weiss, G. Raybon, and U. Koren, "Ultrafast Gain Dynamics in 1.5 μm Multiple Quantum Well Optical Amplifiers," *Appl. Phys. Lett.*, vol. 58, pp. 158-160, 1991.

38.   R. Nagarajan, T. Fukushima, S. W. Corzine, and J. E. Bowers, "Effects of Carrier Transport on High-Speed Quantum Well Lasers," *Appl. Phys. Lett.*, vol. 59, pp. 1-3, 1991.

39.   W. Rideout, W. F. Sharfin, E. Koteles, M. O. Vassell, and B. Elman, "Well-Barrier Hole Burning in Quantum Well Lasers," *IEEE Photon. Technol. Lett.*, vol. 3, pp. 784-786, 1991.

40.   K Kikuchi and T. Okoshi, "Measurement of FM noise, AM noise, and Field Spectra of 1.3 μm InGaAsP Lasers and Determination of the Linewidth Enhancement Factor," *IEEE J. Quantum Electron.*, vol. QE-21, pp. 1814-1818, 1985.

41.   J. E. Bowers, "High Speed Semiconductor Laser Design and Performance," *Solid-State Electron.*, vol. 30, pp. 1-11, 1987.

42.   R. Olshansky, P. Hill, V. Lanzisera, and W. Powazinik, "Universal Relationship Between Resonant Frequency and Damping Rate of 1.3 μm InGaAsP Semiconductor Lasers," *Appl. Phys. Lett.*, vol. 50, pp. 653-655, 1987.

43.   J. Eom, C. B. Su, J. S. LaCourse, and R. B. Lauer, "The Relationship of Doping Level to K Factor and the Effect on Ultimate Modulation Performance of Semiconductor Lasers," *Photon. Technol. Lett.*, vol. 2, pp. 692-694, 1990.

44.   R. Nagarajan, M. Ishikawa, and J. E. Bowers, "Effects of Carrier Transport on Relative Intensity Noise and Critique of K Factor Predictions of Modulation Response," *Electron. Lett.*, vol. 28, pp. 846-848, 1992.

45.   P. A. Morton, H. Temkin, D. L. Coblenz, R. A. Logan, and T. Tanbun-Ek, "Enhanced Modulation Bandwidth of Strained MQW Lasers," *Appl. Phys. Lett.*, vol. 60, pp. 1812-1814, 1992.

46.   T. Ishikawa, R. Nagarajan, and J. E. Bowers, "Theoretical Study on the Structure Dependent Characteristics of 1.55 µm InGaAsP/InP Multiple Quantum Well Lasers," to be published.

47.   C. B. Su and V. Lanzisera, "Effects of Doping Level on the Gain Constant and Modulation Bandwidth of InGaAsP Semiconductor Lasers, *Appl. Phys. Lett.*, vol. 45, pp. 1302-1304, 1984.

48.   K. Uomi, T. Mishima, and N. Chinone, "High Speed Modulation Capacity (>30 GHz) of Multi-Quantum Well Lasers - Modulation Doped Multi-Quantum Well Laser," *Proc. Thirteenth European Conf. on Optical Commun.*, vol. 3, pp. 29-32, 1987.

49.   K. Uomi, T. Mishima, and N. Chinone, "Modulation-Doped Multi-Quantum Well (MD-MQ) Lasers. II. Experiment," *Jpn. J. Appl. Phys.*, vol. 29, pp. 88-94, 1990.

50.   K. J. Vahala and C. E. Zah, "Effect of Doping on the Optical Gain and the Spontaneous Noise Enhancement Factor in Quantum Well Amplifiers and

Lasers Studied by Simple Analytical Expressions," *Appl. Phys. Lett.*, vol. 52, pp. 1945-1947, 1988.

51. R. J. Nelson and N. K. Dutta, "Calculated Auger Rates and Temperature Dependence of Threshold for Semiconductor Lasers Emitting at 1.3 and 1.55 μm," *J. Appl. Phys.*, vol. 54, pp. 2923-2929, 1983.

52. C. H. Henry, B. F. Levine, R. A. Logan, and C. G. Bethea, "Minority Carrier Lifetime and Luminescence Efficiency of 1.3 μm InGaAsP-InP Double Heterostructure Layers," *J. Quantum Electron.*, vol. QE-19, pp. 905-912, 1983.

53. R. Olshansky, C. B. Su, J. Manning, and W. Powazinik, "Measurement of Radiative and Nonradiative Recombination Rates in InGaAsP and AlGaAs Light Sources," *J. Quantum Electron.*, vol. QE-20, pp. 838-854, 1984.

54. W. H. Cheng, K. D. Buehring, A. Appelbaum, D. Renner, S. Shin, C. B. Su, A. Mar, and J. E. Bowers "High Speed and Low Relative Intensity Noise 1.3 μm InGaAsP Semi-Insulating Buried Crescent Lasers," *J. Quantum Electron.*, vol. 27, pp. 1642-1647, 1991.

55. M. Sugano, H. Sudo, S.Soda, T. Kusunoki, and H. Ishikawa, "Effects of Zinc Doping in DFB Lasers Emitting at 1.3 and 1.55 μm," *Electron. Lett.*, vol. 26, pp. 95-96, 1990.

56. C. B. Su and V. A. Lanzisera, "Ultra-High-Speed Modulation of 1.3-μm InGaAsP Diode Lasers," *J. Quantum Electron.*, vol. QE-22, pp. 1568-1578, 1986.

57. C. E. Zah, R. Bhat, S. G. Menocal, F. Favire, N. C. Andreadakis, M. A. Koza, C. Caneau, S. A. Schwarz, Y. Lo, and T. P. Lee, "Cavity length and Doping Dependence of 1.5-μm GaAnAs/GaInAsP Multiple Quantum Well Laser Characteristics," *Photon. Technol. Lett.*, vol. 2, pp. 231-233, 1990.

58. P. J. Thijs and T. Van Dongen, "High Quantum Efficiency, High Power, Modulation Doped GaInAs Strained Layer Quantum Well Laser Diodes Emitting at 1.5-μm," *Electron. Lett.*, vol. 25, pp. 1735-1737, 1989.

59. S. W. Corzine, R. H. Yan, and L. Coldren, "Optical Gain in III-V Bulk and Quantum Well Semiconductors," from <u>Quantum Well Lasers</u> (P. Zory, Ed.), Academic Press, New York, 1993, pp. 17-96.

60. H. Schneider and K. v. Klitzing, "Thermionic Emission and Gaussian Transport of Holes in a GaAs/$Al_xGa_{1-x}As$ Multiple-Quantum-Well Structure," *Phys. Rev.*, vol. B 38, pp. 6160-6165, 1988.

61. D. Coblentz, T. Tanbun-Ek, R. A. Logan, A. M. Sergent, S. N. G. Chu, and P. S. Davisson, "Strained Multiple Quantum Well Lasers Emitting at 1.3 μm Grown by Low-Pressure Metallorganic Vapor Phase Epitaxy," *Appl. Phys. Lett.*, vol. 59, pp. 405-407, 1991.

Chapter 3

Laser Fabrication

3.1 Semi-Insulating Properties of Fe-doped InP

An important consideration for any buried heterostructure laser is the method of current confinement. Insufficient current confinement leads to higher threshold, lower efficiency and increased device heating. All three effects degrade the laser's static characteristics by decreasing the amount of available output power at a given input current. If the maximum available output power is sufficiently reduced, then the resonance frequency and maximum modulation bandwidth will be reduced as well. In addition, increased device heating also indirectly reduces the dynamic characteristics through a reduction in the differential gain of both bulk and MQW lasers.

One of the most effective and common means of providing current confinement in buried heterostructure (BH) lasers is etching a mesa in the *p-i-n* base material and regrowing with reverse-biased *p-n* junctions. The drawback to this technique is the large amount of parasitic capacitance associated with the depletion layers of the reverse-biased junctions. For this reason, Fe-doped semi-insulating (SI) InP layers were developed as a replacement for *p-n* junctions [1, 2, 3, 4, 5, 6]. SI layers have been shown experimentally to be effective in improving the modulation performance of InGaAsP lasers via a reduction in the parasitic capacitance [7, 8].

To achieve semi-insulating properties InP is doped with a transition metal, which acts as a deep donor or acceptor. Several transition metals have been studied
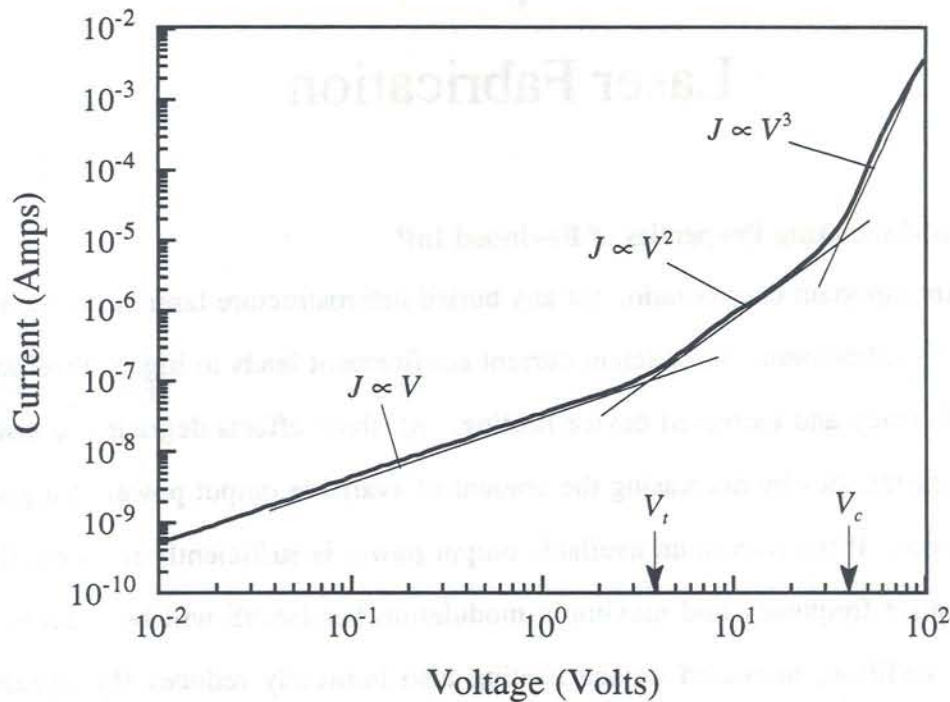
Figure 3.1   Current-voltage characteristic of a 3 μm thick SI InP layer. The layer was grown using

low-pressure MOCVD and iron pentacarbonyl as the dopant source. See Reference [6]

for details. Straight lines represent, linear, quadratic and SCL regimes.

for use in semi-insulating material, such as Fe [1-6], Co [9, 10, 11, 12, 13] Cr [11,

13], Mn [13], and Ti [13, 14, 15]. Of these dopants, iron has been found to produce

the highest resistivities, between 10^8 and 10^9 Ω-cm, followed by cobalt with

resistivities of 10^5 Ω-cm. All of the SI layers used in this study were doped with iron.

The I-V characteristic of a high quality SI InP layer is shown in Figure 3.1.

For electrical evaluation purposes, a nonalloyed, 200 nm-thick Au film was

evaporated on the backside of the n^+ substrate and nonalloyed 200 nm-thick Au dots

of 20 mil diameter were evaporated on the semi-insulating surface. The measured

I-V data for the Fe-doped layers are consistent with Lampert's theory of single

68

carrier injection into an insulator with a single trap level [16]. This theory predicts three regimes as the voltage increases: a linear or "ohmic" regime, a shallow-trap square law or "transition" regime, and a trap-free or "space-charge limited (SCL)" regime. In the ohmic regime, current flow results from the thermally generated free carriers. In the transition regime, current flow is limited by the recombination of injected electrons and holes through the deep Fe acceptors. In the trap-filled regime, the deep Fe acceptors are completely filled and the SI layer becomes conductive.

The transition voltage, V_t, is defined as the voltage at the intersection on a log-log plot of the two extrapolated straight lines representing the linear current regime and the transition current regime [16, 17]. It may be written as

$$V_t = \tfrac{9}{8}(d_{SI}^2/\theta\mu_n \tau_n),$$

with

$$\theta = (\rho_c/lN_t)\exp(E_t - E_c/kT),$$

where d_{SI} is the thickness of the SI layer, μ_n is the electron mobility and τ_n is the electron carrier lifetime. ρ_c, N_t, l, E_c, E_t, k and T are the effective density of states, the electron trap concentration, the degeneracy of the trap level E_t, the energy of the bottom edge of the conduction band, the energy of the electron trap levels, the Boltzmann constant, and the temperature, respectively. V_t was determined to be 3.6 V at 25 °C for 3.8 µm thick Fe-doped layers [4]. It can be seen from the above equations that high transition voltages require thick Fe-doped layers and high trap concentrations.

The critical voltage, V_c, is defined as the voltage at the intersection on a log-log plot of the two extrapolated straight lines representing the transition current
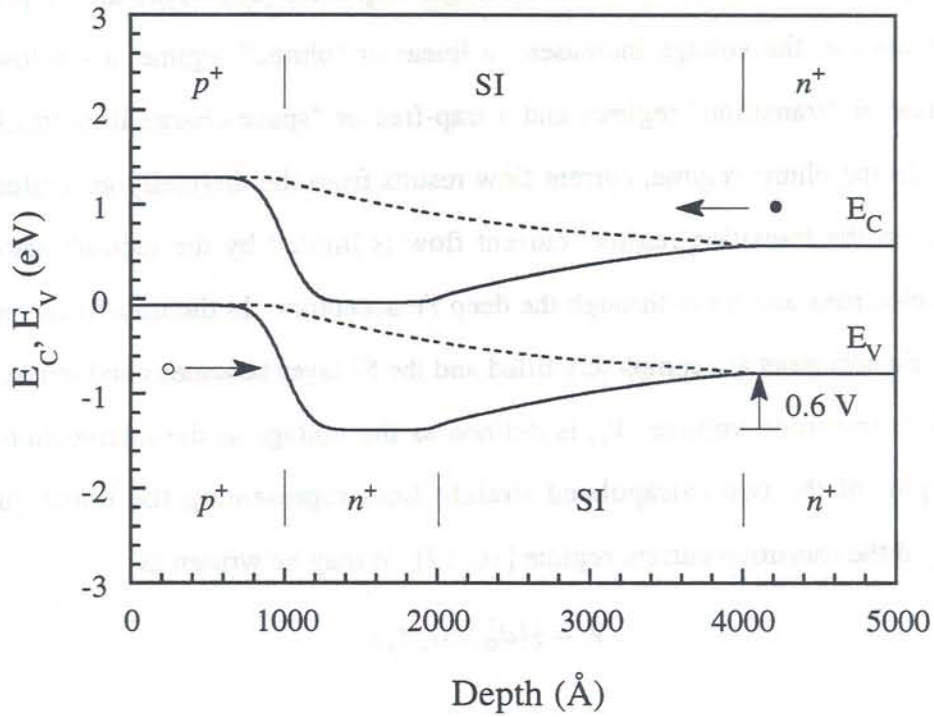
Figure 3.2   Calculated band diagrams for SI-based blocking layers under 0.6 V forward bias. The
             upper, dashed lines represent p^+-SI-n^+ blocking layers. The lower, solid lines represent
             p^+-n^+-SI-n^+ blocking layers. Holes are injected from the left, electrons from the right.

regime and the SCL current regime [17, 18]. In this case, the critical voltage is

related to the Fe acceptor concentration, N_t, by

$$V_c = (qd_{SI}^2/2\varepsilon)(N_t - N_d),$$

where q, ε, and N_d are the electron charge, the dielectric permitivity, and the

background electron concentration, respectively. In this work, V_c was determined to

be 70 V for 3.8 μm thick Fe-doped layers [4]. It is evident from the above equations

that, in order to obtain effective current blocking characteristics, the SI layers must

have sufficient thickness to achieve high critical voltage.

70

Another consideration of some importance is the phenomenon of double injection [19]. This refers to the situation where SI InP is sandwiched between n and p-type layers. As a bias is applied, both electrons *and* holes are injected into the material and the deep acceptor levels act as efficient recombination sites. When this happens the resistivity of the layers as well as the transition and critical voltages drop considerably. The critical or "trap filled limit" voltage can fall to below 1.5 V [20] This has implications for bipolar devices, such as laser diodes, where the semi-insulating layer is sandwiched between p and n-type layers. In order to keep the critical voltage high, it is important to eliminate the p-type/semi-insulating interface.

One proposed solution to the problem of double injection is the insertion of a thin n^+ layer between p and SI layers [21]. In this technique, double injection is reduced due to the potential barrier for holes created by the n^+ layer. Figure 3.2 shows simulated band diagrams for p^+-SI-n^+ and p^+-n^+-SI-n^+ diode. The potential barrier for holes due to the additional n^+ layer is clearly visible.

3.2 Enhanced Diffusion of Fe-doped InP Layers

Diffusion of dopants throughout a laser structure is a major concern in any laser process design, but it is of special concern for SI InP lasers. Enhanced diffusion has been found to occur between adjacent Zn and Fe doped layers. Young and Fontijn [22] found anomalous diffusion of iron from SI InP into a Zn-bearing layer. In their structure, the iron concentration in the Zn-doped InP reached a level which exceeded that of the intentionally Fe-doped material, effectively annihilating the semi-insulating character of the Fe-doped layer. Enhanced diffusion in the reverse direction has also been observed [21, 23, 24]. Zn-diffusion into a Fe-doped SI layer at temperatures near 600 °C was found to be a relatively fast process, with a diffusion

71
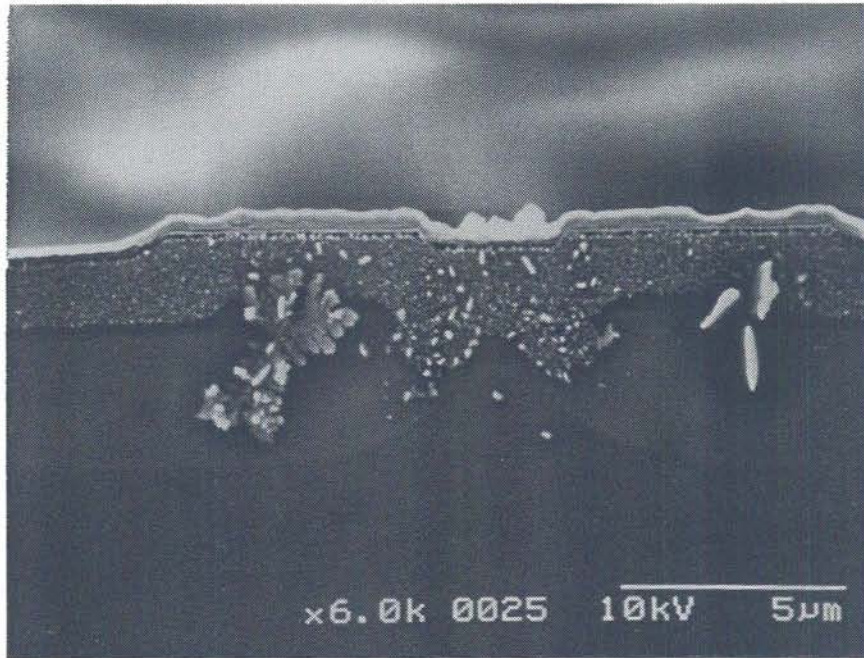
Figure 3.3   Cross-sectional SEM micrograph of CMBH structure with SI/n^+ blocking layers. The device has been stained to show the structural detail. The n-substrate appears dark, the SI layer appears lighter, the n^+ layer and active area appear very dark, and the p-cladding layer is distinguished by a crystalline residue.

coefficient in the range of 10^{-10} - 10^{-11} cm^2/s [21, 23]. These values are approximately two orders of magnitude higher than the reported Zn diffusion coefficient without the presence of Fe-doped layers [25]. Both Zn and Fe accumulation at the p-SI interface were observed [22]. Possible mechanisms for enhanced Zn/Fe diffusion include interstitial/lattice exchange [21] or interstitial/interstitial compensation [22]. Whatever the mechanism, the interdiffusion of Zn and Fe dopants destroys the conductivity and semi-insulating properties of p-type and SI InP layers, respectively. In addition, Zn and Fe dopant accumulation at the interface may provide significant double injection leakage paths in bipolar device structures. In order to preserve the conducting and semi-insulating character of both materials, there should be no direct contact of the Zn-doped layer with Fe-doped InP.

72

The same n^+ layer used to prevent double carrier injection as discussed in the previous section has applications to the problem of enhanced Zn and Fe interdiffusion. An n^+ layer inserted between adjacent p and SI type layers serves to shield the interstitial Zn and Fe atoms from each other so that enhanced diffusion does not occur. Figure 3.3 shows a cross-sectional SEM micrograph of a CMBH structure in which a 0.3 μm n^+ layer has been grown between the SI blocking and p-type cladding layers. The sample has been stained to show the layer structure. It can be seen that the p-type material ends abruptly at the interface of the n^+ layer, except in the vicinity of the active area where the n^+ layer disappears. In this area, it appears that some Zn diffusion has occurred and that the material surrounding three sides of the active area is p-type. Although the additional n^+ layer minimizes the area of contact between Zn and Fe-doped layers, due to the nature of selective regrowth it is not entirely eliminated. Thus, a small leakage path may still exist around the active area.

To review, the requirements for the effective use of Fe-doped current blocking layers are that they have high trap density, sufficient thickness, and do not come in contact with Zn-doped layers. With these requirements in mind, we now compare the relative merits and static performance of several types of SI InP lasers.

3.3 Design of High Speed Laser Structures Employing Semi-Insulating InP Current Blocking Layers

The incorporation of semi-insulating InP into buried heterostructures has been studied extensively. The laser designs can be grouped by the number of regrowths used in the device fabrication: no-regrowth [26, 27], single-regrowth [28, 29, 30, 31, 32], double regrowth [7, 33], and triple regrowth [34]. The preceding references are

73

only representative examples of different device structures and do not constitute an exhaustive list. Increasing the number of regrowths reduces the parasitics and/or adds functionality to the device. However, there is a tradeoff between design simplicity leading to ease of fabrication on the one hand, and increased complexity leading to increased device performance and decreased process yield on the other. Regrowth processes, in particular, tend to be yield-limiting processes.

Although all laser structures have design limits, there are several overriding concerns which may be addressed at the outset and which narrow the field of possible structures considerably. In general, device planarity is desirable for reliability, thermal conductivity (active area surrounded by high thermal conductivity material) and packaging purposes (e.g. flip-chip bonding for better thermal heat sinking). In addition, planar active areas are desirable for the possible incorporation of quantum wells and DFB gratings. V-groove, or buried crescent lasers, for example, cannot accommodate uniform quantum wells. We therefore restrict our attention to those designs in which the active area is deposited in the initial, planar growth. This, in turn, necessitates at least one regrowth or mass transport process for the creation of strong index guiding. We will further restrict our attention to lasers which incorporate at least one semi-insulating material regrowth.

We now consider three types of planar buried heterostructures: the semi-insulating planar buried heterostructure (SIPBH), the etched mesa buried heterostructure (EMBH), and the cap mesa buried heterostructure (CMBH). The three structures are illustrated schematically in Figure 3.4. In an effort to retain as much design simplicity and ease of fabrication as possible, we begin with the simplest of regrown structures and proceed toward more complex designs. We demonstrate

74
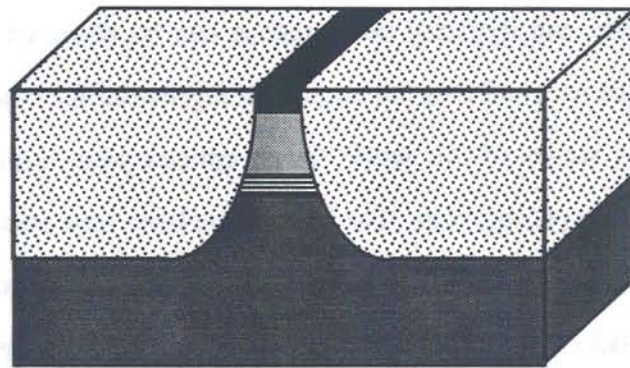
(a)
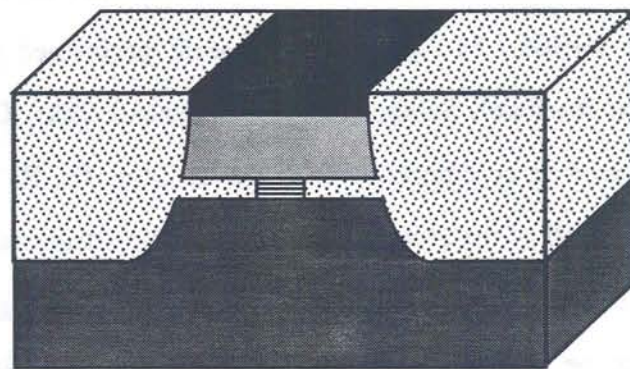
(b)
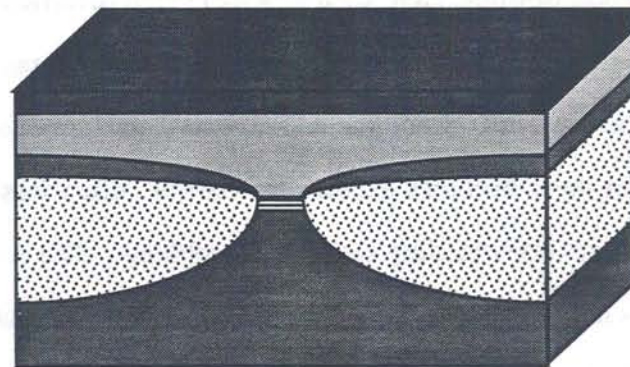
(c)

| ▨ n InP | ░░ SI InP | ▨ p InP | ■ InGaAs | ▤ MQW active |

Figure 3.4 Cross-sectional schematic diagrams of the three SI laser structures investigated: (a) the Semi-Insulating Planar Buried Heterostructure (SIPBH), (b) The Etched Mesa Buried Heterostructure (EMBH) and (c) the Cap Mesa Buried Heterostructure.

75

how increased static and dynamic performance can be obtained by increasing the complexity of the device, and thus the number of regrowths necessary for fabrication.

In the early stages of this work design options were limited to those lasers with a single SI or n-type regrowth. The bulk active layer base structure was obtained from AT&T Bell Laboratories. The p-contact layer of the base material consists of heavily doped InGaAs ($p = 5 \times 10^{18}$ cm^{-3}). This allows only one type of etched mesa to be fabricated, sometimes known as the semi-insulating planar buried heterostructure or SIPBH. SI-type regrowths were performed in a low-pressure MOCVD reactor at Rockwell Science Center, Thousand Oaks, CA. Work on the SIPBH was performed in collaboration with Dr. S. Zehr, Dr. R. T. Huang and W. Burke. While having all of the aforementioned desirable attributes, the structure has at least three severe drawbacks. The first is that in order to obtain good regrowth, the mesa profile has to be smooth, monotonic and free of kinks. While this is quite achievable with a good isotropic etch, such as KKI [35], it invariably leaves the top of the mesa smaller than the bottom. In particular, the p-contact layer is always narrower than the active area. Since the active area is designed to be 1 - 1.5 μm in width, the p-contact layer becomes excessively narrow, often less than 1 μm. This presents severe contact and cladding resistance problems. The second drawback is that because the p-cladding layer is so narrow and is sandwiched laterally between SI InP layers, any increased resistance due to enhanced Zn or Fe diffusion is exacerbated. Lastly, current leakage due to double injection is a severe problem.

A second-generation SIPBH, dubbed the etched-mesa buried heterostructure (EMBH), seeks to solve the contact and cladding resistance problems by widening the mesa. This structure was pioneered by researchers at AT&T Bell Laboratories. The

particular EMBH lasers discussed here were fabricated in collaboration with Drs. R. Logan and T. Tanbun-Ek of Murray Hill, New Jersey. The wide mesa and narrow active area of the EMBH requires a selective undercut etch to reduce the lateral dimension of the active area. The high selectivity is provided by a p-contact layer with a larger bandgap (E_g = 1.08 eV) than that of the active area. The larger bandgap leads to higher specific contact resistance, r_c. (See Section 4.2 for contact resistivity values.) Despite the increase in r_c, the 5 to 12-fold increase in the width of the mesa reduces the overall contact resistance to 5 - 10 Ω. The problem of enhanced diffusion is addressed in two ways. First, the doping of the p-cladding layer is graded from undoped near the active area to heavily doped ($p = 2 \times 10^{19}$ cm^{-3}) in the p-contact layer. This reduces enhanced diffusion in the lower half of the cladding layer, where it is most important. Second, the increased width of the mesa allows for some Zn/Fe interdiffusion at the edges of the mesa without significantly affecting the overall contact and cladding resistance.

Although optimization of the EMBH structure was pursued for some time, it is apparent that it, too, has some inherent design problems. First, the mesa is literally upside-down. That is, the preferred mesa taper for low contact resistance and good current channeling into the active area is reentrant, one that starts wide at the top and narrows as it approaches the active area. The shape of the EMBH mesa allows for a large amount of current spreading, and thus current leakage, around the active area. Likewise, the large area of contact between p and SI-type layers promotes current leakage via double injection. Also, the wide apron of the mesa just above the active area, coupled with the very thin SI layer between p and n cladding layers, is a large source of parasitic capacitance. Finally, the mesa etch depth and MOCVD regrowth

77
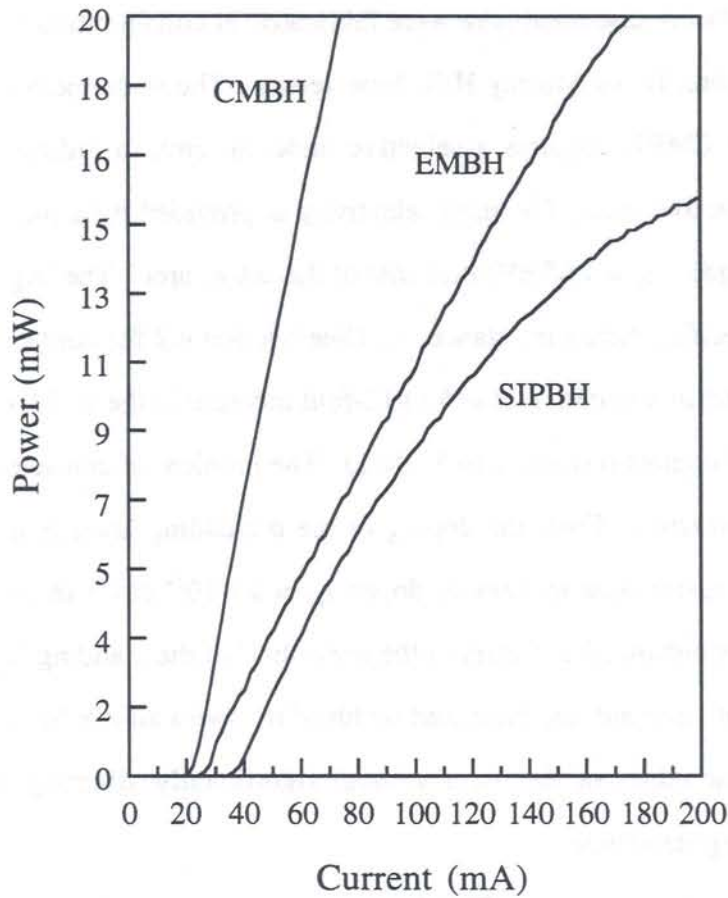
Figure 3.5   Light output under pulsed operation for CMBH, EMBH and SIPBH.

parameters become highly critical in order to suppress voids which may form at the corners of the mesa.

A two-regrowth structure called the cap-mesa buried heterostructure (CMBH) was designed to circumvent these problems. The CMBH laser was also designed at AT&T Bell Laboratories. The CMBH lasers in this work were fabricated in collaboration with Drs. Logan and Tanbun-Ek. The CMBH incorporates a reentrant p-cladding taper, very little contact between p and SI type layers, thick SI layers

78

between n and p-type cladding, and much less propensity to form voids during the selective regrowth step. An additional n^+ layer was inserted in between the p and SI type layers to prevent double injection and enhanced diffusion.

Figure 3.5 shows the pulsed P-I characteristics of the three types of laser structure. Both the SIPBH and EMBH lasers suffer from a large current leakage due to double injection. The rollover in the P-I curve is most pronounced for the SIPBH. In contrast, the CMBH exhibits a very linear response to the bias current at similar power levels. The forward device resistance, measured at 50 mA dc bias, was found to be 15 - 20 Ω for the SIPBH (L = 500 μm), 5 - 10 Ω for the EMBH (L = 370 μm), and 5 - 7 Ω for the CMBH (L = 360 μm). The smaller series resistance values of the CMBH are due to a combination of the smaller contact resistance and reduced interdiffusion of Zn and Fe between p and SI layers. We conclude that the CMBH is the best structure for linearity and reduced parasitic resistance. The remainder of this dissertation will focus exclusively on the CMBH laser.

3.4 MOCVD Growth

The base material for all three structures is grown by metalorganic chemical vapor deposition (MOCVD). A diagram of the MOCVD system is shown in Figure 3.6. The basic system consists of a series of metalorganic sources, each of which is plumbed with a source of high-purity hydrogen gas. The hydrogen gas is bubbled through a stainless steel container containing the liquid metalorganic source. This produces a gaseous phase containing metal-hydrocarbons and hydrogen. This gas is precisely combined in various concentrations with arsine and phosphine to form the desired compound at the surface of the substrate. The vapors are mixed in a reverse flow mixing nozzle located 6 inches upstream from the growth chamber to

79
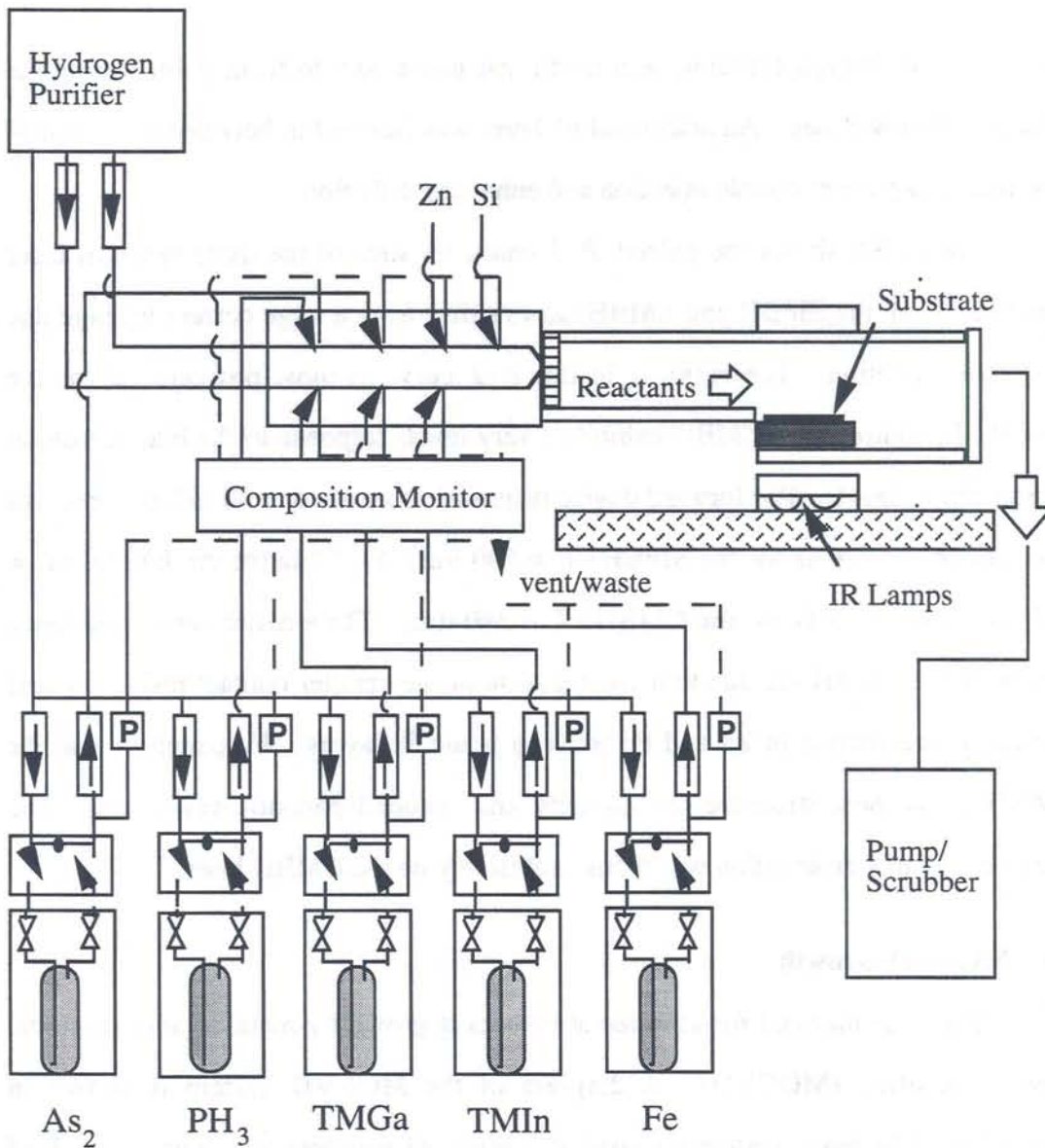
Figure 3.6   Schematic diagram of MOCVD system.

insure uniform epitaxy. The growth chamber consists of a quartz tube in which a graphite susceptor carrying the substrate is placed. The susceptor and substrate are heated, either inductively or through the use of tungsten-halogen heat lamps. As the gases reach the substrate they are pyrolized by the hot surface. That is, the various

chemical bonds are broken, the heavy metals deposit on the surface and the volatile hydrocarbons desorb. The uniformity of the resulting film is a function of the kinetics of the gas/surface reactions and the boundary layer formation. For most growth chamber configurations lower pressure and higher gas velocities can increase the uniformity. All of the growth conditions here involve low-pressure MOCVD.

3.5 Selective Regrowth

Perhaps the most critical step common to the fabrication of all three types of laser structure is the selective regrowth step. Selective, planar regrowth has been demonstrated using both MOCVD [36, 37, 38, 39, 40, 41, 42, 43, 44] and Hydride VPE [45]. For MOCVD, the quality of the regrowth has been found to be extremely sensitive to the shape of the mesa, the extent of the etch mask overhang, the depth of the mesa, the growth temperature, the growth rate, the reactor pressure, the In source, the ratio of coated to uncoated surface, the etch method and even the reactor geometry. The best growth conditions found in this study were reported in Reference [41]. The optimum growth temperature, reactor pressure and growth rate were found to be 600 °C, 60 Torr, and 0.055 μm/min., respectively. Furthermore, it was found that the presence or absence of polycrystalline InP layers deposited on the mask depended on the indium source, but not on the mask material. When triethylindium (TEI) was used for the regrowth, polycrystalline InP was observed on the mask no matter which mask material was used (SiO_2 or Si_3N_4). In contrast, when trimethylindium (TMI) was used as the indium source, no polycrystalline InP was observed on the mask regardless of mask material. In addition, the regrowth was found to be extremely sensitive to the mesa shape. Mesa profiles with corners or notches, such as the rectangular, trapezoidal or reentrant varieties, were found to

81

exhibit "rabbit ears" and/or deep grooves around the edges of the mask after regrowth. Only mesa profiles with smooth, monotonic sidewalls exhibited planar, groove-free regrowth. Finally, using ideal mesa profiles and growth conditions, it was found that planar regrowth of InP could be achieved for mesa structures with an overhang length as long as 2.6 μm and a mesa height as high as 4 μm. The minimum amount of overhang necessary to avoid overgrowth on the mask was found to be about 0.5 μm. Thus, a great degree of control over the undercut and profile of the mesa is necessary for good regrowth quality and reproducibility.

The morphological properties of the regrowth differ markedly between MOCVD and Hydride VPE. In particular, the Hydride VPE technique is reported to be relatively insensitive to parameters such as mesa sidewall shape and the extent of the etch mask overhang [45, 46]. Excellent mesa sidewall coverage with no void formation, no mask overgrowth, and good surface morphology in the field regions between mesas has been demonstrated. This technique has been used to fabricate double-regrowth, SI lasers with -3 dB bandwidths of 18 GHz [47].

3.6 CMBH Fabrication

The CMBH is a three-growth structure. The base material growth and subsequent selective and non-selective regrowths are outlined in Figure 3.7. The first growth is performed on a bare n-InP substrate and consists of a 0.5 μm thick, n-InP buffer layer doped at 1×10^{18} cm^{-3}. The bulk or MQW active area, including any SCH regions, is grown next. Finally, a thin 50 nm undoped cap layer is grown on top of the active area. The structure is then covered with oxide which is patterned into 2 μm stripes. Selective and non-selective wet chemical etchants are used to form a smoothly varying mesa which undercuts the oxide. The final mesa prior to regrowth
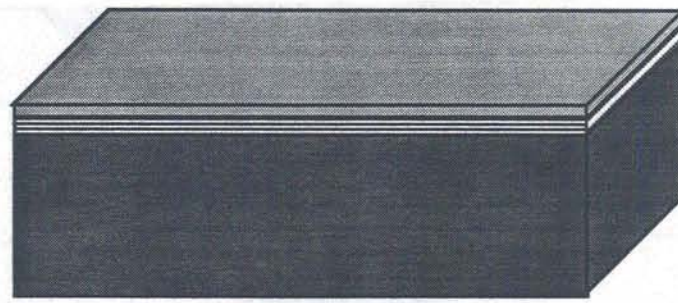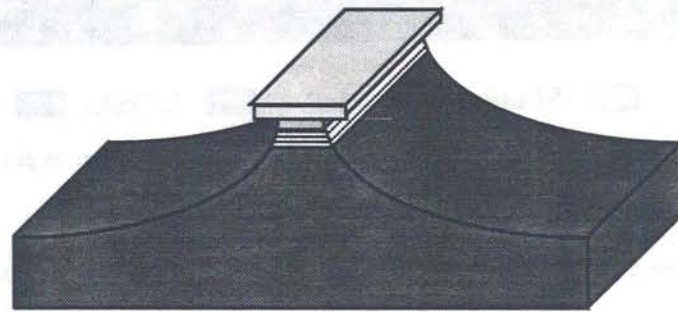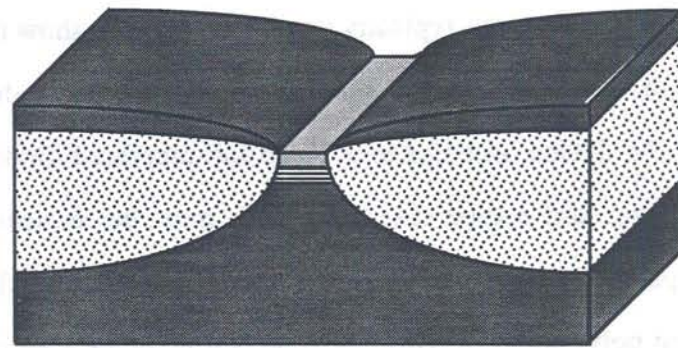
Figure 3.7   Three MOCVD growths of the CMBH. (a) Base material (b) First regrowth
(selective). (c) Second regrowth (non-selective).

is shown in Figure 3.7 (b). A selective regrowth is performed in which the blocking
and *n*-type layers are grown everywhere except on the oxide. Once the regrowth is
completed, the oxide is removed in HF and the wafer is reloaded into the MOCVD
chamber. Figure 3.7 (c) shows the wafer just after oxide removal. The second

83

■ *n* InP   ▒ SI InP   ▢ *p* InP   ■ InGaAs   ▤ MQW active
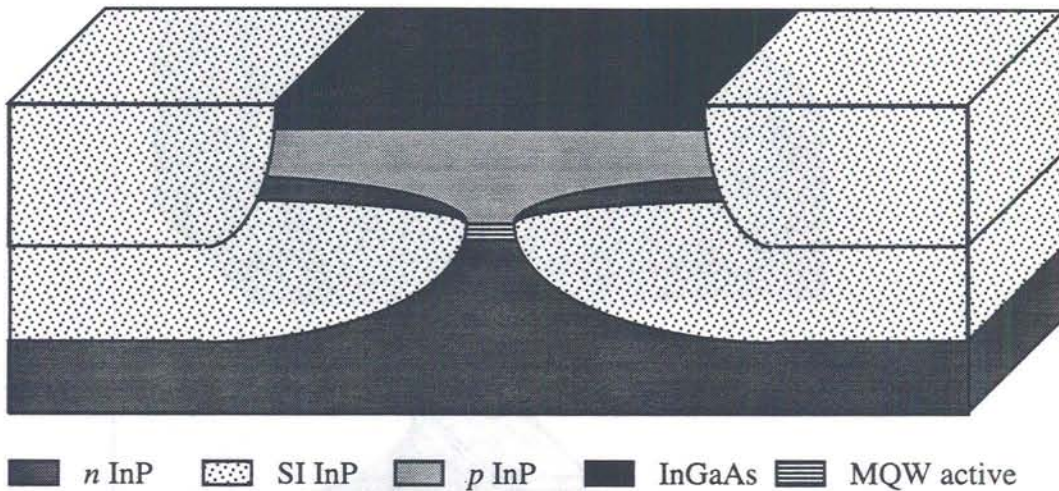
Figure 3.8   Triple regrowth structure of Reference [34]. The structure is planar and contacts may be deposited directly on the semiconductor surface.

regrowth is non-selective and adds the *p*-type cladding and *p*-contact layers to the structure. In general, this regrowth can planarize small ripples in the surface, although large surface features, typically larger than 0.5 μm, show through.

Although the use of SI InP blocking layers greatly reduces the parasitic capacitance of the device, in order to achieve sub-picofarad diode capacitances the area of the contact and *p*-type cladding layers must be reduced. One approach reduces the capacitance by reducing the area of the contact and cladding layers and planarizing with polyimide [7]. Another approach involves a second mesa etch and selective regrowth as described above, only this time using a larger mesa width [34]. The final structure, shown in Figure 3.8, is planar and contacts can be deposited directly onto the semiconductor surface. Both approaches produce parasitic capacitances of less than 2 pF. The former approach is adapted for use in this work.

Processing begins with the structures shown in Figure 3.9. The first step, shown in Figure 3.9 (a), is to pattern a liftoff mask for a 5 μm stripe centered over the active area. The Ti/Pt/Au contact metallization described in Section 4.4 is then

deposited with a Au layer thickness of 110 nm and the addition of a 30 nm Ti layer. The total metallization thickness is 200 nm. This metallization is then used as a self-aligned mask for the subsequent reactive ion etching (RIE) of the cap and cladding layers. The top Ti layer is used as a protective mask against Ar sputtering of the Au. A methane-hydrogen plasma is used to etch all InGaAsP compounds. Because polymerization of the surface may occur under some etch conditions, it is necessary to add some Ar to assist the desorption of the non-volatile species. The optimum flow ratio for etching is $CH_4/H_2/Ar$, 4/20/10 sccm. For a standard parallel plate reactor geometry, the anisotropy of the etch depends on the accelerating voltage and the chamber pressure. It was found that the most vertical sidewalls occurred for V_{bias} = -500 V and a pressure of 125 mT. The forward RF power varied between 155 and 170 W. The typical etch rate for InP was approximately 70 nm/min. The etch depth was determined by surface profilometer. The final etch profile is shown in Figure 3.9 (b). As a final step, the wafers are cleaned in an O_2 plasma for 15 min. to remove residual polymer. The Ti cap layer is removed in 15 sec. of a BHF etch.

The different structures of Figure 3.10 require different etch depths for capacitance reduction. The simple SI/n-type blocking layer structure of Figure 3.10 (a) requires only that the etch stop somewhere in the SI layer to completely isolate the contact. This depth is typically ~2.5 µm. The structure of Figure 3.10 (b), however, requires etching completely through to the substrate, an etch depth of ~6.0 µm, in order to minimize the capacitance of the reverse biased p-n blocking layers. The resulting structures are very non-planar. This presents a problem for metal step coverage. Also of consideration is the goal of keeping the bond pad capacitance low by applying a thick dielectric between substrate and bond pad. This

85

Legend:
- ■ n InP
- ▨ p InP
- ▦ SI InP
- ■ InGaAs
- ▤ MQW active
- ▨ Ti/Pt/Au
- ▨ Polyimide
- ▨ Resist

(a)

(b)

(c)
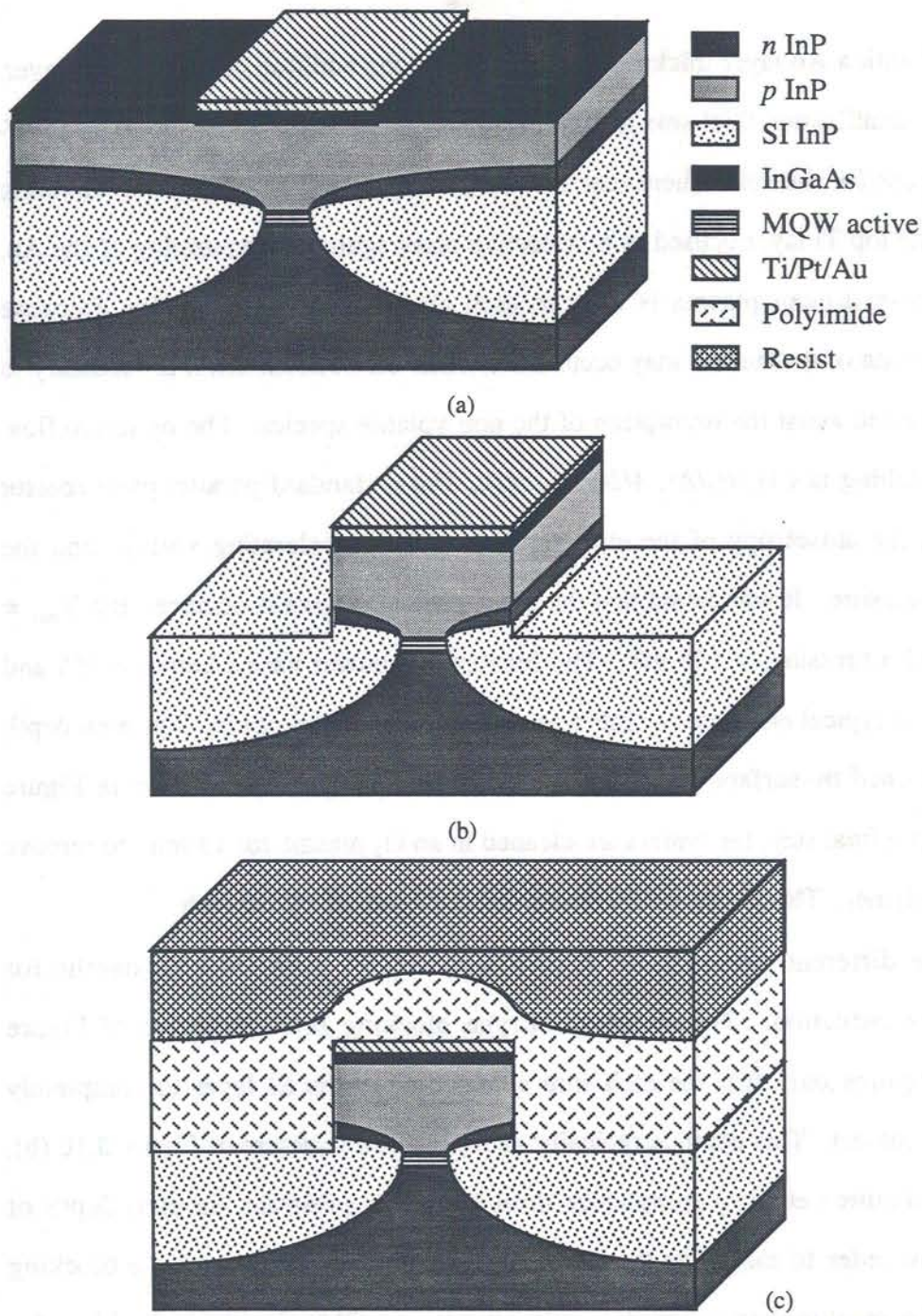
Figure 3.9   Post-regrowth processing for the high-speed CMBH. (a) Deposition and patterning of
p-contact metal/RIE etch mask. (b) CH$_4$-H$_2$ RIE etch. (c) Polyimide deposition and
cure followed by resist planarization.

86
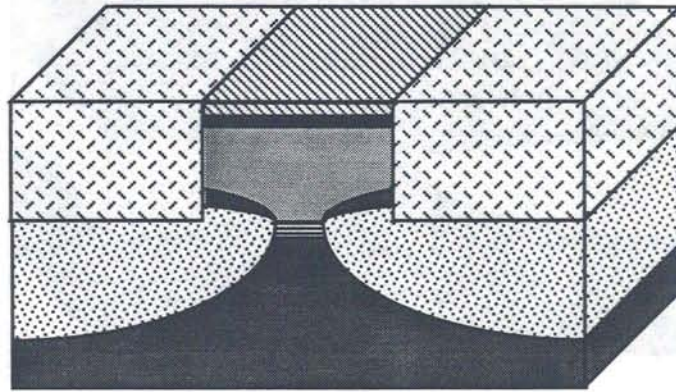
(d)
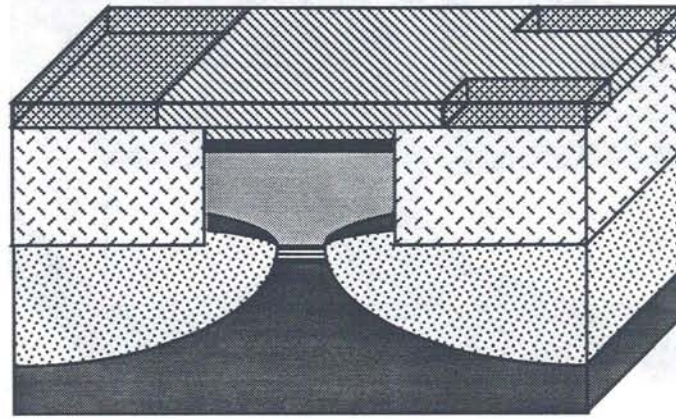
(e)
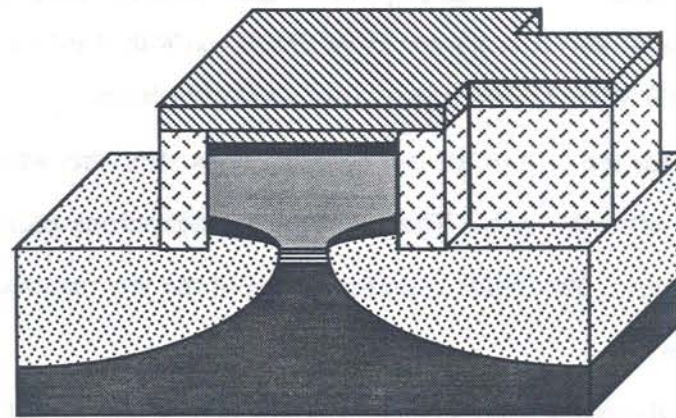
(f)

Figure 3.9   (d) O_2 plasma etch of resist and polyimide. (e) Plating through resist. (f) O_2 plasma
            etch of field polyimide.

87
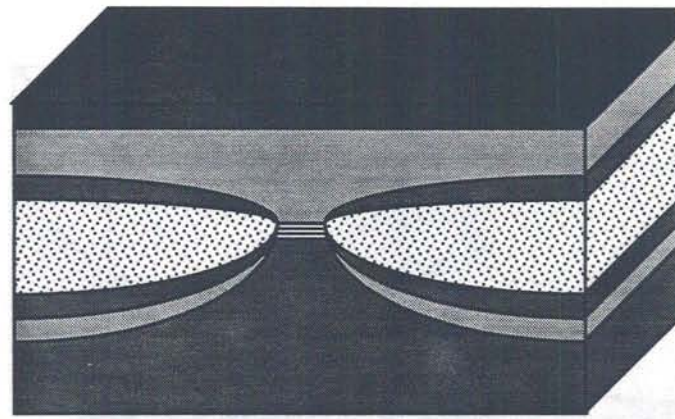
(a)
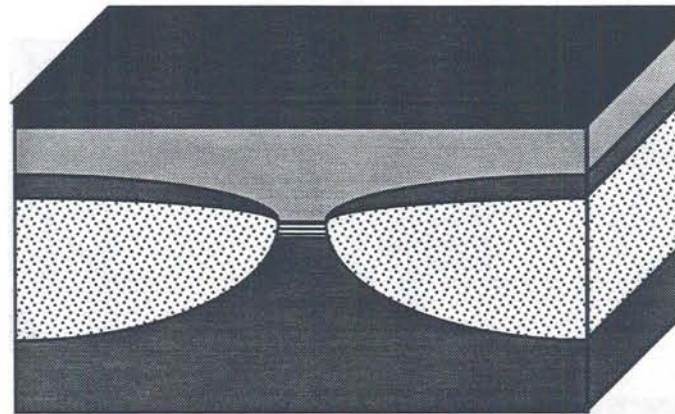
(b)

■ n InP ▦ SI InP ▨ p InP ■ InGaAs ≣ MQW active

Figure 3.10   Various blocking layer schemes for the CMBH. (a) With SI and n-InP blocking layers
only. (b) With additional reverse-biased p-n blocking layers.

is especially true for the case of the *p-n* blocking layer structure, where the substrate
itself is exposed after the etch. These design considerations require a thick, yet
planarizable dielectric. Polyimide is presently one of the few materials that can meet
these requirements.

Several polyimides were investigated for their planarization, dielectric and
mechanical properties. Probamide™ 284 was found to be the most ideal for its fair to
good planarization, low dielectric constant (n_r = 1.63), low cure temperature (320 °C)

88

and low elasticity. The thickness of the applied polyimide decreases with increasing spin speed. Since higher spin speeds reduce the effects of edge bead, it is preferable to apply several thin layers, rather than one thick one. However, the large mesa heights of both structures require multiple polyimide depositions and even multiple planarizations. The basic planarization process is as follows. The wafers are dehydration baked at 170 °C for 30 min. Probamide™ 3289 adhesion promoter is applied, followed immediately by Probamide™ 284, which is spun at 2000 - 3000 rpm to achieve a thickness of 2.5 - 3.0 μm. The degree of planarization at these spin speeds is typically 0 - 10%. The polyimide is then cured at 90 °C for 15 min. and at 150 °C for 15 min. The final cures take place in a N_2 ambient at 240 °C for 15 min. and 320 °C for 1 hour. Figure 3.9 (c) shows the wafer after polyimide deposition and cure.

A greater degree of planarization is achieved by spinning a thick photoresist layer (AZ 4330) on top of the polyimide at 4000 rpm. The photoresist is baked on a 100 °C hotplate for 1 min. One coat of resist can planarize a 2.5 μm ridge to about 0.5 μm. Two coats can planarize a 6 μm ridge to about 1.0 μm. Photoresist and polyimide etch in O_2 plasma at nearly the same rate. This allows planarization of the underlying polyimide to nearly the same degree as that of the photoresist [48]. A schematic diagram of the RIE chamber is shown in Figure 3.11. A HeNe laser is used to monitor the total etch depth. The etch rate varies from run to run and throughout each run, slowing slightly as the etch progresses. The color of the O_2 plasma changes noticeably, signaling possible contamination by etch byproducts. Despite the nonlinearity of the etch rate, the total etch depth may be accurately measured by counting the number of interference fringes that occur during the etch. The etch depth per fringe, d, may be calculated from the Bragg condition,

89
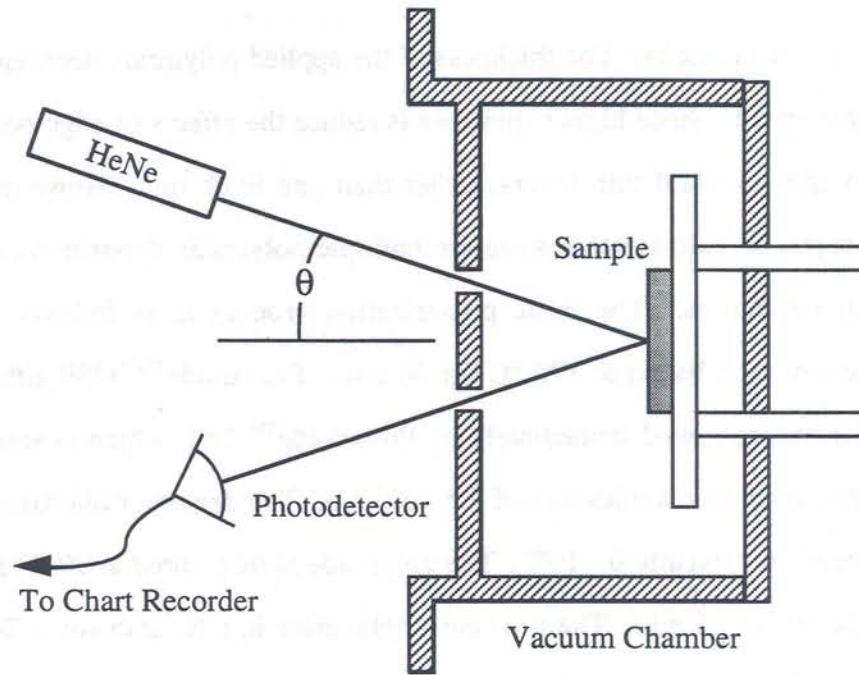
Figure 3.11   RIE chamber for O_2 plasma etching of resist and polyimide. A HeNe laser is used to
monitor the etch depth.

$$\lambda \cos \theta = 2 n_r d_{fr}.$$

For $\lambda = 632$ nm, $n_{r, \text{photoresist}} = 1.63$, and an angle of incidence, θ, of about 10 degrees,
$d_{fr} = 191$ nm/fringe. By knowing the thicknesses and planarity of the polyimide and
photoresist, the total desired etch depth may be calculated. The thickness and
planarity can be measured by Dektak surface profilometer.

After resist deposition the wafer is loaded into the RIE chamber. The wafer is
secured to the cathode with an electrically and thermally conducting paste. The RIE
chamber is evacuated to pressures between 1.5×10^{-6} and 5×10^{-7} Torr. The O_2 flow
rate is set to 7 sccm and the plasma etch is carried out at a pressure of 10 mTorr. The
cathode voltage is -200 V and the RF power is 60 W. After the RIE etch, the results
are monitored visually and with a Dektak profilometer. Figure 3.9 (d) shows the
planarized mesa structure. The Au mesa metal should be exposed and free of

90

polyimide residue. The Dektak should reveal a bump in the middle of polyimide several hundred nm high. If a small amount of further etching is required, it can be performed in the CH$_4$-H$_2$ RIE system using O$_2$ for a few seconds at a time without a large amount of contamination roughening the surface. This process is repeated until most of the wafer is clear. If it is important to remove the edge effect, then photolithography may be performed using an edge exposure mask. Thus, varying thicknesses of polyimide may be selectively removed from different parts of the wafer.

At this point the wafer is ready for bondpad metallization. Since significant surface steps up to 0.5 μm may still be present, it is necessary to use a fairly thick metal to ensure adequate step coverage. Liftoff metallizations are limited to about 400 nm and may therefore be inadequate. For this reason a two step, Au plating method is used. The first step is to sputter a thin or "flash" layer of metal over the entire wafer. The actual flash layer consists of 30 nm Ti, 200 nm Au, and 30 nm Ti. The first Ti layer is for promoting adhesion to the underlying Au and polyimide layers. The second Ti layer is for promoting photoresist adhesion during the plating process. The sputtering is carried out in a three target, magnetron sputtering machine. The Ar pressure is set to 100 mT to promote good sidewall coverage. RF power is 100 W for the Ti layers and 200 W for the Au layers. After flash layer deposition the wafer is liftoff patterned for plating. The plating setup is shown in Figure 3.12. The wafer is mounted to one of two Pt electrodes and both electrodes are immersed in a stirred and heated Au plating solution. The temperature of the solution is maintained between 45 and 47 °C. A DC current is passed between the electrodes with the negative bias applied to the substrate. The current necessary for a reasonable
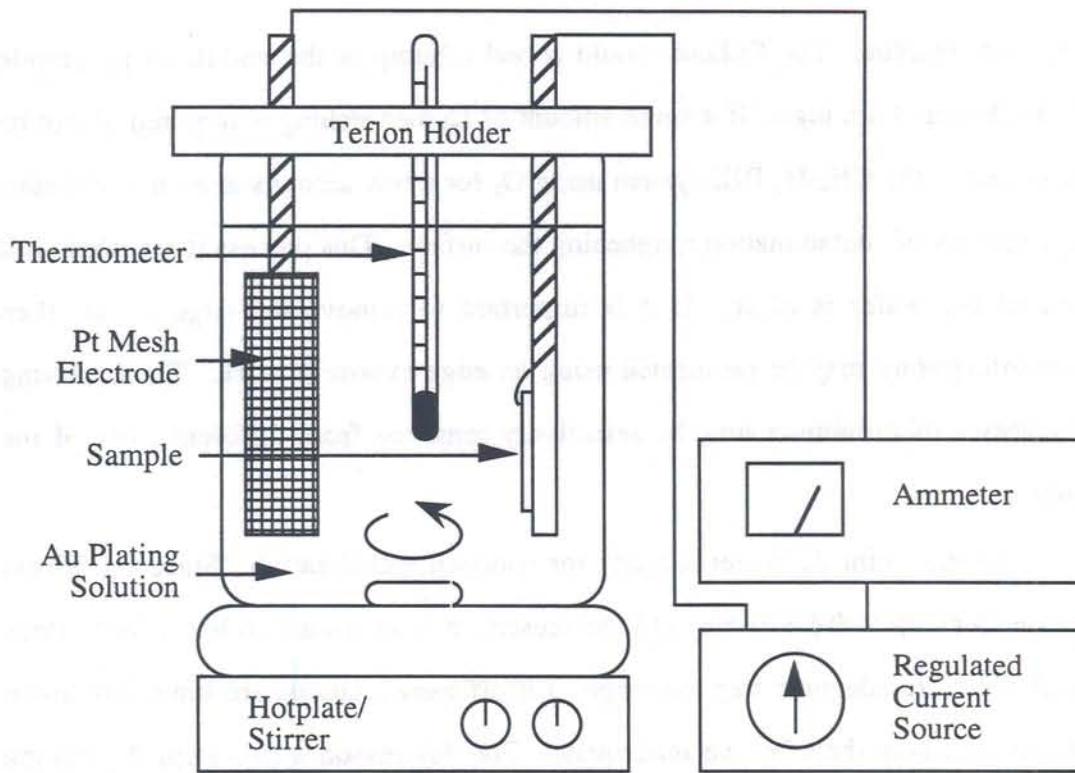
Figure 3.12 Plating system for laser wafers.

deposition rate, ~4 μm/hr, may vary with the age of the plating solution and the size of the substrate. However, a typical value for fresh plating solution is about 10 mA. If the deposition rate exceeds ~10 μm/hr, the resulting Au layer may turn a non-uniform brown and be of poor quality. Thus, it is important that the current source be regulated and the temperature and freshness of the plating solution be accurately maintained. The thickness of the Au layer is monitored by surface profiling through the resist mask. A 3 μm layer of resist is used as the mask and plating is stopped when the Au is flush with the resist, as shown in Figure 3.9 (e). The resist is then removed in acetone. The flash layer is removed with the following sequence of etches:

Layer	Etch	Time
Ti	HF:20H$_2$0	30 sec.
Au	KI:H$_2$0	2 min.
Ti	HF:20H$_2$0	30 sec.

It is important for cleaving purposes to remove as much of the excess polyimide as possible. This is achieved by etching in an O$_2$ plasma at 300 mT and 300 W for 30 min. During this process the metal acts as a self-aligned mask to protect the polyimide underneath the bond pads. The resulting structure is shown in Figure 3.9 (f). Once the excess polyimide is removed, the contacts are ready for annealing. The wafer is rapid thermal annealed in a N$_2$ ambient at 420 °C for 30 seconds.

3.7 Post-Anneal Processing

Prior to n-contact deposition, the wafer is thinned to improve both cleaving and heat sinking. Thinning involves a two-wax process. First, the wafer is mounted p-side down to a Si substrate with a high-temperature wax, also known as "crystal bond". This wax flows at about 200 °C and dissolves in acetone. The Si provides excellent flatness and mechanical stability for the lapping process. Care must be taken to make sure that there are no air bubbles underneath the wafer and that the wax extends all the way to the corners of the wafer, while at the same time minimizing the amount of excess wax around the wafer. Air bubbles will cause the wafer to collapse under the pressure of the lapping process, whereas excess wax will cause the wafer to stick to the lapping surface, causing uneven lapping and possible wafer breakage. Second, the mounted wafer is secured to the brass lapping block with a low
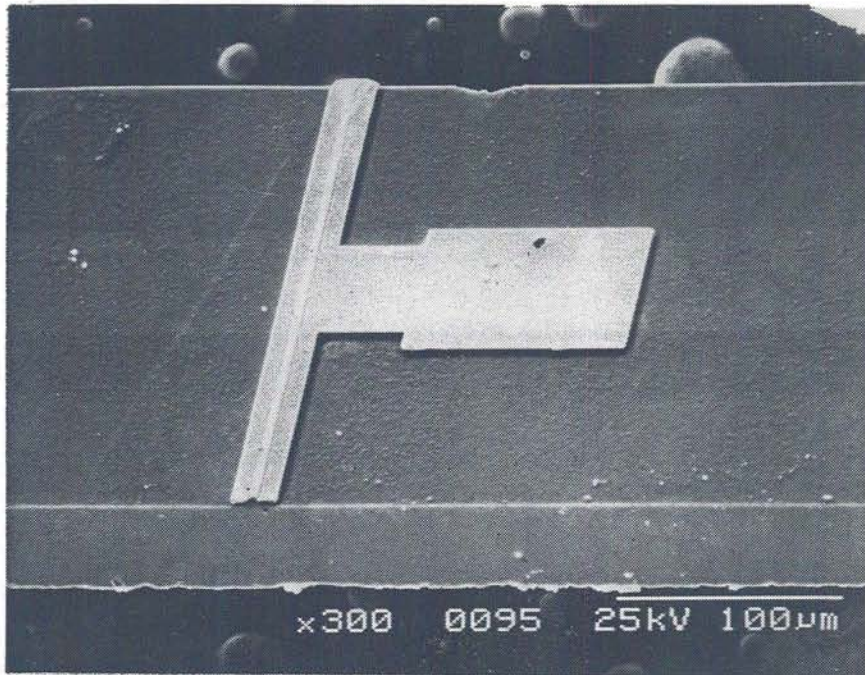
(a)
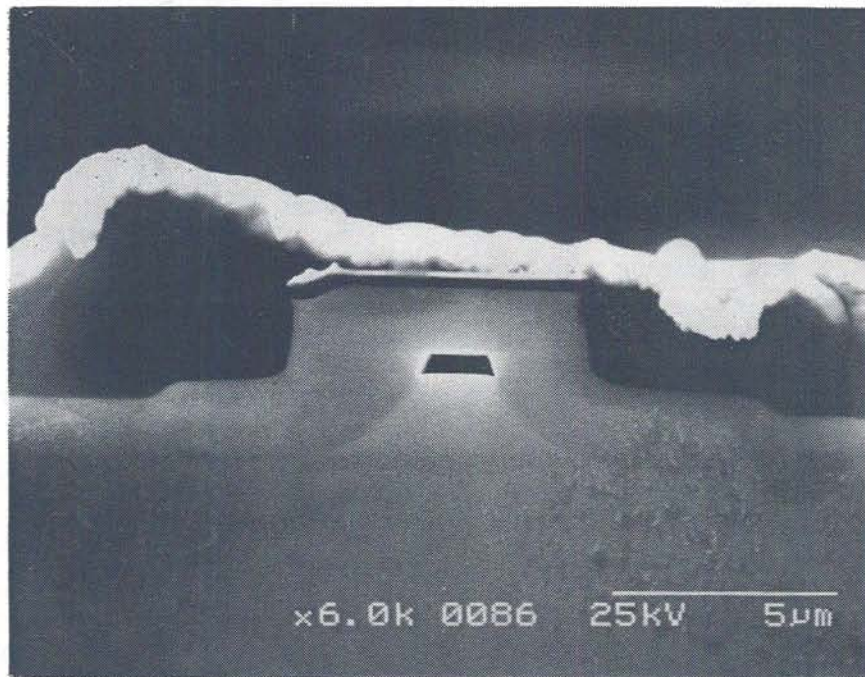
(b)

Figure 3.13   Completed CMBH devices.   (a)   Single device on a bar.   (b)   Close-up of the mesa.

The active area has been stained to show the detail.

94

temperature paraffin wax. This wax melts at about 80 °C and can be dissolved in trichloroethane (TCE). The low melting temperature of this wax allows the Si to be mounted and dismounted without disturbing the wafer. The different solvents allow the Si and wafer to be cleaned separately. Finally, the brass block is secured to a piston and collar assembly and is ready for lapping. The wafer is thinned to a thickness of 75 to 80 μm using a slurry of 5.0 μm alumina grit and water. The Si holder is removed, cleaned and loaded directly into the thermal evaporation chamber for n-contact deposition.

The n-contact consists of thermally evaporated Au 150 nm, Ni 50 nm and Au 50 nm. The rough surface allows for excellent Au adhesion to the substrate so that a "sticking" layer is not necessary. The Ni layer is used as a solder barrier to prevent the Au from being completely removed by the Pb/Sn solder used in the mounting process. The n-contact metal is ohmic as-deposited and the wafer is not annealed following evaporation.

The wafer is then cleaved into bars. A SEM photograph of a completed device is shown in Figure 3.13. Preliminary testing is done in this state to determine which devices are suitable for mounting.

3.8 Mounting and Testing

Two types of mounting are used depending on the intended use of the laser, copper studs and modified K-connectors. The first type of mount is shown in Figure 3.14 (a). A short segment of microstrip transmission line is soldered to one end of the copper stud. The laser diode is soldered adjacent to the microstrip. The laser and microstrip are connected by a length of 125 μm wide Au ribbon. Ribbon is used instead of bondwire to reduce the parasitic inductance. The advantages of this

95
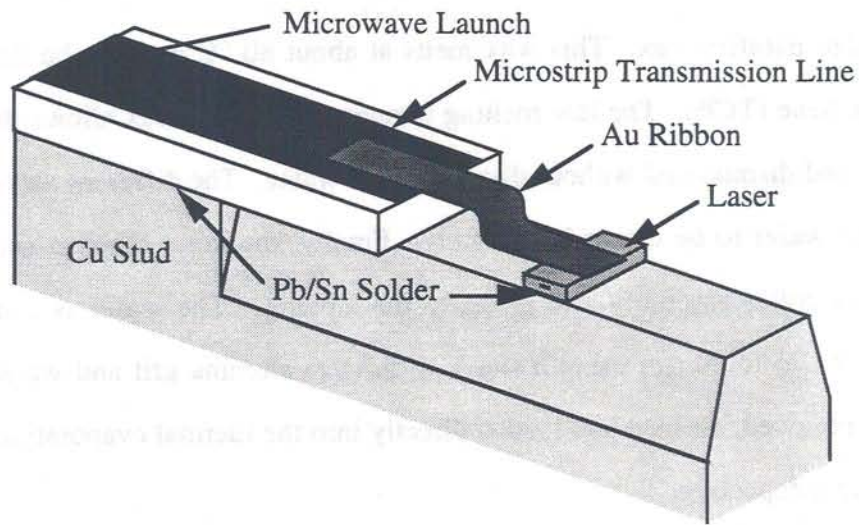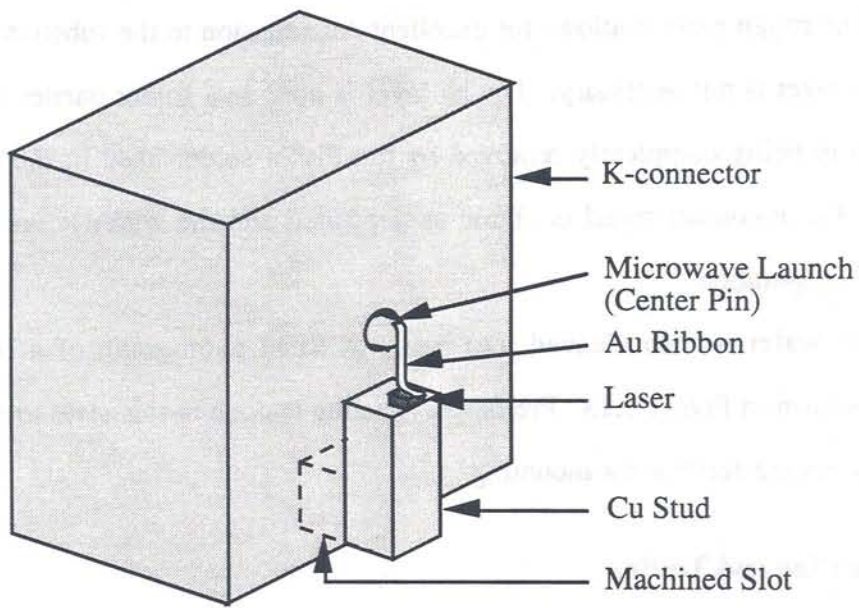
Figure 3.14   Microwave mounting schemes for semiconductor laser diodes. (a) Copper stud mount.

(b) K-connector mount.

mounting scheme are that it is inexpensive and that light is available from both facets.

The second type of mount is shown in Figure 3.14 (b) A slot has been machined into

a standard K-connector. After the laser has been soldered to a matching copper stud,
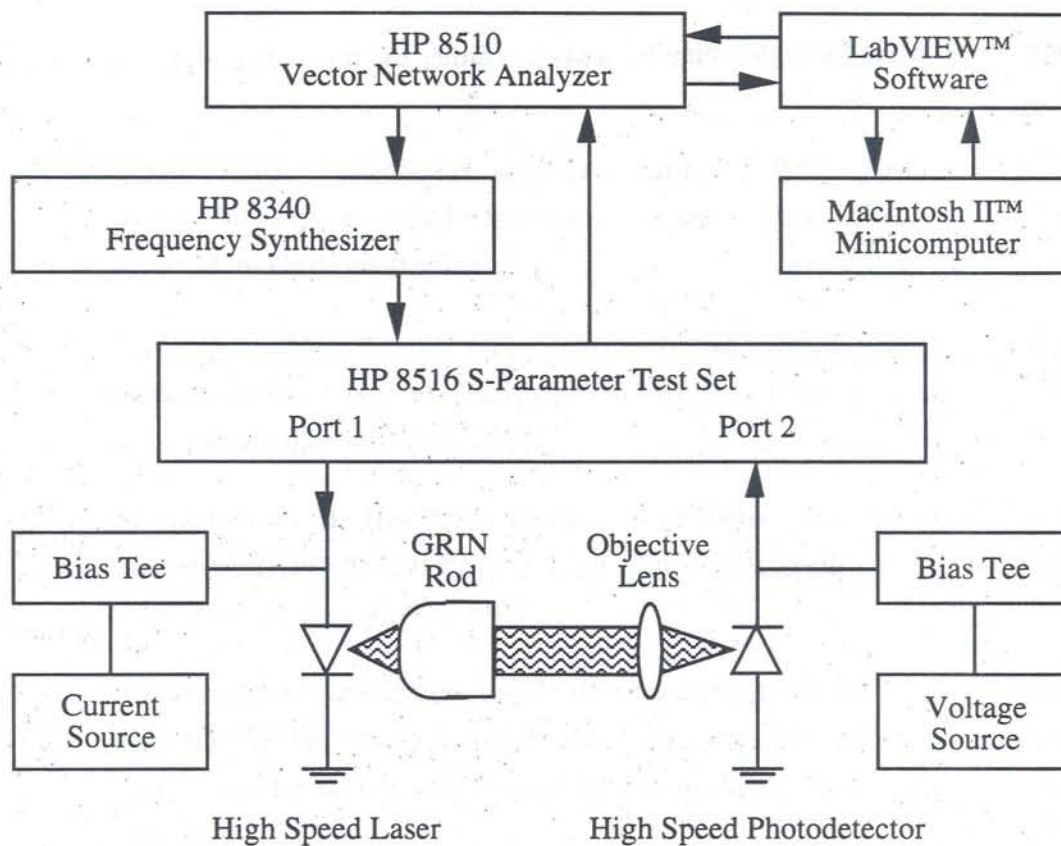
Figure 3.15   Microwave test setup for frequency modulation measurements.

the stud is inserted into the K-connector and secured with conducting epoxy. Once
again Au ribbon is used to bond the center pin of the K-connector to the bond pad of
the laser diode. The advantage of this mounting scheme are that microwave
reflections are largely eliminated and the connector fits standard sockets. The
disadvantage is that light is available from only one facet.

The experimental setup for measuring modulation bandwidth and S-
parameters is shown in Figure 3.15. It consists of an S-parameter test set driven by a
frequency generator, which is in turn controlled by a network analyzer. Frequencies
over the bandwidth of interest are step generated and launched over 26 GHz K-

connector cables, through a bias tee and onto either the microstrip or K-connector of the laser mount.
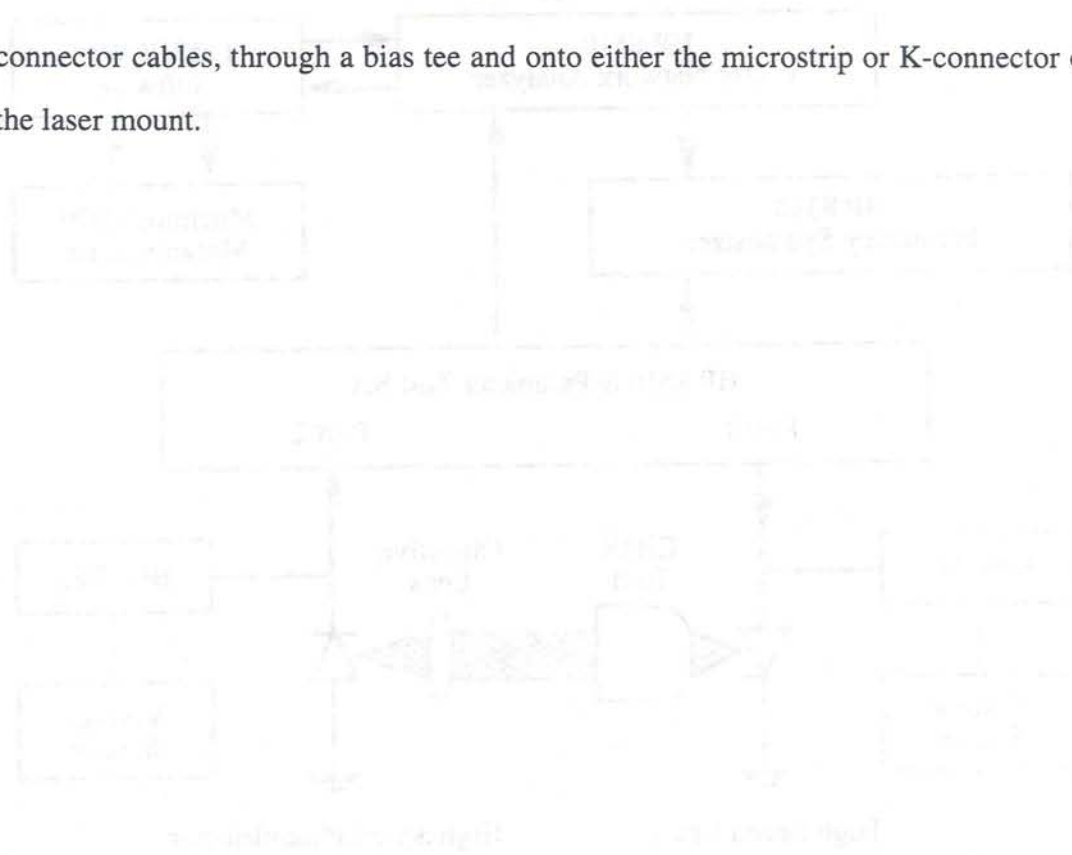
References

1. P. Speier, G. Schemmel, and W. Kuebart, "MOVPE Growth and Characteristics of Fe-Doped Semi-Insulating InP Layers," *Electron. Lett.*, vol. 22, pp. 1216-1218, 1986.

2. S. Iyer, A. T. Macrander, R. F. Karlicek, Jr., and S. Lau, "Semi-Insulating Properties of Fe-Doped InP Grown by Hydride Vapor Phase Epitaxy," *J. Appl. Phys.*, vol. 66, pp. 5580-5584, 1989.

3. S. Lourdudoss, B. Hammarlund, and O. Kjebon, "An Investigation On Hydride VPE Growth and Properties of Semi-Insulating InP-Fe," *J. Electron. Mater.*, vol. 19, pp. 981-987, 1990.

4. R. T. Huang, A. Appelbaum, and D. Renner, "High Quality Fe-Doped Semi-Insulating InP Epitaxial Layers Grown by Low-Pressure Organometallic Vapor Phase Epitaxy Using Tertiarybutylphosphine," *Appl. Phys. Lett.*, vol. 58, pp. 170-172, 1991.

5. K. W. Wang, V. D. Mattera, F. Ren, D. Zolnowski, J. N. Hollenhorst, and D. N. Buckley, "Growth and Properties of Semi-Insulating InP Using Multi-Frit Trichloride Vapor Phase Epitaxy (MOVPE)," *J. Electrochem. Soc.*, vol. 138, pp. L41-L43, 1991.

6. R. T. Huang, A. Appelbaum, D. Renner, W. Burke, and S. W. Zehr, "Growth and Characterization of Fe-doped Semi-Insulating InP Prepared by Low-Pressure Organometallic Vapor Phase Epitaxy With Tertiarybutylphosphine," *J. Appl. Phys.*, vol. 69, pp. 8139-8144, 1991.

7. J. E. Bowers, U. Koren, B. I. Miller, C. Soccolich, and W. Y. Jan, "High-Speed, Polyimide-Based Semi-Insulating Planar Buried Heterostructures," *Electron. Lett.*, vol. 23, pp. 1263-1265, 1987.

8.   W. H. Cheng, D. Renner, K. L. Hess, and S. W. Zehr, "Dynamic Characteristics of Semi-Insulating Current Blocking Layers: Application to Modulation Performance of 1.3 μm InGaAsP Lasers," *J. Appl. Phys.*, vol. 64, pp. 1570-1573, 1988.

9 .   G. W. Iseler, "Properties of InP Doped With Fe, Cr, or Co," *Inst. Phys. Conf.*, Ser. No. 45, pp. 144-153, 1979.

10.   B. Cockayne, W. R. MacEwan, and G. T. Brown, "The Single Crystal Growth and Electrical Properties of Cobalt-Doped Indium Phosphide," *J. Cryst. Growth*, vol. 55, pp. 263-267, 1981.

11.   E. A. Rezek, L. M. Zinkiewicz, and H. D. Law, "High-Resistivity ($>10^5$ Ω-cm) InP Layers by Liquid Phase Epitaxy," *Appl. Phys. Lett.*, vol. 43, pp. 378-380, 1983.

12.   W. H. Cheng, J. Pooladdej, S. Y. Huang, K. D. Buehring, A. Appelbaum, D. Wolf, D. Renner, K. L. Hess, and S. W. Zehr, "1.3 μm InGaAsP Buried Crescent Lasers With Cobalt-Doped Semi-Insulating Current Blocking Layers Grown by Metallorganic Chemical Vapor Deposition," *Appl. Phys. Lett.*, vol. 53, pp. 1257-1259, 1988.

13.   C. D. Brandt, "A Study of Energy Levels Introduced by Transition Elements in III-V Compound Semiconductors," Ph. D. Thesis, Massachusetts Institute of Technology, 1987.

14.   C. D. Brandt, A. M. Hennel, L. M. Pawlowicz, Y. T. Wu, T. Boyskiewicz, J. Lagowski, and H. C. Gatos, "New Semi-Insulating InP: Titanium Midgap Donors," *Appl. Phys. Lett.*, vol. 48, pp. 1162-1164, 1986.

15.   C. E. Zah, C. Caneau, S. G. Menocal, F. Favire, T. P. Lee, A. G. Dental, and C. H. Joyner, "High-Speed 1.3 μm GaInAsP *p*-Substrate Buried-Crescent

Lasers With Semi-Insulating Fe/Ti-Doped Current Blocking Layers," *Electron. Lett.*, vol. 24, pp. 695-697, May 1988.

16. M. A. Lampert and P. Mark, Current Injection in Solids, New York Academic, 1970, Chapters 1 and 4.

17. K. L. Ashley and A. G. Milnes, "Double Injection in Deep-Lying Impurity Semiconductors," *J. Appl. Phys.*, vol. 35, pp. 369-374, 1964.

18. M. Sugawara, O. Aoki, N. Nakai, K. Tanaka, A. Yamaguchi, and K. Nakajima, Semi-Insulating III-V Materials, Ohmsha, Tokyo and North-Holland, Amsterdam, 1986, pp. 597-602.

19. M. A. Lampert, "Double Injection in Insulators," *Phys. Rev.*, vol. 125, pp. 126-141, 1962.

20. J. Cheng, S. R. Forrest, B. Tell, D. Wilt, B. Schwartz, and P. Wright, "Semi-Insulating Properties of Fe-Implanted InP. II. Deep Levels of Fe from the Study of p^+-Semi-Insulating-n^+ Diodes," *J. Appl. Phys.*, vol. 58, pp. 1787-1797, 1985.

21. S. Asada, S. Sugou, K. I. Kasahara, and S. Kumashiro, "Analysis of Leakage Current In Buried Heterostructure Lasers with Semi-Insulating Blocking Layers," *IEEE J. Quantum Electron.*, vol. 25, pp. 1362-1368, 1989.

22. E. W. A. Young and G. M. Fontijn, "Zinc-Stimulated Outdiffusion of Iron in InP," *Appl. Phys. Lett.*, vol. 56, pp. 146-147, 1990.

23. W. H. Cheng, H. Kuwamoto, A. Applebaum, D. Renner, and S. W. Zehr, "Effect of Zinc Diffusion from Overgrown *p*-InP Layers on Semi-Insulating InP," *J. Appl. Phys.*, vol. 69, pp. 1862-1865, 1991.

24.   K. W. Wang, S. M. Parker, C. L. Cheng, and J. H. Long, "Diffusion in InP Using Evaporated Zn_3P_2 Film with Transient Annealing," *J. Appl. Phys.*, vol. 63, pp. 2104-2109, 1988.

25.   A. W. Nelson and L. C. Westbrook, "A Study of Zinc Doping in Metallo-Organic Chemical Vapor Deposition of InP," *J. Appl. Phys.*, vol. 55, pp. 3103-3108, 1984.

26.   Y. Abe, T. Ohishi, H. Sugimoto, K. Ohtsuka, T. Matsui, H. Ogata, "High-Speed 1.55 μm GaInAsP/InP Mass Transport Laser Diode On Semi-Insulating Substrate," *Electron. Lett.*, vol. 25, pp. 1505-1506, 1989.

27.   J. E. Bowers, B. R. Hemenway, A. H. Gnauck, and D. P. Wilt, "High Speed InGaAsP Constricted Mesa Lasers," *J. Quantum Electron.*, vol. QE-22, pp. 833-834, 1986.

28.   H. Wada, H. Horikawa, Y. Matsui, Y. Ogawa, and Y. Kawai, "1.55 μm DFB Lasers with Fe-Doped InP Current Blocking Layers Grown by Two-Step MOVPE," *Electron. Lett.*, vol. 25, pp. 133-134, 1989.

29.   H. Wada, H. Horikawa, Y. Matsui, Y. Ogawa, and Y. Kawai, "High-Power and High-Speed 1.3 μm V-Grooved Inner-Stripe Lasers with New Semi-Insulating Current Confinement Structures on *p*-InP Substrates," *Appl. Phys. Lett.*, vol. 55, pp. 723-725, 1989.

30.   W. H. Cheng, S. B. Su, K. D. Buehring, J. W. Ure, D. Perrachione, D. Renner, K. L. Hess, and S. W. Zehr, "High-Speed and High-Power 1.3 μm InGaAsP Buried Crescent Injection Lasers with Semi-Insulating Current Blocking Layers," *Appl. Phys. Lett.*, vol. 51, pp. 1783-1785, 1987.

31.   W. Thulke and S. Illek, "1.53 μm DFB Laser on Semi-Insulating InP Substrate with Very Low Threshold Current," *Electron. Lett.*, vol. 26, pp. 933-934, 1990.

32.   T. Tanbun-Ek, R. A. Logan, and J. P. Van Der Ziel, "High Frequency Buried Heterostructure 1.5 μm GaInAsP/InP Lasers, Grown Entirely by Metalorganic Vapour Phase Epitaxy in Two Epitaxial Growth Steps," *Electron. Lett.*, vol. 24, pp. 1483-1484, 1988.

33.   C. Kazmierski, A. Ougazzaden, D. Robein, D. Mathoorasing, M. Blez, and A. Mircea, "20 GHz Bandwidth 1.5 μm Wavelength VUG DFB Laser Using a Zero Net Strain $In_xGa_{1-x}As_yP_{1-y}$ Well Active Structure Grown at Constant y," *Electron. Lett.*, vol. 29, pp. 1290-1291, 1993.

34.   P. A. Morton, R. A. Logan, T. Tanbun-Ek, P. F. Sciortino Jr., A. M. Sergent, R. K. Montgomery, and B. T. Lee, "25 GHz Bandwidth 1.55 μm GaInAsP *p*-Doped Strained Multiquantum-Well Lasers," *Electron. Lett.*, vol. 28, pp. 2156-2157, 1992.

35.   T. Kambayash, C. Kitahara, and K. Iga, "Chemical Etching of InP and GaInAsP for Fabricating Laser Diodes and Integrated Optical Circuits," *Jap. J. Appl. Phys.*, vol. 19, pp. 79-85, 1980.

36.   J. E. Bowers, T. L. Koch, B. R. Hemenway, D. P. Wilt, T. J. Bridges, and E. G. Burkhardt, "High-Frequency Modulation of 1.52 μm Vapour-Phase-Transported InGaAsP Lasers," *Electron. Lett.*, vol. 21, pp. 392-393, 1985.

37.   B. I Miller, U. Koren, and R. J. Capik, "Planar Buried Heterostructure InP/GaInAs Lasers Grown Entirely by OMVPE," *Electron. Lett.*, vol. 22, pp. 947-949, 1986.

38.   T. Sanada, K Nakaei, K. Wakao, and S. Yamakoshi, "Planar-Embedded InGaAsP/InP Heterostructure Laser with a Semi-Insulating InP Current-Blocking Layer Grown by Metallorganic Chemical Vapor Deposition," *Appl. Phys. Lett.*, vol. 51, pp. 1054-1056, 1987.

103

39. T. Tanbun-Ek, R. A. Logan, and J. P. van der Ziel, "High Frequency Buried Heterostructure 1.5 μm GaInAsP/InP Lasers, Grown Entirely by Metallorganic Vapour Phase Epitaxy in Two Epitaxial Growth Steps," *Electron. Lett.*, vol. 24, pp. 1483-1484, 1988.

40. R. T. Huang, C. L. Jiang, A. Appelbaum, and D. Renner, "Selective Growth of InP in Patterned, Nonplanar InP Substrates by Low-Pressure Organometallic Vapor Phase Epitaxy," *J. Electron. Mater.*, vol. 19, pp. 1313-1317, 1990.

41. G. Laube, A. Nowitzki, K. Dütting, and P. Speier, "Selective MOVPE of Semi-Insulating InP Layers for High Speed OEICs," *J. Cryst. Growth*, vol. 107, pp. 156-160, 1991.

42. A. R. Clawson, C. M. Hanson, and T. T. Vu, "MOVPE Growth of SiO$_2$-Masked InP Structures at Reduced Pressures," *J. Cryst. Growth,* vol. 77, pp. 334-339 1986.

43. M. Oishi and K. Kuroiwa, "Low Pressure Metalorganic Vapor Phase Epitaxy of InP in a Vertical Reactor," *J. Electrochem. Soc.,* vol. 132, pp. 1209-1214, 1985.

44. K. Nakai, T. Sanada, and S. Yamakoshi, "Planar Selective Growth of InP by MOVPE," *J. Cryst. Growth,* vol. 93, pp. 248-253, 1988.

45. R. F. Karlicek, Jr., B. P. Segner, J. D. Wynn, A. J. Becker, U. K. Chakrabarti, and R. A. Logan, "Regrowth of Semi-Insulating InP around Etched Mesas Using Hydride Vapor Phase Epitaxy," *J. Electrochem. Soc.,* vol. 137, pp. 2639-2642, 1990.

46. S. Lourdudoss, B. Hammarlund, and O. Kjebon, "An Investigation on Hydride VPE Growth and Properties of Semi-insulating InP:Fe," *J. Electron. Mater.,* vol. 19, pp. 981-987, 1992.

47.   O. Kjebon, S. Lourdudoss, J. Wallin, U. Westergren, and S. Lindgren, "Extemely Low Parasitic 1.55 µm Lasers for Direct Amplitude High Frequency Modulation up to 20 GHz," submitted to ECOC '93.

48.   R. Nagarajan, "Carrier Transport Effects in High Speed Quantum Well Lasers," Ph. D. Thesis, University of California, Santa Barbara, 1992.

Chapter 4
Contact and Heterojunction Resistance

4.1 High Performance Ohmic Contacts

The importance of high-quality, ohmic contacts to InP and related materials has spurred widespread and intense investigation during the last decade. With the improvement of high-performance electronic and photonic devices have come ever more stringent requirements on the nature of the ohmic contacts. Devices which are operated at high speed, under high current density and at elevated-temperatures require contacts that (a) have the lowest possible resistance, (b) provide stable morphology over a wide temperature range, which requires the presence of only limited intermetallic reactions, and thus requires an abrupt metal-semiconductor interface throughout the contact processing, (c) cause no excessive stresses in the metal films or underlying dielectric or semiconductor layers, and (d) are compatible with the overall device processing scheme. However, due to the large energy bandgap of InP (E_g = 1.3 eV), the metal-semiconductor interface for most metals has a large barrier for holes (Φ_{Bp} = 0.82 eV). As a result, it is typically difficult, at best, to make good, ohmic contact to *p*-type InP. For this reason it is common practice to use a smaller bandgap material, such as InGaAsP (E_g = 1.09 eV) or InGaAs (E_g = 0.75 eV), as a contact layer. Both of these materials have been used in this investigation.

As a practical matter, ohmic contacts are generally considered to be metal-semiconductor Schottky barriers in which a high concentration of dopants in the

106

interface region cause a narrowing and lowering of the barrier allowing a majority of carriers to pass through. The most conventional ways of introducing dopants in the interface region are by (1) incorporating a high dopant concentration into the initial epitaxial growth, (2) by introducing an external dopant source from which the dopants are driven into the semiconductor by a heat treatment process, and (3) by ion implantation. The first two metallization schemes discussed in this work, AuBe and Pd/Zn, utilize a combination of the first two methods. A different approach to forming an ohmic contact is to employ a semiconductor with an extremely narrow bandgap, such as InAs (~0.35 eV), thereby reducing the height of the metal-semiconductor Schottky barrier significantly [1]. This is the thrust of the third metallization scheme, Ti/Pt.

Throughout this chapter we will refer extensively to the transmission line model (TLM) for ohmic contacts. The model treats planar contacts of the variety most often found in electronic and optoelectronic devices, and also provides a technique for measuring the specific contact resistance, r_c. Due to its importance both here and in referenced work, a brief summary of this model is given in the Appendix.

4.2   AuBe (0.9% Be) Contacts

Several Au-based alloys have been suggested for the formation of ohmic contacts to InP and its related compounds. Because of the highly reactive nature of the Au-In and Au-P binary systems, Au readily alloys with InP at temperatures between 300 °C and 450 °C to form a thin, intermediate, heavily doped layer between the metal and the semiconductor. In addition, the large solid solubility of Au for the dopants makes it an ideal candidate for introducing and dispersing dopants without

the formation of dopant nucleation sites. The principal alloys used for contacts to p-type InP are AuZn [2, 3, 4, 5], and AuBe [6, 7, 8, 9]. These typically yield specific contact resistances on the order of 1×10^{-5} Ω-cm^2. Here we are principally interested in the use of AuBe (0.9% Be) as a metallization for devices with short wavelength, wide bandgap, quaternary contact layers, such as the etched mesa buried heterostructure (EMBH) described in Chapter 3. For the EMBH lasers described here, the wavelength of the quaternary contact layer was 1.14 μm.

One drawback of Au-based metallization schemes is that they tend to form wide interfacial reaction layers, which can grow to 2 to 3 times the thickness of the initial deposited metal layer [10]. In addition, annealing can cause the formation of Au spikes leading to non-uniform current injection across the contact [7, 10]. One method for improving the uniformity and planarity of Au-based contacts is to insert a barrier layer between the Au alloy and Au contact layers. The barrier layer is typically composed of a transition or refractory metal, such as Ni, Pt or Pd. Another method is to use rapid thermal annealing (RTA) instead of furnace annealing [11]. Both of these methods are employed here.

To measure the specific contact resistance, a layer of InGaAsP ($\lambda = 1.14$ μm) 0.5 μm thick was grown on SI InP. The layer was nominally Zn doped at a level of 2×10^{19} cm^{-3}. A mesa 100 μm wide was selectively etched to form the transmission line and 100 μm square pads were evaporated. The metallization consisted of 50 nm of AuBe (0.9% Be), 50 nm of Ni as a blocking layer, and 200 nm of Au. The as-deposited contacts were non-ohmic. The samples were rapid thermal annealed for a variety of times and at a variety of temperatures. Figure 4.1 shows the dependence of r_c on anneal time. The r_c reached its final value very quickly, indicating that the

108
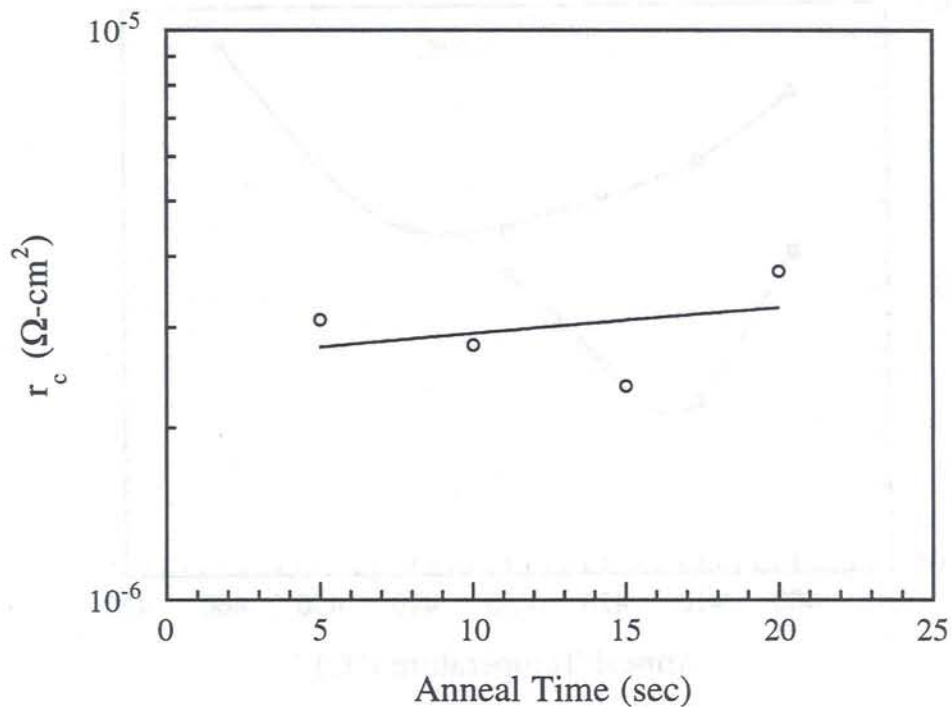
Figure 4.1   Dependence of average r_c on anneal time at 420 °C for AuBe metallization. Samples were rapid thermal annealed in a N_2 ambient.

alloying and Be diffusion take place in only a few seconds. Figure 4.2 shows the dependence of r_c on anneal temperature. The solid line represents an average of four measured values. A smooth minimum in r_c occurs between 420 and 450 °C. These results compare favorably with the published literature [7].

Since Be is a very reactive, it was suspected that specific contact resistance might be sensitive to surface preparation prior to evaporation and the amount of time the sample was exposed to the ambient before annealing. Figure 4.2 shows how the specific contact resistance varied with anneal temperature for two different surface preparations. The graph demonstrates a significant difference between surface preparations based on HCl and HF. However, other processing considerations, such
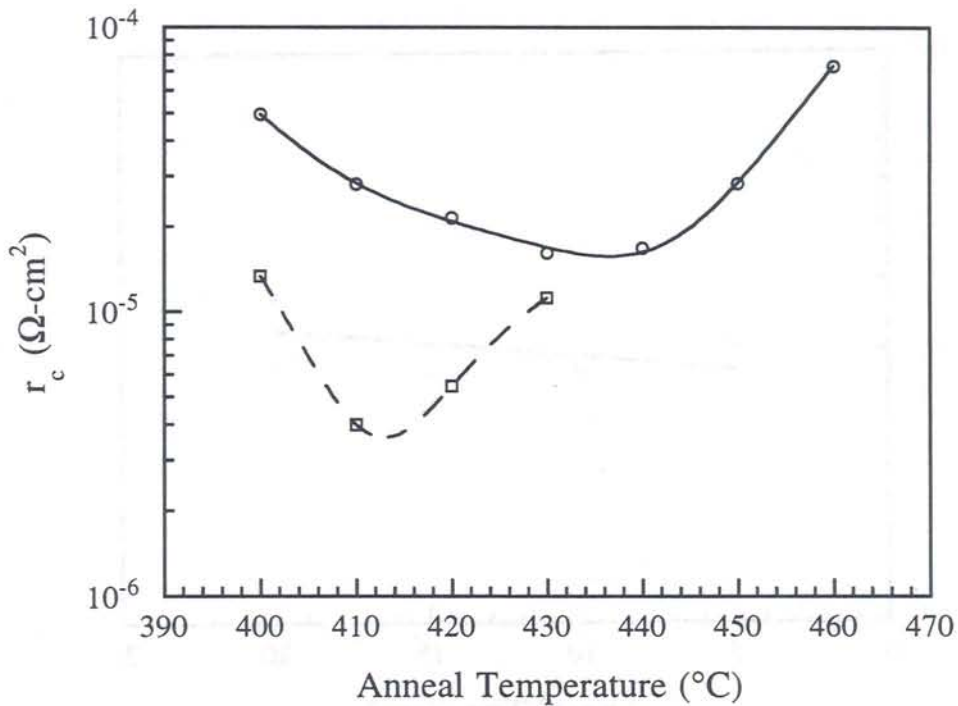
Figure 4.2   Variation of average r_c with anneal temperature for AuBe metallization. Solid line represents a surface preparation of HCl:3H$_2$O for 1 min. Dashed line represents a surface preparation of BHF:5H$_2$O for 10 sec. Samples were rapid thermal annealed for 5 seconds in a N$_2$ ambient.

as whether it is necessary to preserve a SiO$_2$ layer, may dictate which surface preparation is used. Figure 4.3 shows the measured r_c as a function of the time delay between removing the sample from the evaporation vacuum chamber and the anneal. There is very little degradation of the contact integrity, even for very long delay times.
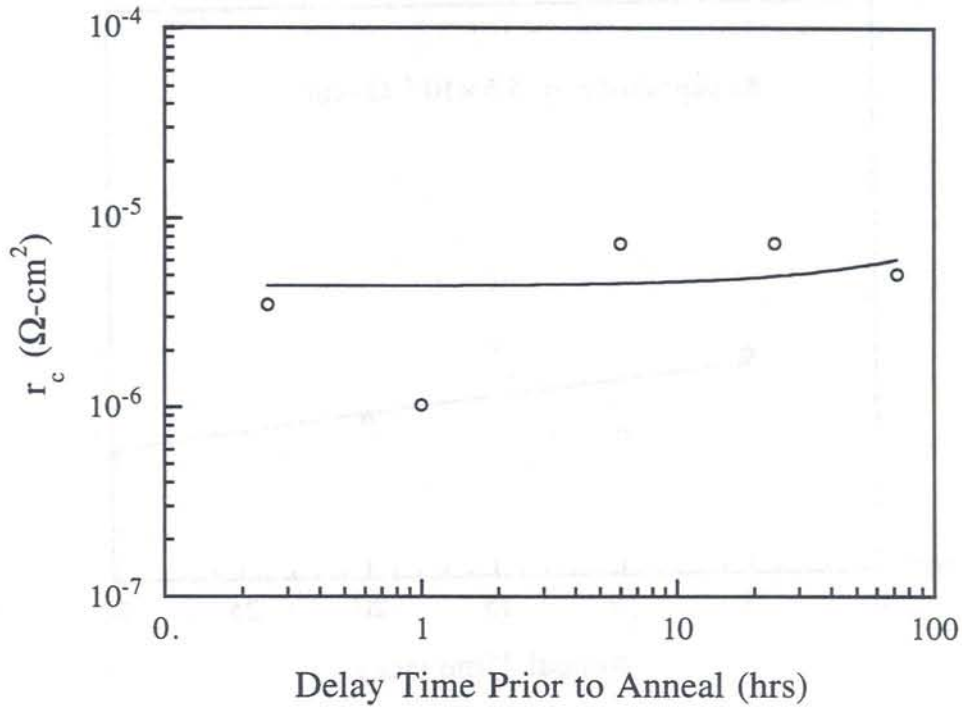
Figure 4.3   Variation of average r_c with delay time between removal from the metal deposition vacuum and rapid thermal anneal for AuBe (0.9% Be) on InGaAsP ($\lambda = 1.14\ \mu$m).

4.3   Pd/Zn Contacts

The Pd/Zn metallization scheme was suggested by a report of low-resistance, laterally uniform contacts to *p*-type GaAs [12]. Earlier investigations show that Pd easily penetrates the native oxide on GaAs and reacts with the substrate at temperatures below 500 °C to form binary and ternary compounds [13, 14]. It was postulated that the formation of these compounds should lead to the formation of Ga vacancies and thus promote the incorporation and diffusion of Zn in addition to improving adhesion and uniformity of contact formation. We suspected that a similar metallization might be applicable to InGaAs lattice matched to InP.

111
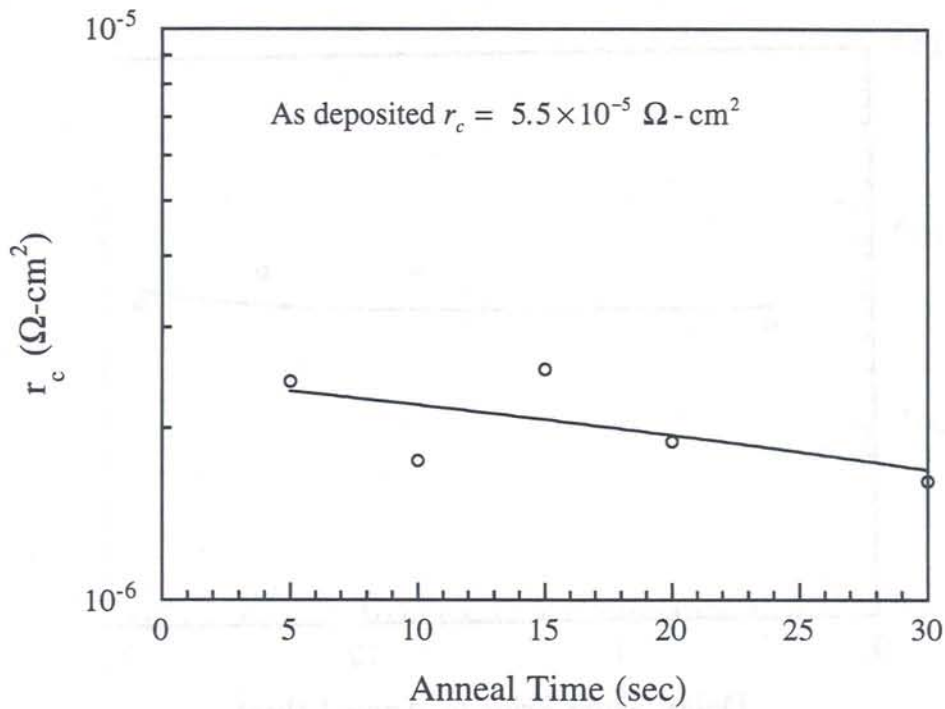
Figure 4.4   Dependence of r_c on anneal time at 420 °C for Pd/Zn metallization.

As in the case of AuBe, Pd/Zn provides a solid source for dopant diffusion at the semiconductor surface. Thus, it can be used when the contact layer doping is less than ideal ($<10^{19}$ cm^{-3}). Our particular version of this metallization consists of 10 nm Pd, 3-5 nm Zn, 30 - 50 nm Pd and 200 nm Au. All layers were thermally evaporated. The second Pd layer is used as a barrier layer, also similar to the AuBe case. Ni or other suitable transition or refractory metal may be substituted for Pd. The barrier layer is intended to promote Zn diffusion into the Pd and semiconductor and to reduce the assimilation of Zn into the overlying Au layer. The barrier layer also serves to prevent the Au from alloying with, or spiking into, the semiconductor.

112
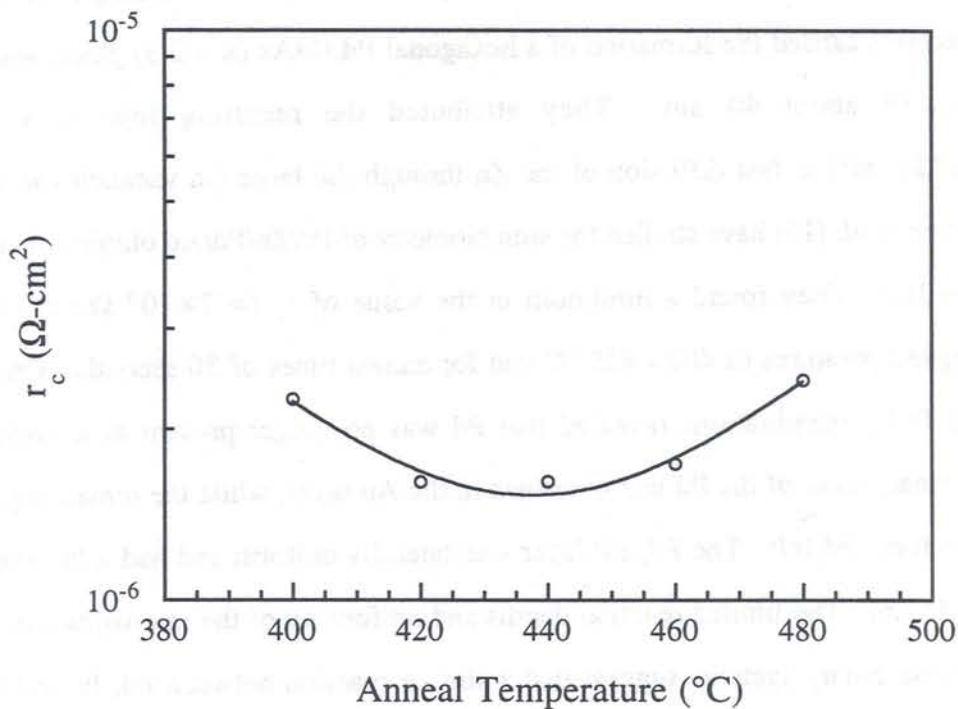
Figure 4.5   Variation of average r_c with anneal temperature for Pd/Zn metallization. All samples were annealed for 10 sec.

TLM samples were prepared as in the case of AuBe. All metals were deposited via thermal evaporation. The as-deposited contacts were ohmic with $r_c = 5.5 \times 10^{-5}$ Ω-cm^2. Annealing was performed in the rapid thermal annealer under N$_2$ ambient. Figure 4.4 shows the measured r_c as a function of anneal time. The alloying and diffusion process is once again very fast, and the r_c changes little with anneal times longer than about 10 seconds. Figure 4.5 shows the measured r_c as a function of anneal temperature. All anneal temperatures between 400 and 480 °C yielded r_c values in a very narrow range, between about 1.5 and 3.0×10^{-6} Ω-cm^2.

The reproducibility of this metallization was excellent, a likely indication of a uniform, planar microstructure. This is consistent with the studies done on both GaAs

113

and InP. In the case of GaAs, Bruce *et al.* [12] determined that annealing at 450 °C for 30 seconds caused the formation of a hexagonal Pd_xGaAs (x ≈ 2.5) phase with a thickness of about 40 nm. They attributed the resulting low r_c value ($\leq 1 \times 10^{-6}$ Ω-cm^2) to fast diffusion of the Zn through the large Ga vacancies in this phase. Ivey *et al.* [15] have studied the stoichiometry of Pd/Zn/Pd/Au ohmic contacts to *p*-type InP. They found a minimum in the value of r_c (= 7×10^{-5} Ω-cm^2) for annealing temperatures of 400 - 425 °C and for anneal times of 30 seconds. Cross-sectional TEM examinations revealed that Pd was no longer present as a distinct layer. Instead, most of the Pd had dissolved in the Au layer, while the remaining Pd reacted to form Pd_2InP. The Pd_2InP layer was laterally uniform and had a thickness of about 45 nm. The limited reaction depths and uniformity of the microstructure in both of these binary systems suggest that a similar reaction between Pd, In and Ga takes place during the anneal of Pd/Zn on InGaAs metallizations. To our knowledge, these are the first results reported for Pd/Zn on InGaAs lattice matched to InP.

4.4 Ti/Pt Contacts

Alternative methods of metal-semiconductor contact formation have been proposed which involve driving Au-free solid phase reactions and using higher eutectic melting point systems [16]. These contacts use the near-noble transition metals as the metallization scheme of choice. Due to the more stable thermodynamic properties and less reactive nature of these metals, they provide a less reactive and less degraded contact microstructure than Au-based alloys. This is typically achieved through heat treatments at higher temperatures. The ohmic nature of these contacts is obtained by both heavily doping the semiconductor layer under the metals and by the formation of narrow-bandgap intermetallic phases in the metal/semiconductor
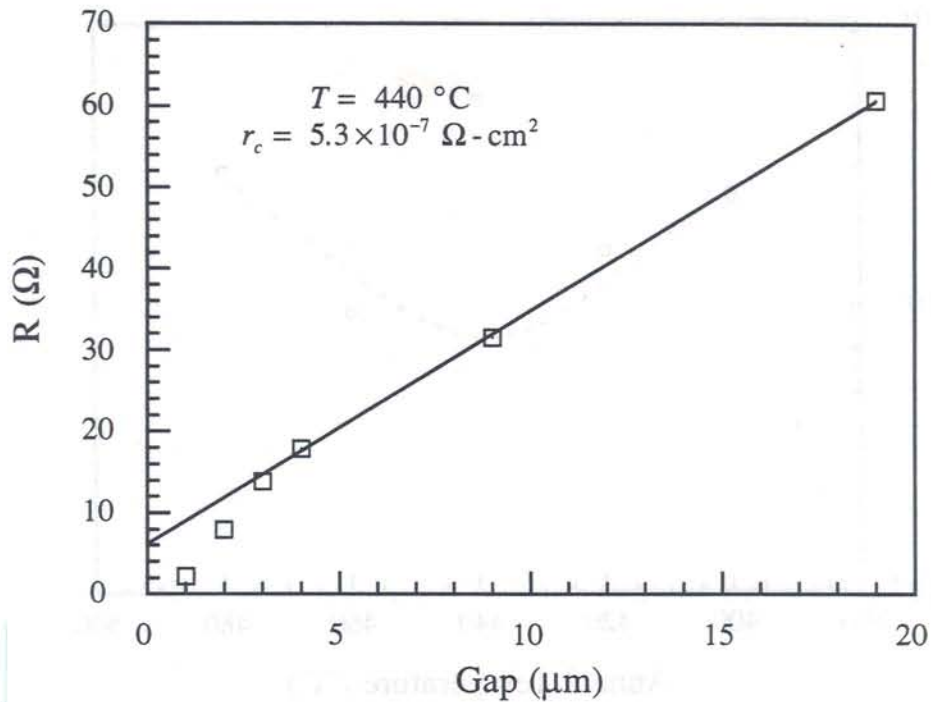
Figure 4.6   Example of TLM measurement for Ti/Pt/Au. Sample was annealed for 30 sec.

interface through a limited reaction when sintering. The most commonly used transition metal pair is Ti/Pt [17, 18, 19, 20, 21, 22, 23]. The metallization is composed of 30 nm Ti/30 nm Pt/200 nm Au. It contains no additional dopants for reducing the width of the Schottky barrier through band bending and thus relies heavily on the doping present in the epitaxial InGaAs contact layer for this purpose. The lowest contact resistances are obtained with a doping level in excess of 2×10^{19} cm^{-3}.

Ti/Pt/Au metallizations were found to give some of the best device resistances for the laser diodes fabricated in this study. However, a determination of the specific contact resistance of Ti/Pt/Au contacts was complicated by nonlinearities in the R vs. L measurements. A typical plot of R vs. L becomes sublinear for small gaps, as

115
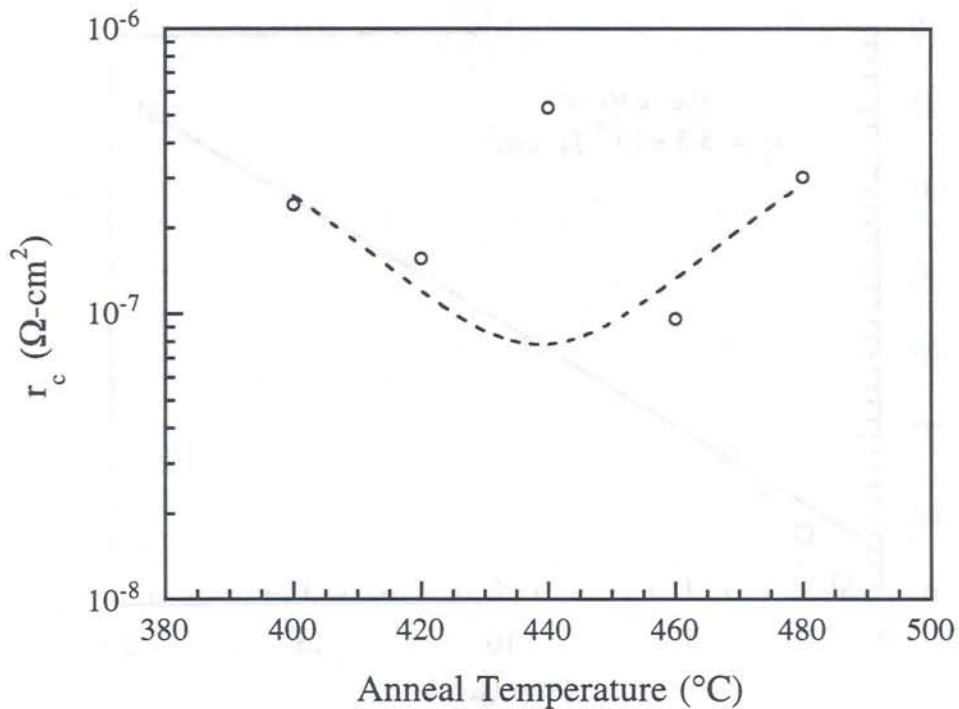
Figure 4.7   Variation of average r_c with anneal temperature for Ti/Pt/Au. Samples were annealed for 30 sec.

shown in Figure 4.6. Visual inspection of the TLM pattern revealed a Ti-like skirt approximately 0.5 μm wide surrounding each contact pad, causing the actual contact separation to be different from the defined separation. Subtracting 1 μm from all contact spacings, however, did not reconcile the data. It is possible that either the diffusion width is not equal for all separations, or that the conductivity of the material adjacent to the contact changes in a non-abrupt fashion with distance from the contact. In this situation it is best to use spacings ≥ 5 μm for the linear extrapolation, although this may reduce the overall accuracy of the measurement.

An electron beam evaporator was used to deposit 30 nm of Ti, 30 nm of Pt, and 200 nm Au. In this metallization scheme, Ti provides excellent adhesion between

116

the semiconductor and Pt layers. The wafers were sintered in a rapid thermal annealer for 30 seconds at various temperatures. The extracted specific contact resistance is plotted in Figure 4.7. It is evident that, while there is much scatter in the data due to the aforementioned measurement difficulties, all of the measured values fall between 1×10^{-6} and 1×10^{-7} Ω-cm^2. There is no discernible minimum between 400 °C and 500 °C. However, this data is in general agreement with that of Reference [23]. These are the best results of any metallization scheme we have measured.

The small specific contact resistance of this metallization scheme has been correlated with the contact microstructure [21]. A narrow interfacial reacted layer about 40 nm thick, containing InAs and various intermetallics, is observed just below the Ti/Pt layer. Below this InAs layer is a deformed zone of about 30 nm thick, which was formed in the InGaAs layer adjacent to the metal/semiconductor interface. The latter was formed as a result of the observable updiffusion of In and As, resulting in a significant depletion near the semiconductor surface, leading to a decrease in the lattice constant in the InGaAs layer, and inducing misfit stresses. The total reaction thickness of about 70 nm is much smaller than that of Au-based alloys. It is the presence of the highly doped, narrow bandgap (0.35 - 0.45 eV) InAs layer adjacent to the Ti/Pt that is responsible for the lowering of the Schottky barrier and resulting improvement in r_c.

In conclusion, three metallization schemes have been evaluated for possible use in the fabrication of high speed lasers. Table 4.1 summarizes the metallization schemes and their applications. For the device structures studied in this work, AuBe proved to be the best metallization for the 1.14 µm InGaAsP contact layer of the

117

EMBH. For narrower bandgap InGaAs layers, both Pd/Zn and Ti/Pt are appropriate. Attention must be paid, however, to the doping level of the contact layer. Since it contains no dopants, the Ti/Pt metallization is more sensitive to the doping level than Pd/Zn. Nevertheless, if the doping of the InGaAs layer is high ($>2\times10^{19}$ cm^{-3}), then Ti/Pt contacts are the preferred metallization.

Metallization	Anneal Temperature	Anneal Time	Comment
AuBe (0.9% Be)	400 - 420 °C	10 sec.	Useful for long-wavelength quaternaries. Surface preparation is important.
Pd/Zn	400 °C	10 sec.	Useful for InGaAs layers where additional doping is needed. Very reproducible.
Ti/Pt	420 °C	30 sec.	Best results for InGaAs layers where doping $\geq 2\times10^{19}$ cm^{-3}.

Table 4.1   Summary of metallizations and annealing conditions.

4.5. Heterojunction Resistance

In the previous section we discussed the contact resistance of the metal to semiconductor junction. We saw how important it was to use a narrow bandgap semiconductor, like InGaAs, to achieve a low value of r_c. These narrow bandgap semiconductors are typically grown on top of wider gap material, such as InP, with a much lighter doping concentration. This results in a large valence band offset at the heterojunction interface, presenting a large barrier to hole diffusion. This barrier manifests itself as an additional contact resistance, thus raising the total parasitic resistance of the device. In order to measure the specific resistance of the heterointerface, r_i, a structure must be used in which the dominant resistance is a result of this interface. We have investigated the effect of this barrier through the use of an interface transmission line model (ITLM) structure [24].

118
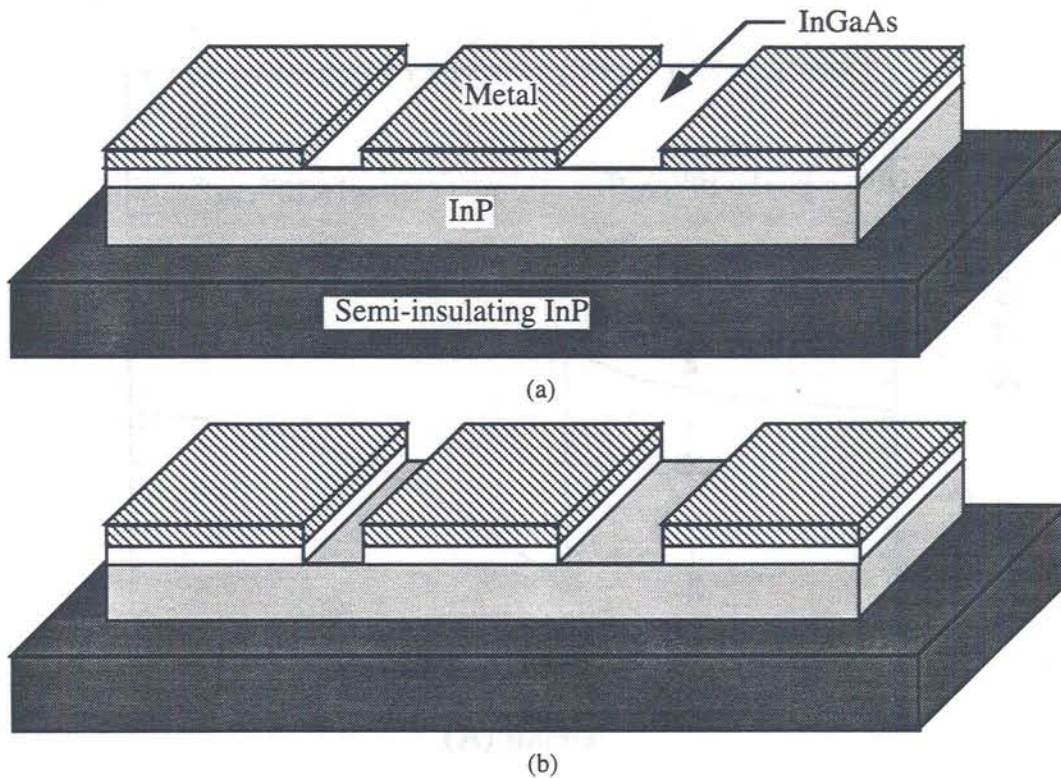
Figure 4.8   Schematic diagram of the ITLM device structure. (a) Etched mesa with evaporated contacts. (b) ITLM pattern after InGaAs layer etch.

Figure 4.8 illustrates the fabrication steps of the ITLM structure. Using selective etchants, a 100 μm wide mesa is patterned into the InGaAs and underlying InP for current confinement. 100 μm square pads are then patterned with gap spacings of 1, 2, 3, 4, 5, 10 and 20 μm. A contact metal consisting of 10 nm Pd, 5 nm Zn, 30 nm Pd and 200 nm Au is then evaporated and lifted off. As will be seen from the acceptably low values of contact resistance which are initially obtained, annealing of the contacts is not required. Finally, the contact layer between the metal pads is selectively removed by wet etching in $H_2SO_4:H_2O_2:10H_2O$ for 10 seconds. The resulting structure is shown in Figure 4.8 (b). TLM measurements were taken before and after the final etch.

119

(a)

InGaAs
$p = 1 \times 10^{17}\,\text{cm}^{-3}$

InP
$p = 1 \times 10^{18}\,\text{cm}^{-3}$

$q\Phi_B$

E_v (eV)

Depth (Å)

(b)

InGaAs
$p = 5 \times 10^{19}\,\text{cm}^{-3}$

InP
$p = 3 \times 10^{18}\,\text{cm}^{-3}$

-0.1 V

0 V

+0.1 V

$q\Phi_B$

E_v (eV)

Depth (Å)

120
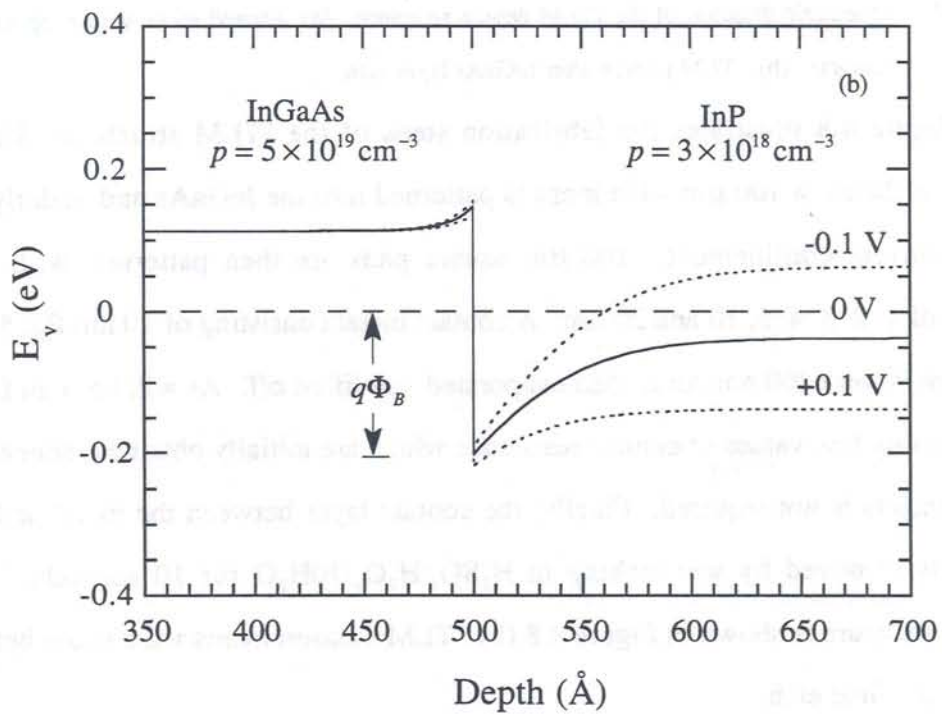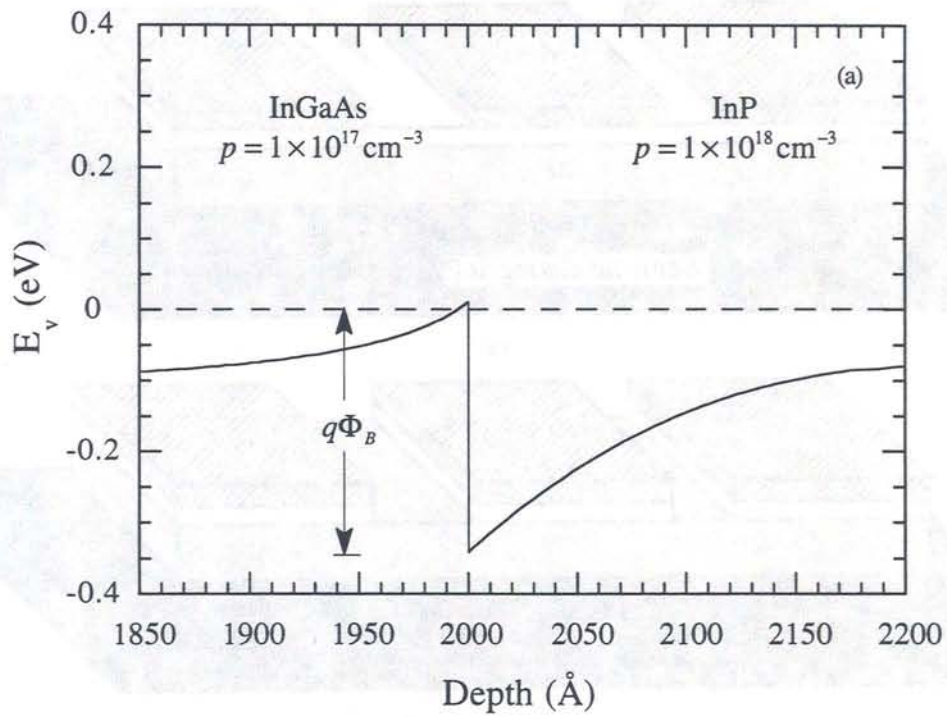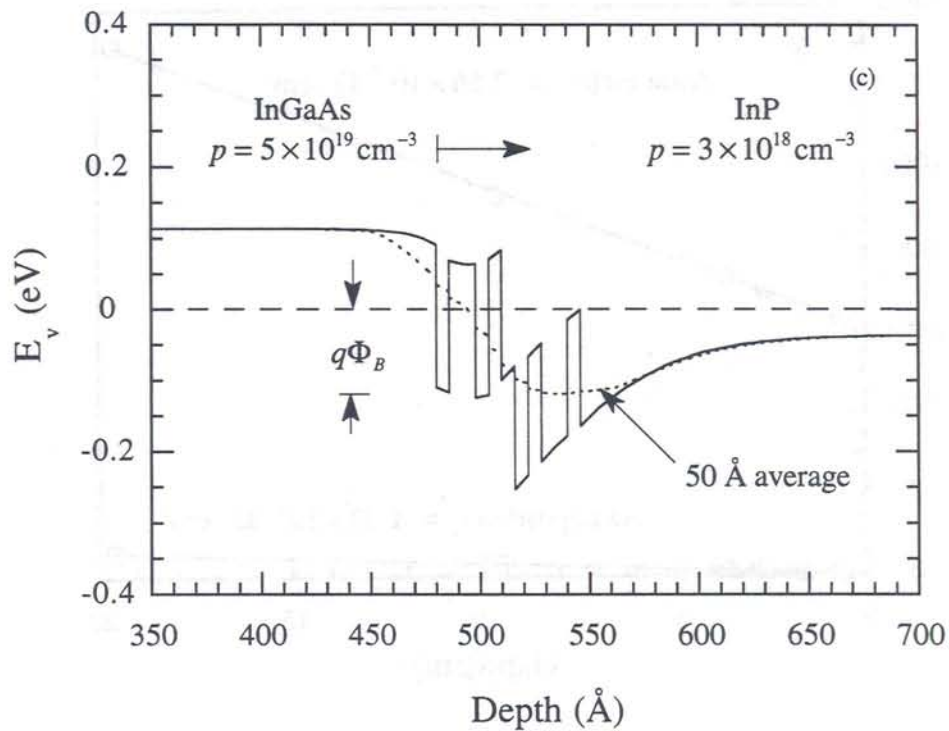
Figure 4.9   Calculated valence band structures. (a) Abrupt heterojunction of Sample A. (b) Abrupt heterojunction of Sample B. Dashed lines represent of bias levels of +0.1 and -0.1 V. Solid curve represents zero bias. (c) Digitally graded heterobarrier of Sample C. Dotted curve represents 50 Å averaging. The Fermi level (dashed line) is located at 0 eV in all plots.

The heterojunctions investigated in this work were grown by gas-source MBE [25].   Three types of interfaces were investigated: an abrupt heterojunction (Sample A) with a light doping on one side and a medium doping on the other, a heavily doped abrupt heterojunction (Sample B), and a heavily doped heterojunction with digitally graded bandgap layer (Sample C). A calculation of the valence band structures for Samples A, B and C are shown in Figure 4.9, where the area of interest has been enlarged to show the heterostructure detail.

121

Graph (a): R (Ω) vs Gap (μm)

(a)

After etch $r_c = 2.56 \times 10^{-7}$ Ω-cm^2

As deposited $r_c = 1.02 \times 10^{-7}$ Ω-cm^2

Graph (b): R (Ω) vs Gap (μm)

(b)

After etch $r_c = 1.87 \times 10^{-4}$ Ω-cm^2

As deposited $r_c = 5.04 \times 10^{-7}$ Ω-cm^2

122

$$\text{After etch } r_c = 7.40 \times 10^{-6} \ \Omega\text{-cm}^2$$

$$\text{As deposited } r_c = 3.52 \times 10^{-7} \ \Omega\text{-cm}^2$$
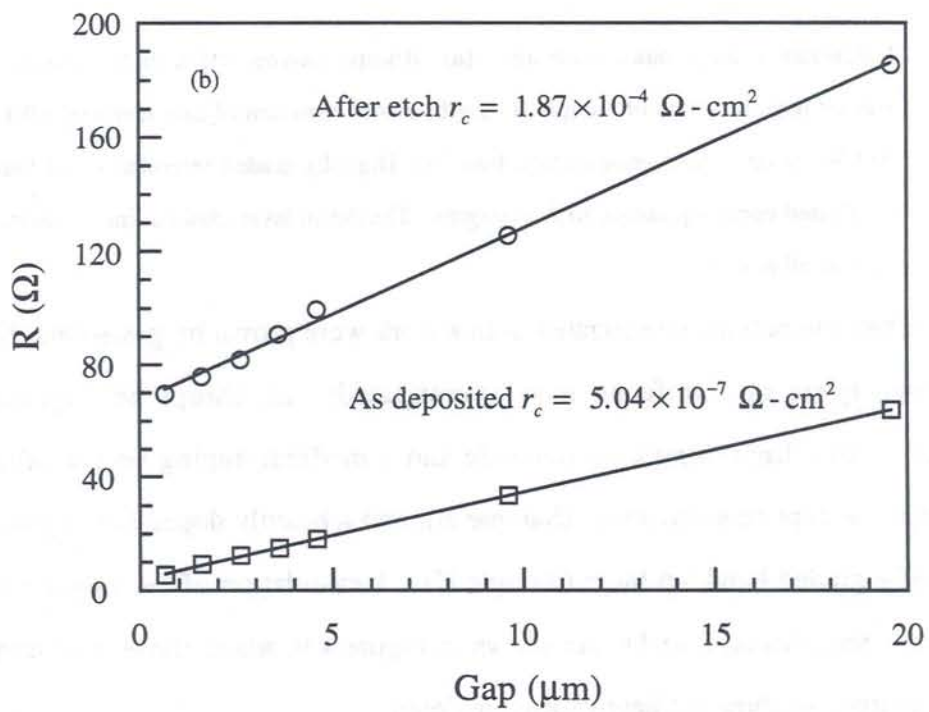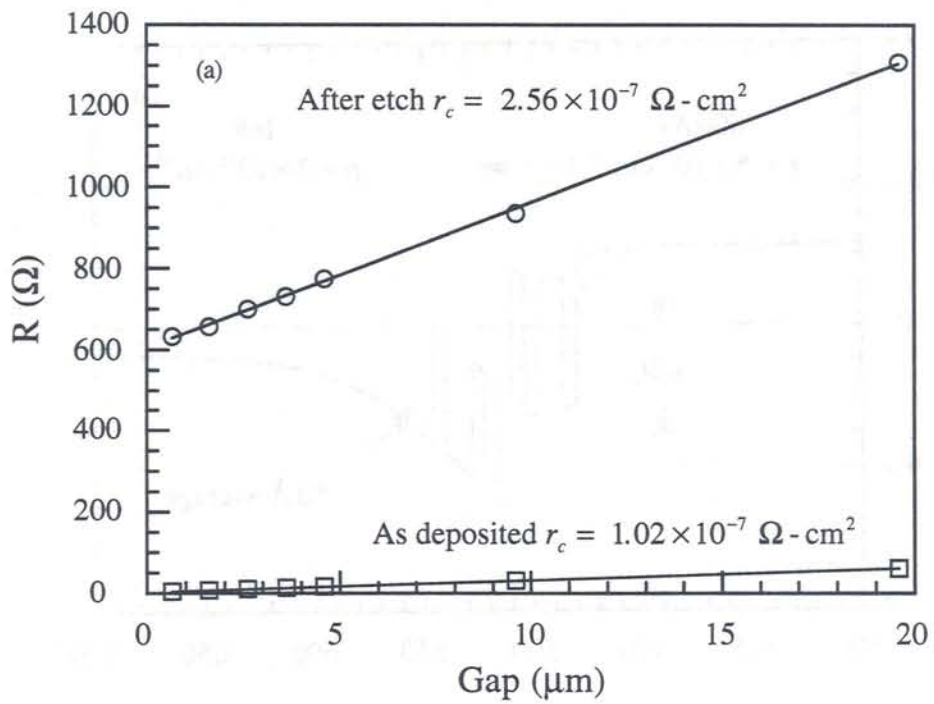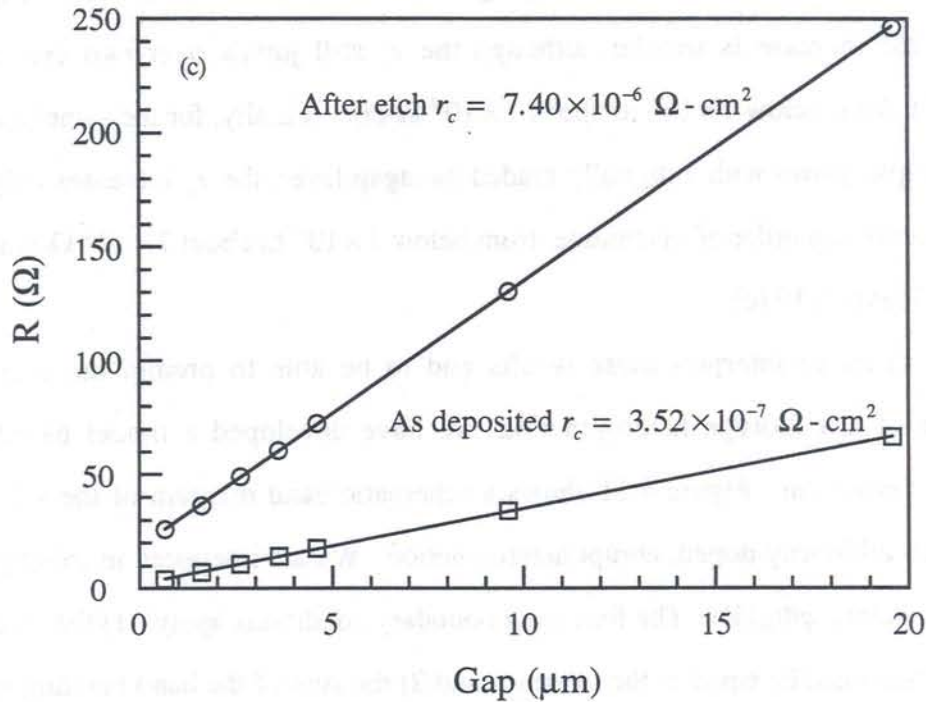
Figure 4.10   ITLM measurement results. (a) Sample A, a lightly doped, abrupt heterojunction. (b) Sample B, a heavily doped, abrupt heterojunction. (c) Sample C, a heavily doped, digitally graded heterobarrier.

Figure 4.10 shows the TLM results for all three of the cases studied. The accuracy of TLM measurements drops rapidly below the 10^{-6} Ω-cm^2 range due to large sensitivities to process and measurement errors. However, in all three cases, the as-deposited r_c was measured to be at or below 1×10^{-6} Ω-cm^2. Thus, we can assume that any r_c values greater than 10^{-6} Ω-cm^2 are due almost entirely to the heterointerface.

For the case of light to medium doping of the interface, Figure 4.10 (a), a dramatic increase in r_c is observed when the current is forced to go through the heterointerface. The r_c jumps three orders of magnitude, from 1×10^{-6} to

123

3×10^{-3} Ω-cm^2. For much heavier doping on both sides of the interface, Figure 4.10 (b), the increase is smaller, although the r_c still jumps over two orders of magnitude, from below 1×10^{-6} to above 1×10^{-4} Ω-cm^2. Finally, for the same heavily doped sample grown with a digitally graded bandgap layer, the r_c increases only by approximately one order of magnitude, from below 1×10^{-6} to about 7×10^{-6} Ω-cm^2, as shown in Figure 4.10 (c).

In order to interpret these results and to be able to predict the specific resistance of any isotype heterojunction, we have developed a model based on thermionic emission. Figure 4.11 shows a schematic band diagram of the valence band for an arbitrarily doped, abrupt heterojunction. We are interested in solving for the barrier height $q\Phi_B(V)$. The following boundary conditions apply: 1) the electric flux densities must be equal at the interface and 2) the sum of the band bending must equal the total built-in and applied voltages. These conditions may be written as

$$D_1 = D_2$$
$$\Psi_1 - \Psi_2 = \Delta,$$

where $kT\Delta = \Delta E_{v1 \rightarrow 2} - \left[(E_{v1} - E_{f1}) - (E_{v2} - E_{f2})\right] - qV_{bias}$ and $qV_{bias} = E_{f2} - E_{f1}$, which is simply the applied bias. Ψ is the band bending normalized to kT, and is defined as $\Psi(x) = (E_v(x) - E_v(\infty))/kT$. We will assume a convention in which Ψ is positive for depletion and negative for accumulation. Assuming non-degeneracy, the relationship between the electric field and the band bending may be written as

$$E = \left(\frac{2kTN_A}{\varepsilon}\right)^{1/2} \left[\Psi + e^{-\Psi} - 1\right]^{1/2},$$

where N_A is the acceptor concentration. At the interface, the first boundary condition may be written as
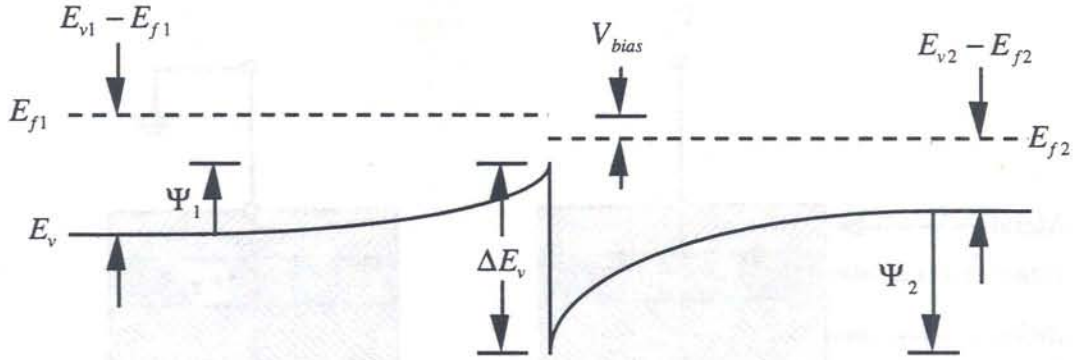
Figure 4.11   Schematic valence band diagram of the InGaAs/InP heterointerface.

$$\varepsilon_2 N_{A1}\left[\Psi_1 + e^{-\Psi_1} - 1\right] = \varepsilon_1 N_{A2}\left[\Psi_2 + e^{-\Psi_2} - 1\right].$$

Substituting for Ψ_2 and solving for Ψ_1 we find

$$e^{-\Psi_1} = \frac{(\alpha - 1)(\Psi_1 - 1) + \Delta}{e^\Delta - \alpha},$$

where we have introduced a relative doping factor, α, defined as

$$\alpha = \frac{\varepsilon_2 N_{A1}}{\varepsilon_1 N_{A2}}.$$

The equation for Ψ_1 must be solved numerically, except in special cases that do not apply to the samples studied here. Once Ψ_1 and Ψ_2 are known, the barrier heights may be calculated as

$$q\Phi_{B1\rightarrow 2} = (E_{v1} - E_{f1}) + \Psi_1$$
$$q\Phi_{B2\rightarrow 1} = \Delta E_{v1\rightarrow 2} + (E_{v2} - E_{f2}) - \Psi_2 + qV_{bias}.$$

Figure 4.9 (b) shows the modeled valence band diagram of the abrupt heterointerface for the heavily doped case under various levels of bias. Current density in both directions is calculated via the thermionic emission equation

$$J_{thermionic} = A^{**}T^2 \exp\!\left(\frac{-q\Phi_B(V)}{kT}\right),$$

125
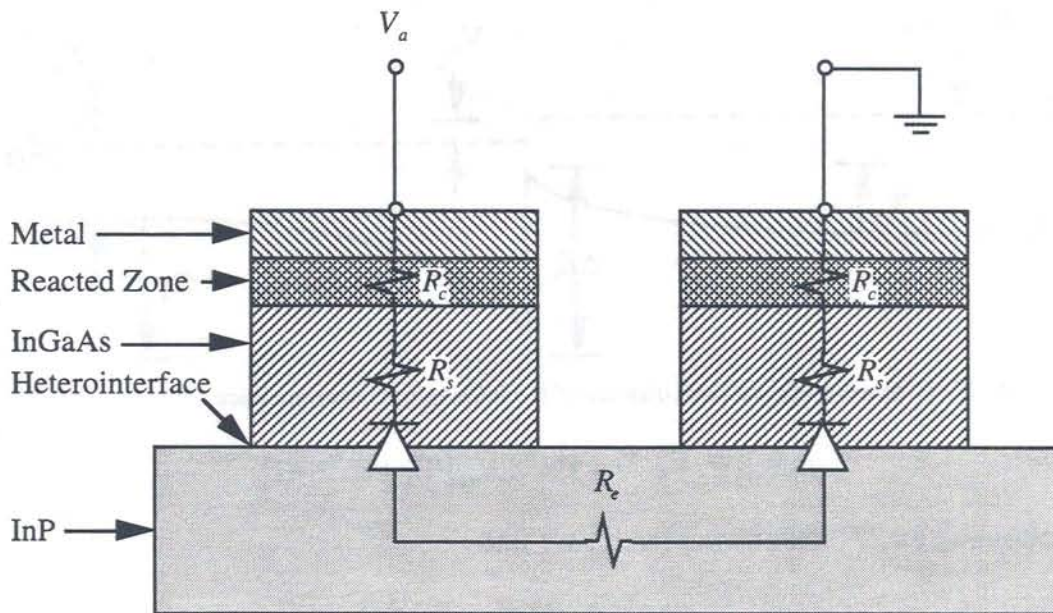
Figure 4.12   ITLM electrical model. R_c is the contact resistance between metal and InGaAs. R_s is the total resistance of the InGaAs layer. R_e is the resistance of the InP between contacts. All of the labeled interface and layer resistances, except those of the diodes, are assumed to be negligible. The current density is calculated for each level of applied bias. When $R_e = 0$, then $\partial V_{bias}/\partial J$ corresponds to the measured TLM r_i.

where A^{**} is the modified Richardson constant and is given by [26] $A^{**} = 120(m_{lh}^* + m_{hh}^*)/m_0$ $[A/cm^2/K^2]$. The calculated barrier heights at zero bias are given in Table 4.2.

The forward and reverse current densities are added at each level of bias to compute the diode-like J-V characteristic of the heterojunction. Finally, these curves are used to model the electrical characteristics of the TLM structure. Figure 4.12 shows the electrical model superimposed on a schematic of the ITLM structure. The calculated results are given in Table 4.2, where we have assumed that the actual voltage drop across the reverse biased heterointerface is less than 100 mV. We find good agreement in all three cases. The differences between the calculated and

126

measured values can be attributed to uncertainties in doping or barrier height. For example, according to the model, a doping increase of a factor of five on one side of the heterojunction causes an order of magnitude decrease in r_i. On the other hand, a doping reduction by a factor of three on both sides of the heterojunction causes an order of magnitude increase in r_i. In the particular case of Sample C, where the calculated value is smaller than the measured value, we have estimated a barrier lowering of 83 meV relative to the abrupt heterojunction case based on a simple averaging of the digital alloy barrier layer, (dashed line of Figure 4.9 (c)). If an estimate of 75 meV is used, then r_i is increased by one order of magnitude. Thus, the results agree to within a very reasonable degree of accuracy.

Sample	Description	Calculated $q\Phi_B$ (0 V)	Calculated r_i [Ω-cm^2]	Measured r_i [Ω-cm^2]
A	Low/Medium doped, abrupt	341 meV	6.8×10^{-3}	2.6×10^{-3}
B	Highly doped, abrupt	202 meV	5.3×10^{-4}	1.9×10^{-4}
C	Highly doped, graded	119 meV	1.9×10^{-5}	7.4×10^{-6}

Table 4.2   Summary of calculated and measured r_i values for each sample.

In conclusion, we have examined an important source of parasitic resistance in InP/InGaAs and other heterojunction devices. We have measured the specific interface resistance, r_i, of the heterojunction between p-InGaAs and p-InP by means of a modified transmission-line model. It is found that the specific contact resistance of these structures increases dramatically when the current is forced to go through the heterointerface. The increase is most dramatic for light to medium doping on either side of the heterointerface. Higher doping reduces the increase, although it is still significant, even for very high doping levels. The effect of inserting a digitally

127

graded bandgap layer between the contact and cladding layers was also investigated. It is found that r_i drops by an order of magnitude compared to the abrupt heterojunction case for the same doping in the contact and cladding layers. The results agree with a model based on thermionic emission. Therefore, very high doping and/or grading of this heterojunction is necessary to obtain very low series resistance in detectors and lasers. These results may be of particular importance in the design of long-wavelength vertical cavity surface emitting lasers, where a large heterointerface resistance may cause non-uniform current injection and/or large device resistances, thereby increasing the lasing threshold and reducing the external quantum efficiency.

References

1. S. N. G. Chu, A. Katz, T. Boone, P. M. Thomas, V. G. Riggs, W. C. Dautremont-Smith, and W. D. Johnston, Jr., "Interfacial Microstructure and Electrical Properties of the Pt/Ti Ohmic Contact in p-In$_{0.53}$Ga$_{0.47}$As Formed by Rapid Thermal Processing," *J. Appl. Phys.*, vol. 67, pp. 3754-3760, 1990.

2. J. B. Boos and W. Kruppa, "The Addition of Ni in AuZn Gate Ohmic Contacts for InP Junction Field Effect Transistors," *J. Vac. Sci. Technol. B*, vol. 7, pp. 502-504, 1989.

3. C. E. Allevato, J. Selders, F. Schulze, and H. Beneking, "Ohmic Contacts on p-type Ga$_{0.47}$In$_{0.53}$As/InP," *Solid State Electron.*, vol. 30, pp. 1039-1042, 1987.

4. O. Oparaku, L. L. Dargan, N. M. Pearsall, and R. Hill, "Characterization of Zn/Au Back Contact to Low-Doped p-InP," *Semicond. Sci. Technol.*, vol. 5, pp. 65-68, 1990.

5. P. Auvray, A. Guivarc'h, H. L'Haridon, J. P. Mercier, and P. Henoc, "Formation Microstructure et Résistances des Contacts Au-Ge/n-GaAs, Au-Ge/n-InP, Au-Zn/p-InP et Au-Be/p-InP," *Thin Solid Films*, vol. 127, pp. 39-68, 1985.

6. H. Temkin, R. J. McCoy, V. G. Keramidas, and W. A. Bonner, "Ohmic Contacts to p-type InP Using Be-Au Metallization," *Appl. Phys. Lett.*, vol. 36, pp. 444-446, 1980.

7. V. G. Keramidas, H. Temkin, and S. Mahajan, "Ohmic Contacts to InP and InGaAsP," *Inst. Phys. Conf. Ser.*, vol. 56, pp. 293-299, 1981.

8. B. P. Segner, L. A. Koszi, H. Temkin, E. J. Flynn, L. J. P. Ketelsen, S. G. Napholtz, and G. J. Przybylek, "InP/InGaAsP Lasers with Broad Area Double Heterostructure Lasers as Back-Face Monitors," *J. Appl. Phys.*, vol. 64, pp. 3718-3721, 1988.

129

9.   D. R. Meyers, E. D. Jones, I. J. Fritz, L. R. Dawson, T. E. Zipperian, R. M. Biefeld, M. C. Smith, and J. E. Schirber, "Material Characterization of an Ion-Implantation Process for *p*-Type (InGa)As/GaAs Quantum-Well Structures," *J. Electron. Mater.*, vol. 18, pp. 465-472, 1989.

10.   J. M. Vandenberg, H. Temkin, R. A. Hamm, and M. A. DiGiuseppe, "Structural Study of Alloyed Gold Metallization Contacts on InGaAsP/InP Layers," *J. Appl. Phys.*, vol. 53, pp. 7385-7389, 1982.

11.   A. Katz, P. M Thomas, S. M. G. Chu, J. W. Lee, and W. C. Dautremont-Smith, "AuBe/p-InGaAsP Contact Formed by Rapid Thermal Processing," *J. Appl. Phys.*, vol. 66, pp. 2056-2062, 1989.

12.   R. Bruce, D. Clark, and S. Eicher, "Low Resistance Pd/Zn/Pd/Au Ohmic Contacts to *p*-Type GaAs," *J. Electron. Mater.*, Vol. 19, pp. 225-229, 1990.

13.   T. Sands, V. G. Keramidas, R. Gronsky, and J. Washburn, "Initial Stages of the Pd-GaAs Reaction: Formation and Decomposition of Ternary Phases," *Thin Solid Films*, vol. 136, pp. 105-122, 1986.

14.   A. Kobayashi, T. Sakurai, T. Hasmizume, and T. Sakata, "An Atomistic Study of the GaAs-Pd Interface," *J. Appl. Phys*, vol. 59, pp. 3448-3453, 1986.

15.   D. G. Ivey, P. Jian, W. Wan, R. Bruce, S. Eicher, and C. Blaauw, "Pd/Zn/Pd/Au Ohmic Contacts to *p*-Type InP," *J. Electron. Mater.*, vol. 20, pp. 237-246, 1991.

16.   A. Katz, "Ohmic Contacts to InP and Related Materials," from <u>Indium Phosphide and Related Materials: Processing, Technology and Devices</u> (A. Katz, Ed.), Artech House, 1992, pp. 307-335.

17.   R. Kaumanns, N. Grote, H. G. Bach, and F. Fidorra, "Simultaneous Fabrication of Very Low Resistance Ohmic Contacts to *n*-InP and *p*-InGaAs," *Inst. Phys. Conf. Ser.*, vol. 91, pp. 501-504, 1988.

130

18. S. N. G. Chu, A. Katz, T. Boone, P. M. Thomas, V. G. Riggs, W. C. Dautremont-Smith, and W. D. Johnston, Jr., "Interfacial Microstructure and Electrical Properties of the Pt/Ti Ohmic Contact in p-In$_{0.53}$Ga$_{0.47}$As Formed by Rapid Thermal Processing," *J. Appl. Phys.*, vol. 67, pp. 3754-3760, 1990.

19. A. Katz, W. C. Dautremont-Smith, S. N. G. Chu, P. M. Thomas, L. A. Koszi, J. W. Lee, V. G. Riggs, R. L. Brown, S. G. Napholtz, and J. L. Zilko, "Pt-Ti/p-In$_{0.53}$Ga$_{0.47}$As Low-resistance Nonalloyed Ohmic Contact Formed by Rapid Thermal Processing," *Appl. Phys. Lett.*, vol. 54, pp. 2306-2308, 1989.

20. A. Katz and W. C. Dautremont-Smith, "Stress Measurements of Pt/Ti/InP and Pt/Ti/SiO2/InP Systems: In Situ Measurements Through Sintering and After Rapid Thermal Processing," *J. Appl. Phys.*, vol. 67, pp. 6237-6246, 1990.

21. A. Katz, P. M. Thomas, S. N. G. Chu, W. C. Dautremont-Smith, R. G. Sobers, and S. G. Napholtz, "Pt/Ti Ohmic Contact to p^{++}-InGaAsP (1.3 μm) Formed by Rapid Thermal Processing," *J. Appl. Phys.*, vol. 67, pp. 884-889, 1990.

22. A. Katz, B. E. Weir, and W. C. Dautremont-Smith, "Au/Pt/Ti contacts to p-In$_{0.53}$Ga$_{0.47}$As and n-InP Layers Formed by a Single Metallization Common Step and Rapid Thermal Processing," *J. Appl. Phys.*, vol. 68, pp. 1123-1128, 1990.

23. W. C. Dautremont-Smith, P. A. Barnes, and J. W. Stayt, Jr., "A Nonalloyed, Low Specific Resistance Ohmic Contact to n-InP," *J. Vac. Sci Technol. B*, vol. 2, pp. 620-625, 1984.

24. J. G. Wasserbauer, J. E. Bowers, M. J. Hafich, P. Silvestre, L. M. Woods, and G. Y. Robinson, "Specific Contact Resistivity of InGaAs/InP p-Isotype Heterojunctions," *Electron. Lett.*, vol. 28, pp. 1568-1569, 1992.

25. P. Silvestre, M. J. Hafich, T. Vogt, A. Nanda, G. Y. Robinson, J. J. Dudley, J. E. Bowers, K. M. Jones, and M. M. Al Jassim, "Gas-Source Molecular-Beam

Epitaxial Growth of InGaAsP for 1.3-µm Distributed Bragg Reflectors," *J. Vac. Sci. Technol. B*, vol. 10, pp. 956-958, 1992.

26.   S. M. Sze, <u>Physics of Semiconductor Devices</u>, John Wiley & Sons, 1981, pp. 256-257.

Chapter 5

Measurements and Results

5.1 Parasitics

Of the three extrinsic device structures studied, by far the best threshold, leakage and output power belong to the CMBH. We now examine the dynamic characteristics of this structure.

In an effort to determine the location of the parasitic capacitance and resistance of the CMBH a series of devices were made with mesa widths of 5, 10 and 20 μm. All devices were fabricated from the same wafer and had a cavity length of 304 μm. The lasers were mounted and bonded for high-speed testing. S_{11} parameter measurements were made on a network analyzer. Using an *LCR* model [1], the device parasitics were extracted from fitted S_{11} parameter measurements using Touchstone™ circuit modelling software. The measured and fitted impedance of a CMBH laser under forward bias is shown in Figure 5.1. It was found that all three devices were inductance limited and that an exact determination of the parasitic capacitance could not be made. However, an upper limit of 1 pF gave the best fit to data in all cases. From this result we conclude that the parasitic capacitance is relatively insensitive to mesa width even for the case of reverse biased *p-n* blocking layers. This, in turn, implies that the major source of the parasitic capacitance is close to the junction. This can be explained by the narrowing of the blocking layers as they approach the junction (see Figure 3.3), resulting in an increased capacitance closer to the active layer. Furthermore, the capacitance of the blocking layers is resistively

133
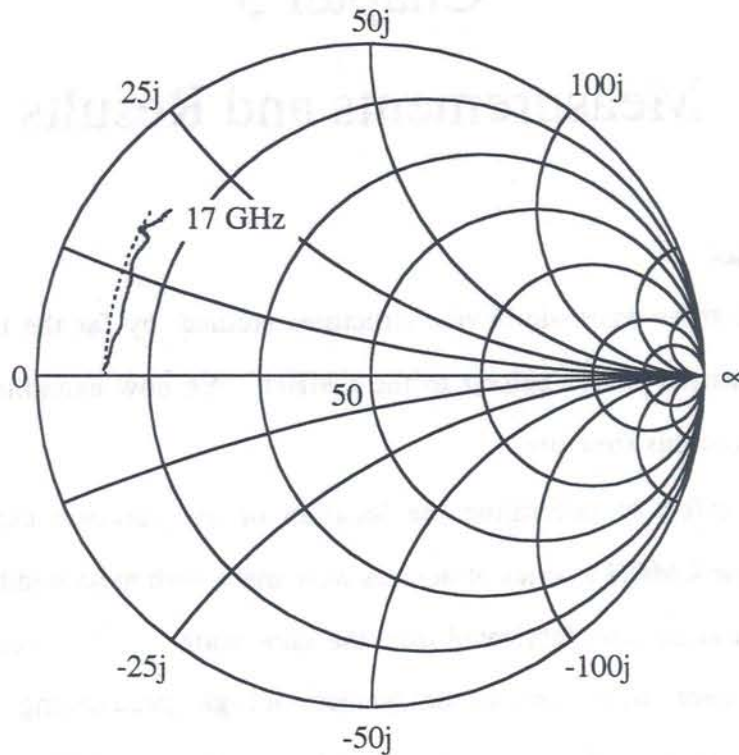
Figure 5.1   Measured (solid line) and fitted (dotted line) impedance of a CMBH laser under 50 mA forward bias.

decoupled and decreases with distance from the active area. The non-uniformity of the layers and distributed nature of the capacitance makes it difficult to theoretically predict the total parasitic capacitance of the device and its frequency dependence. Nevertheless, parasitic capacitances below about 1 pF were achieved.

Resistance measurements were also made for various device widths. The results are shown in Figure 5.2. The dashed line shows a least squares fit of the form $R = R_L/L + r_c/Lw$. The diode resistance R_L is 0.19 Ω-cm and r_c is calculated to be 1.2×10^{-5} Ω-cm^2. These are reasonable values for the particular devices at hand and indicate that the contact resistance is only a small fraction of the total parasitic device resistance. Therefore, other resistances throughout the structure must be addressed if
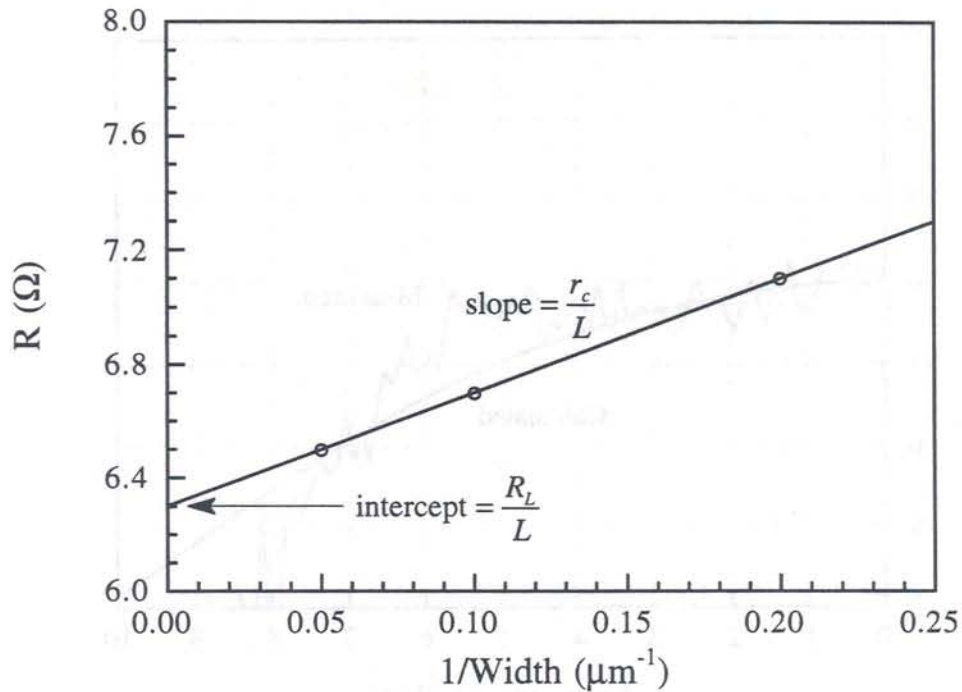
Figure 5.2   Dependence of diode resistance on inverse mesa width for cavity lengths of 304 μm, Wafer #1981-1. The diode line resistance may be calculated from the y-intercept. The specific contact resistance, including heterointerface resistance, may be calculated from the slope.

the total parasitic resistance is to be reduced. The total parasitic resistance of a 5 - 10 μm wide mesa CMBH was between 3 and 6 Ω.

The aforementioned parasitic values are low enough to increase the parasitic-limited 3 dB bandwidth to above 20 GHz. As we shall see in the rest of this chapter, this allows us to observe other dynamic limitations, such as carrier transport effects.

5.2   Transport Limited Modulation Bandwidth

Carrier transport effects may be divided into two groups: low-frequency rolloff due to transport through undoped layers, limited resonance frequency due to a reduction in the effective differential gain from thermionic emission of carriers, and

135
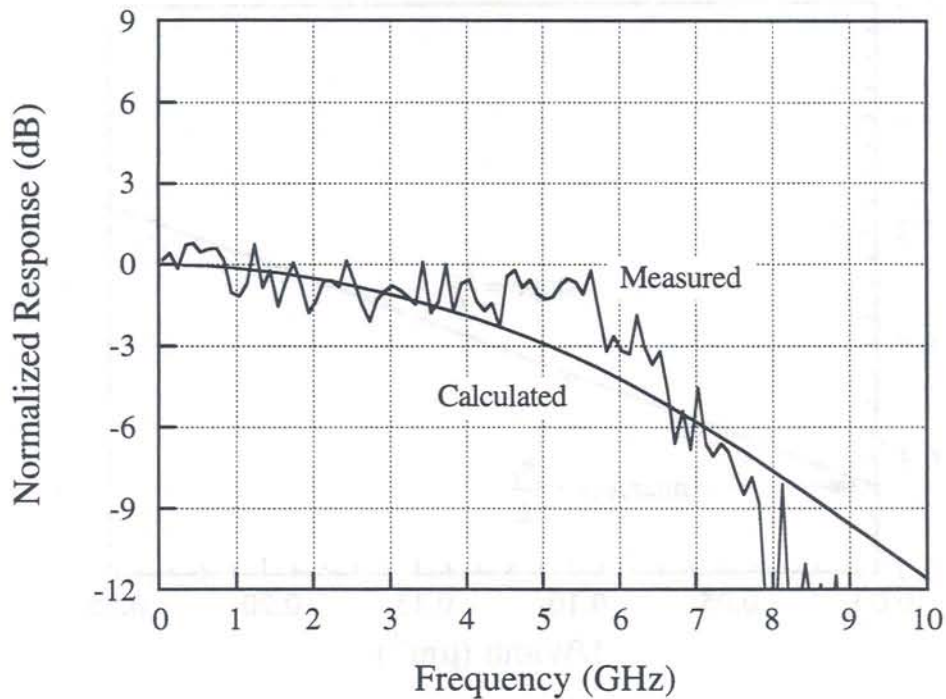
Figure 5.3 (a) Frequency response of Laser A. Low frequency rolloff is observed due to hole
transport through 180 nm undoped layer. Measured and calculated data correspond to
an output power of 24 mW.

limited resonance frequency due to a reduction in the effective differential gain from
non-uniform injection. We have observed at least two types of transport limits in this
study. We first examine the effects of carrier transport through undoped layers, and
then turn to resonance frequency limiting transport effects.

During the early phase of this work, it was found that controlling the location
and amount of the p-type dopants was critical to achieving low-threshold, high-speed
and even lasing itself [2]. In particular, p-type dopants in the active area from either
modulation or proximity doping were found to be detrimental to device performance.
Because of this, most of the lasers fabricated in this work contain nominally undoped
active areas. The primary p-type dopant used was Zn, which has a large diffusion

136
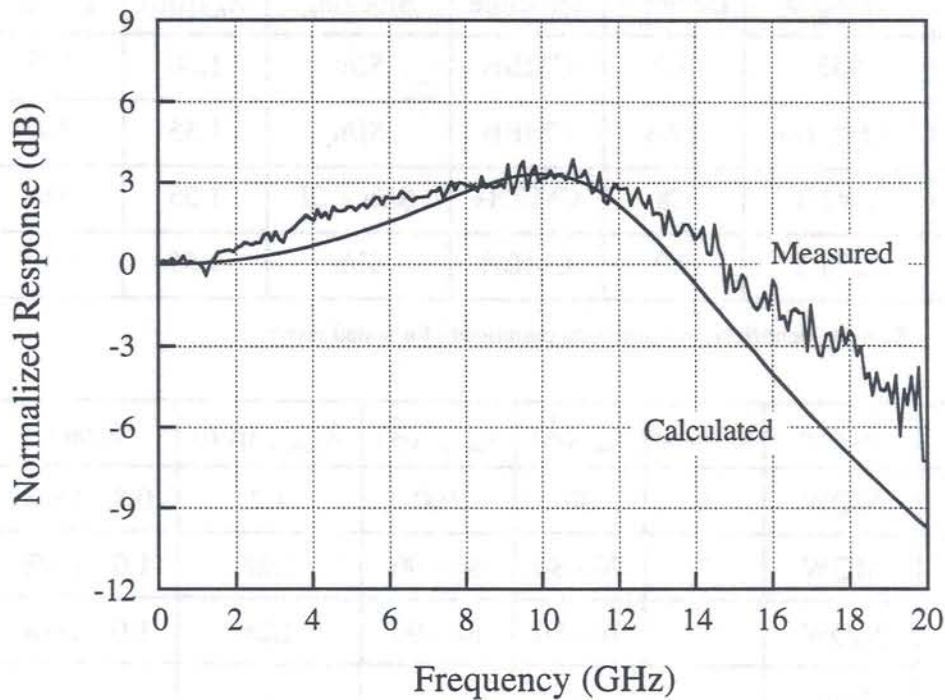
Figure 5.3 (b) Frequency response of Laser B. Resonance frequency limit due to thermionic emission and/or non-uniform injection of carriers leading to a reduction in the effective differential gain. The calculation was made for an output power of 32 mW. The measured data was taken at an output power of 40 mW.

coefficient in InP. In order to avoid doping the active area via Zn diffusion, an undoped InP setback layer was grown adjacent to the active area. For the case of MQW lasers, it has been found experimentally that a minimum setback layer thickness of 70 - 100 nm is necessary to avoid increasing the threshold significantly or eliminating lasing characteristics altogether [2]. It is assumed that the Zn dopants will diffuse somewhat closer to the active area during the remaining growth and regrowth steps. A SIMS analysis showed that the Zn diffuses about 20 nm closer to the active area during these steps. The remaining undoped layer width is defined as the distance between the edge of the Zn and the first quantum well.

137

Laser	Wafer #	Device #	Structure	Blocking	λ_0 (μm)	L (μm)
A	953	1.2	CMBH	SI/n	1.30	385
B	2018-1-a	17.3	CMBH	SI/n	1.55	360
C	2342-1	C8	CMBH+	SI/n + SI	1.55	310
D	2278-2	9.3	CMBH	SI/n	1.55	250

Table 5.1 (a)   Sample identifiers and structural parameters for tested lasers.

Laser	Active	# Wells	t_{well} (Å)	$t_{barrier}$ (Å)	$\lambda_{barrier}$ (μm)	Strain
A	MQW	6	30	100	1.2	0.8 - 1.0%
B	MQW	7	70 - 80	80 - 90	1.28	1.0 - 1.3%
C	MQW	7	70 - 80	80 - 90	1.28	1.0 - 1.3%
D	Bulk	-	-	-	-	-

Table 5.1 (b)   Active area structural parameters for tested lasers. Strains are compressive.

Laser	t_{SCH} (nm) @ λ_{SCH} (μm)	L_U (nm)	R_d (Ω)	C_p (pF)	L_s (nH)
A	50 @ 1.1, 50 @ 1.2	180	2.5	5.0	0.15
B	70 @ 1.28	120	5.4	<0.8	0.08
C	p-side: 70 @ 1.28 n-side: 70 undoped + 60 Zn @ 1.28	0	3.4	<1.8	0.22
D	-	50	5.6	<1.0	0.18

Table 5.1 (c)   Separate confinement heterostructure (SCH) parameters and measured device parasitics for tested lasers. L_U is the total undoped layer width from the edge of the p-doping to the edge of the active area (bulk) or the first quantum well (MQW).

Many of the early MQW laser designs used in this study have very large undoped layers. Table 5.1 lists the structural, parasitic and other measured and

138

Laser	I_{th} (mA)	P_{max} (mW)	Γ	f_{tr} (GHz)	f_{RC} (GHz)	f_{3dB} (GHz)
A	22	>32		6.9	13.3	6
B	6	44	0.11	21.8	40.0	17.0
C	12	36	0.10	-	21.8	20.0
D	10	28	0.2	92.7	26.4	11.0

Table 5.1 (d)   Static and dynamic characteristics of tested lasers. P_{max} is the maximum dc output power, Γ the optical confinement factor, f_{tr} the undoped layer transport limited bandwidth and f_{RC} the parasitic limited bandwidth.

calculated data for several of the lasers studied in this work. In one design, labeled Laser A in Table 5.1, the estimated undoped layer width, L_U, including Zn diffusion is 180 nm. The corresponding cutoff frequency for transport through this layer is 6.9 GHz. The actual frequency response of Laser A is reproduced as Figure 5.3 (a). Laser A was found to have a 3 dB bandwidth of 6 GHz. The parasitic limited bandwidth calculated from the measured parameters of Table 5.1 (c) is 13.3 GHz, nearly twice that of the transport limit. We conclude that Laser A is limited by transport through the undoped setback layer.

Using the structural data of Table 5.1 (a) and (b) the MQW rate equation analysis of Chapter 2 was used to predict the frequency response of this laser. The results, displayed in Figure 5.3 (a), agree well with the actual measured frequency response of Laser A. The gain compression factor in the calculation was arbitrarily taken to be 1×10^{-17} cm^{-3}. Due to these and other similar results, later designs incorporated much thinner undoped setback layers. Because of this, the undoped layer transport limited bandwidth was increased beyond 22 GHz.

In the second type of transport, thermionic emission from the wells and/or non-uniform current injection into the wells causes a reduction in the effective differential gain, effectively limiting the resonance frequencies that can be obtained. Since both thermionic emission and non-uniform carrier injection are manifest in a reduction of the effective differential gain, it is difficult to distinguish between the two in a practical device. An example of a resonance frequency limited laser is listed as Laser B in Table 5.1. The frequency response of this laser at the output power for maximum bandwidth, 40 mW, is shown in Figure 5.3 (b). Increasing the output power beyond 40 mW had little effect on the shape of the frequency response and did not improve the 3 dB bandwidth at all. A MQW rate-equation analysis was made for this laser as was done for Laser A. The calculated frequency response is also displayed in Figure 5.3 (b). There is good general agreement between the calculated and measured frequency responses. Since the model takes both transport processes into account, we may conclude that one or both of these physical processes is limiting the resonance frequency of this laser.

To summarize, we have demonstrated a highly optimized MQW laser design with undoped active area and SCH regions with a 3 dB bandwidth of 17 GHz. This is the highest reported value to date for an undoped, MQW laser operating at 1.55 μm. Further, we have shown that this laser is limited by carrier transport effects and not electrical parasitics. A solution to the problems of undoped layer transport and non-uniform current injection is presented in the next section.

5.3 Active Area Doping

As we have discussed in Chapter 2, doping can decrease the deleterious effects of carrier transport in MQW devices. However, doping can have a detrimental
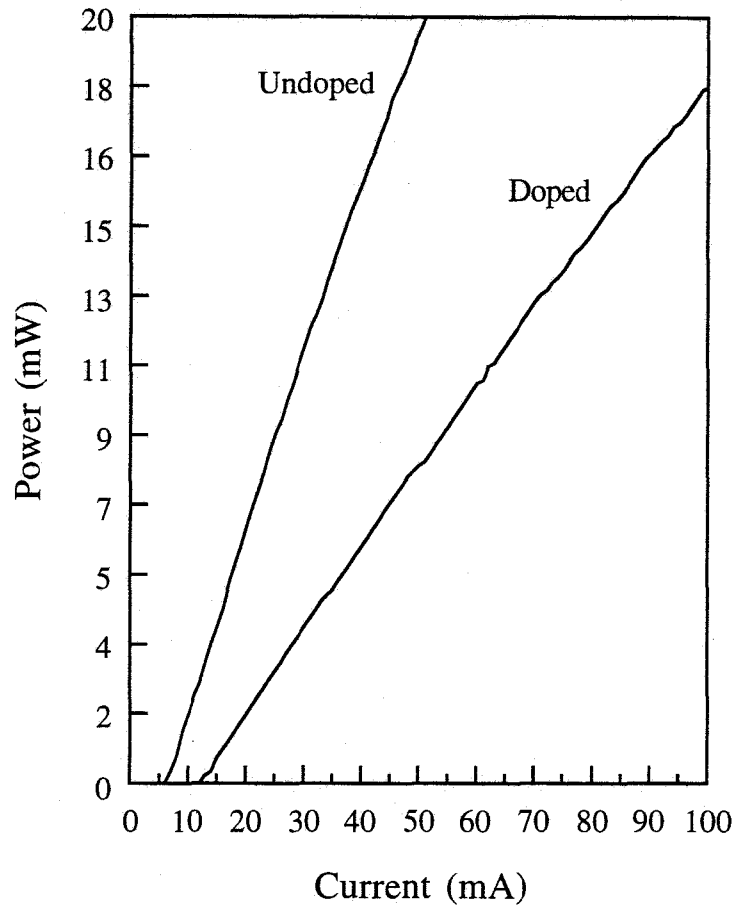
Figure 5.4   Variation of output power with dc drive current for doped and undoped MQW lasers.

effect on the threshold current, the external quantum efficiency and the maximum

output power as well. The lasers fabricated in this study often failed to lase when Zn

was placed less than 70 nm from the active area [2]. The solution, it was discovered,

was to dope the active area *uniformly*, that is, to introduce the same level of dopants

everywhere. Although this does degrade the static characteristics somewhat, the

overall static performance remains high and the dynamic performance improves

greatly. The reason why uniform doping succeeds where proximity or modulation

doping fails is not clear and will require further study.

141
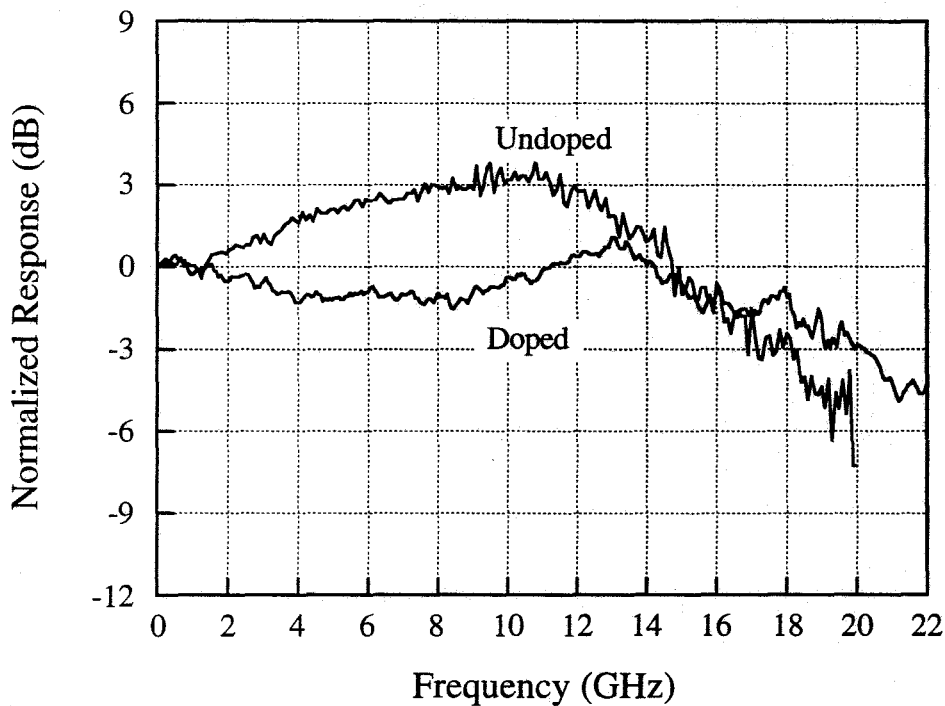
Figure 5.5   Normalized modulation response for doped and undoped MQW lasers. The 3 dB

bandwidths are 20 and 17 GHz for the doped and undoped lasers, respectively.

We now compare two MQW lasers: one with a nominally undoped active

area and one with a uniform p-doping of 1×10^{18} cm^{-3}. These are labeled in Table 5.1

as Lasers B and C, respectively. The doped laser was provided by Dr. Paul Morton of

AT&T Bell Laboratories. Figure 5.4 shows the dc P-I curves for both samples.

Both samples show excellent linearity and external quantum efficiency. The

threshold of the undoped laser is 6 mA, while that of the doped laser is 12 mA. The

increased threshold is due to a shorter carrier lifetime. The decrease in external

quantum efficiency is due to higher internal loss resulting from increased free carrier

absorption. Both samples had maximum output powers of greater than 32 mW.

Figure 5.5 shows the modulation bandwidth of doped and undoped MQW lasers. The

undoped laser has a maximum modulation bandwidth of 17 GHz, whereas the doped
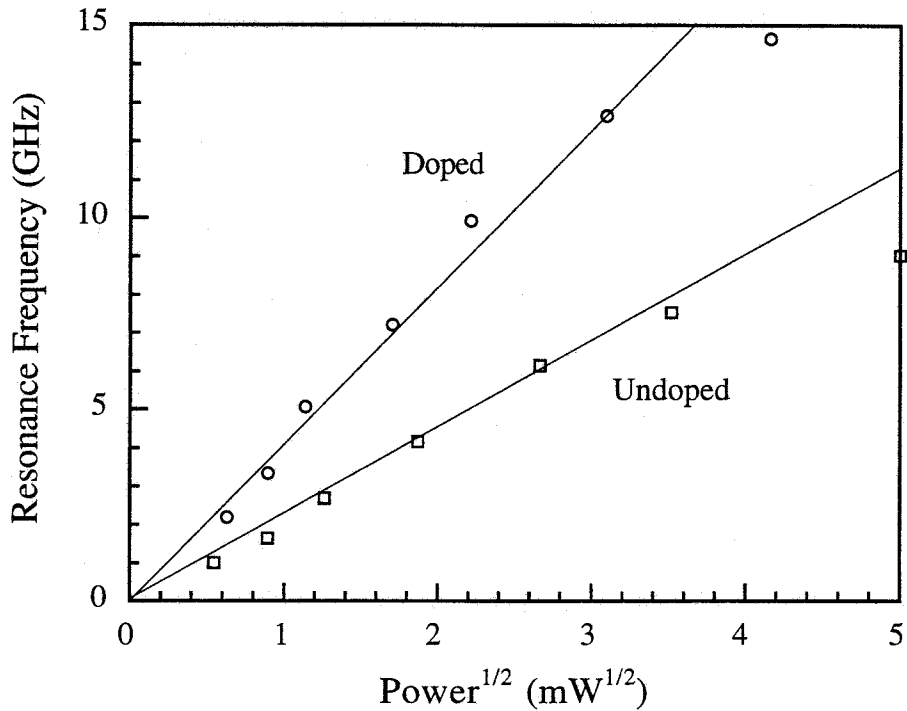
Figure 5.6   Variation of resonance frequency with square root of optical power for doped and
undoped MQW lasers.

laser has a maximum modulation bandwidth of 20 GHz. Figure 5.6 is a plot of f_r vs.

$\sqrt{P}$ for both lasers. A linear dependence of f_r on $\sqrt{P}$ is observed. The slope of the

line is a figure of merit for high speed lasers and is proportional to the differential

gain. The slope of the undoped sample is 2.18 GHz/mW$^{1/2}$, whereas that of the doped

sample is 4.32 GHz/mW$^{1/2}$. We conclude that the differential gain is about twice as

high for the doped laser as for the undoped laser. This, in turn, implies that it is

operating at a lower carrier density than the undoped laser, as expected from the

"symmetrization" of the carrier densities, (see Section 2.10).

From these results it is evident that p-doping of the active area provides two

distinct benefits: the negative effects of carrier transport are reduced and the

differential gain is increased. Therefore, appropriate *p*-doping of the active area is essential for the optimization of high-speed lasers.

5.4 Cavity Length

In Chapter 2 a model was presented which showed that the differences in optimum cavity length for maximum modulation bandwidth between bulk and MQW lasers stemmed from the differences in the gain vs. carrier density (or equivalently gain vs. current density) characteristics. The difference in the nature of the gain curves manifests itself in several different ways. First and foremost, the threshold current is a sensitive function of gain. Moreover, maximum modulation bandwidth is an extremely sensitive function of threshold current, both directly through the resonance frequency and indirectly through leakage currents and thermal effects. Thus, accurate threshold data must be input to the model to be able to predict optimum cavity length. The threshold data for bulk and MQW CMBH lasers is shown in Figure 5.7.

Secondly, the shape of the gain curve determines the differential gain, which is proportional to the resonance frequency. Although this has a much smaller effect than the threshold current, it is significant because for MQW lasers the differential gain is made more sensitive to the threshold carrier density and thus the cavity length. As we have seen in Chapter 2, the differential gain for MQW lasers is expected to be higher for lower carrier densities and longer cavity lengths.

To illustrate the effect of device length on modulation bandwidth, bulk and MQW devices of various lengths were measured. In Figure 5.8 (a) the maximum modulation bandwidth curves for the bulk lasers are reproduced, while in Figure 5.8 (b) the 3 dB bandwidth points are plotted against cavity length. The same data for
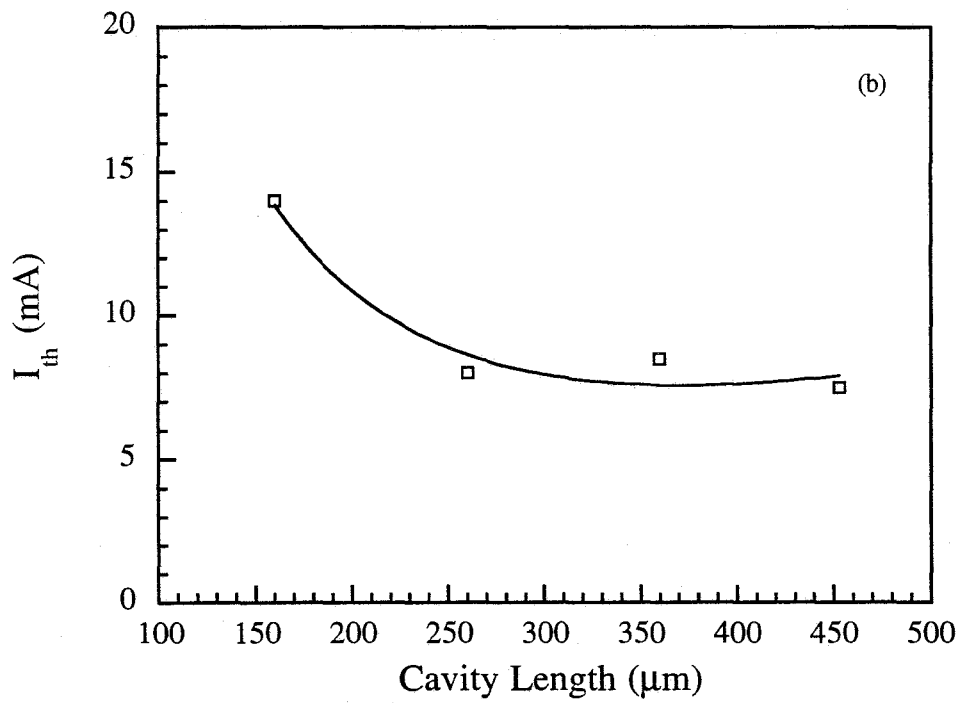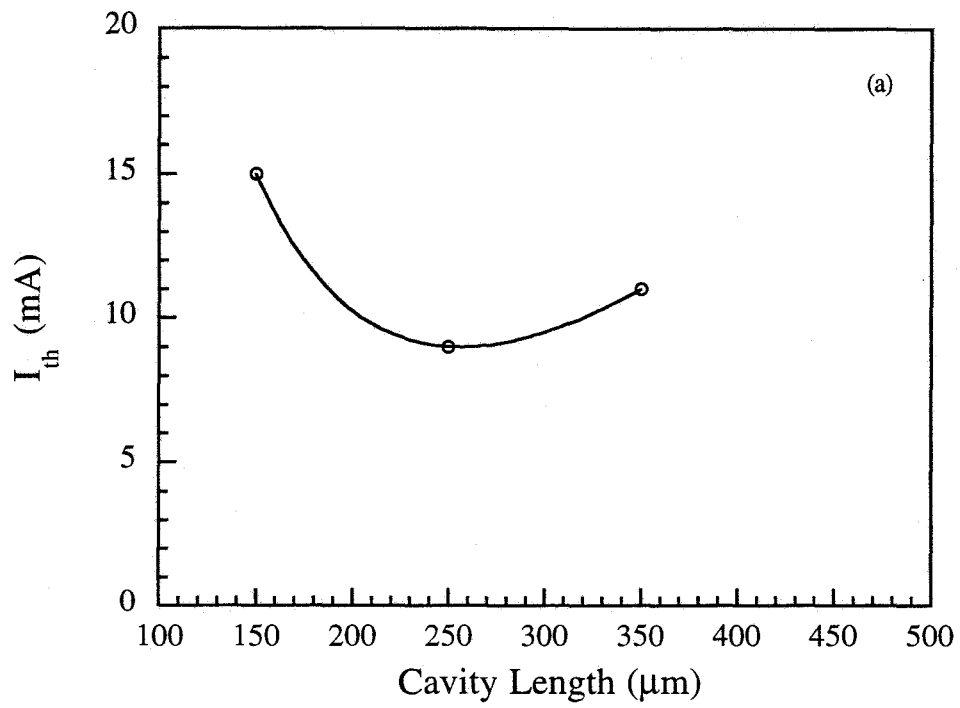
Figure 5.7   Variation of threshold current with cavity length for (a) bulk and (b) MQW lasers.

Open data points represent measured data. Solid lines represent interpolation.

145
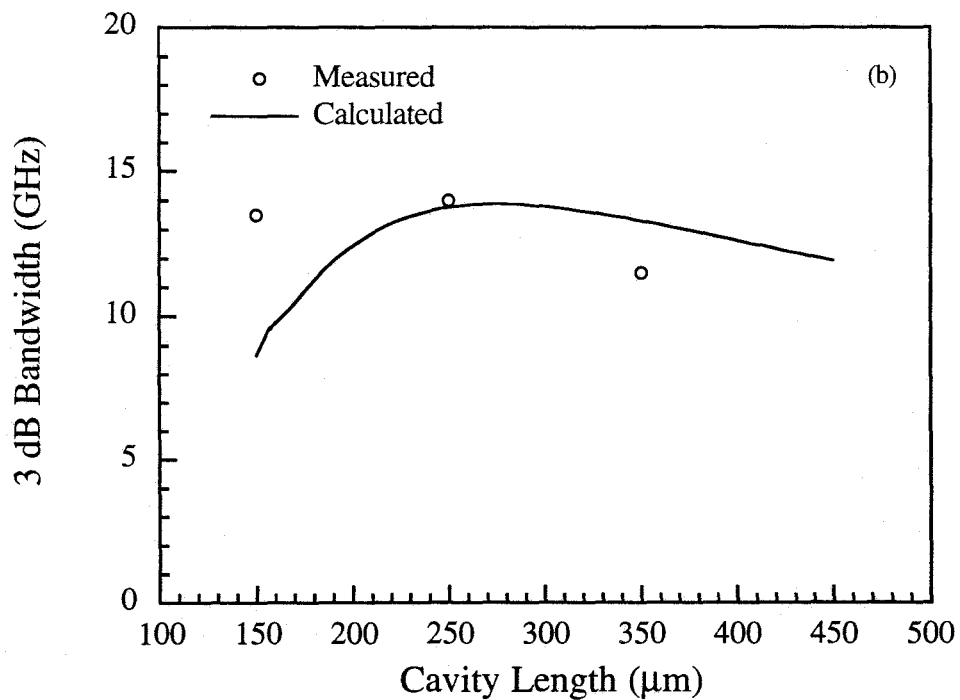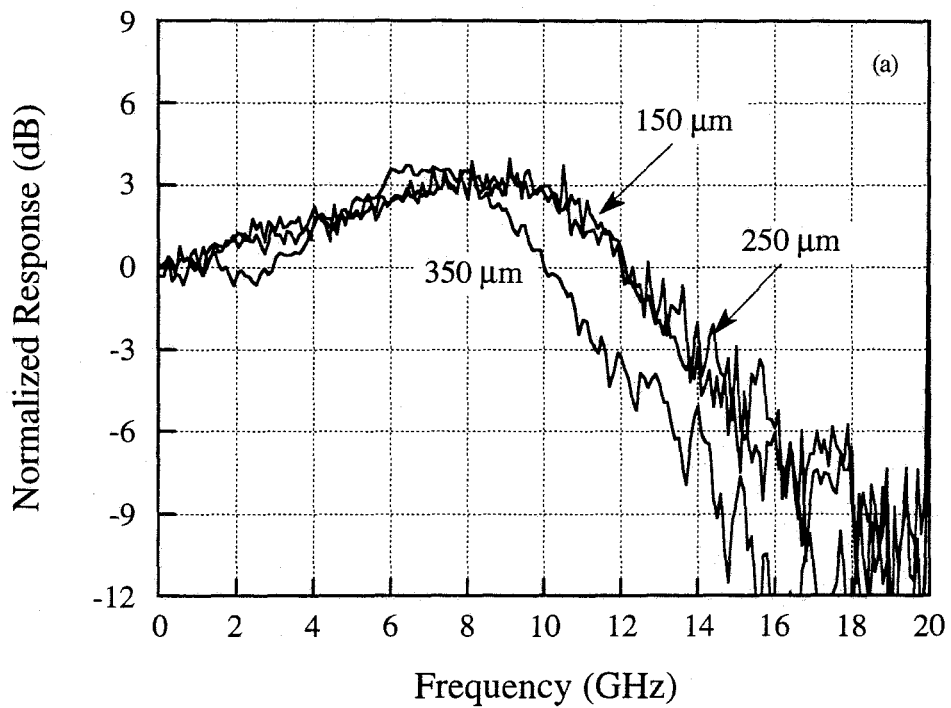
Figure 5.8   Modulation results from bulk wafer #2278-2.1b. (a) Maximum modulation responses

for devices of various cavity lengths. (b) 3 dB modulation bandwidth vs. cavity length.

146
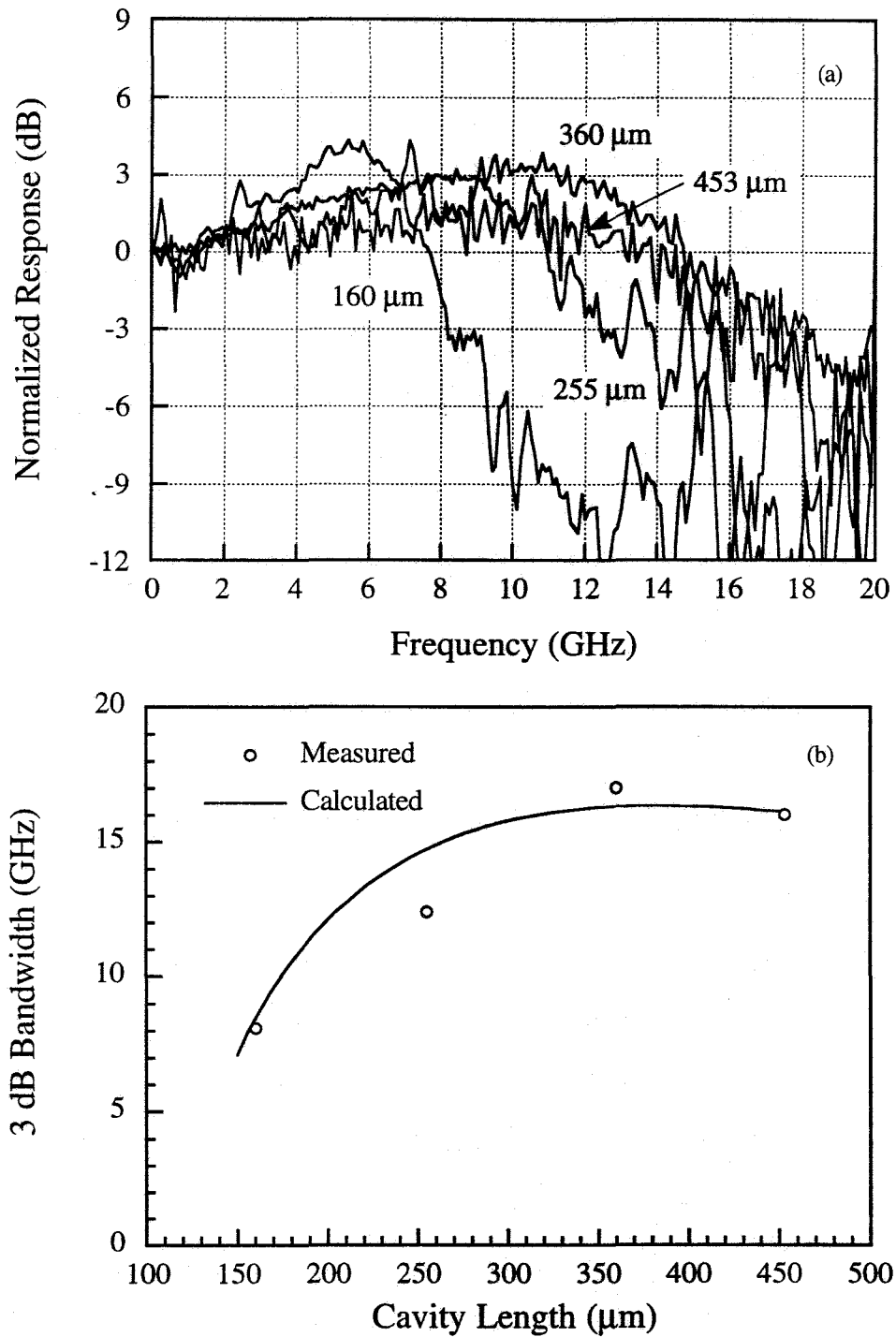
Figure 5.9   Modulation results from MQW wafer #2018-1-a. (a) Maximum modulation responses

for devices of various cavity lengths. (b) 3 dB modulation bandwidth vs. cavity length.

147

the MQW samples are presented in Figure 5.9. A comparison of the figures reveals tha the maximum modulation bandwidth, $f_{3dB\,max}$, for MQW lasers occurs at longer cavity lengths than it does for bulk lasers.

The solid curves in Figures 5.7 (b) and 5.8 (b) are theoretical calculations based on the model of Chapter 2. The threshold data for each laser structure has been interpolated in the range $L = 150$ to 450 μm and the interpolation used to calculate the device threshold in the model. For the bulk lasers of Figure 5.8 (b), the model predicts an optimum cavity length of 250 μm. $f_{3dB\,max}$ for the measured data occurs between 150 and 250 μm. For the MQW lasers of Figure 5.9 (b), the calculated bandwidth dependence on length agrees well with the measured data, with the optimum cavity length for both occurring around 350 μm. It is interesting to note how closely the maximum in the bandwidth coincides with the minimum in the threshold current as a function of cavity length. This leads to the conclusion that threshold current is the dominant factor in the cavity length dependence of f_{3dB}.

5.5 MQW vs. Bulk Active Area

Parasitics and other extrinsic limitations aside, achieving high modulation bandwidth in semiconductor lasers depends heavily on the design of the active area. A major goal of this work is to determine which active area structure, bulk or MQW, is likely to yield the greatest modulation bandwidth. Although predicted to have much higher differential gain than bulk lasers, MQW lasers have suffered from a host of other limitations to high-speed modulation, as discussed in Chapter 2 and shown in previous sections. Only recently, with a deeper understanding of these limitations, have quantum well lasers begun to fulfill their promise.
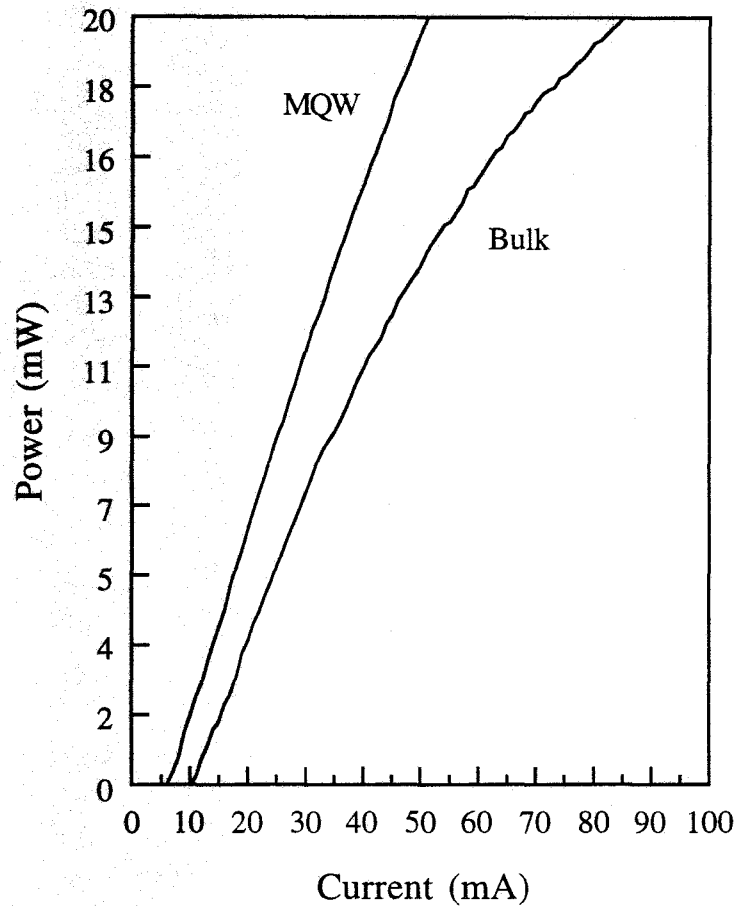
Figure 5.10   Variation of output power with dc drive current for bulk and MQW lasers.

In order to make a direct comparison between bulk and quantum well active areas, two sets of devices were fabricated. The extrinsic transverse and lateral structures were made as similar as possible. The cavity lengths were optimized separately as discussed in the previous section. Both wafers employed SI/n blocking layers and had mesa widths of 5 µm. The cavity lengths were 250 and 355 µm for the bulk and MQW devices, respectively. The P-I curves for both samples are plotted in Figure 5.10. As expected, the MQW laser exhibited lower threshold and higher external quantum efficiency. This can be attributed to more symmetric, non-
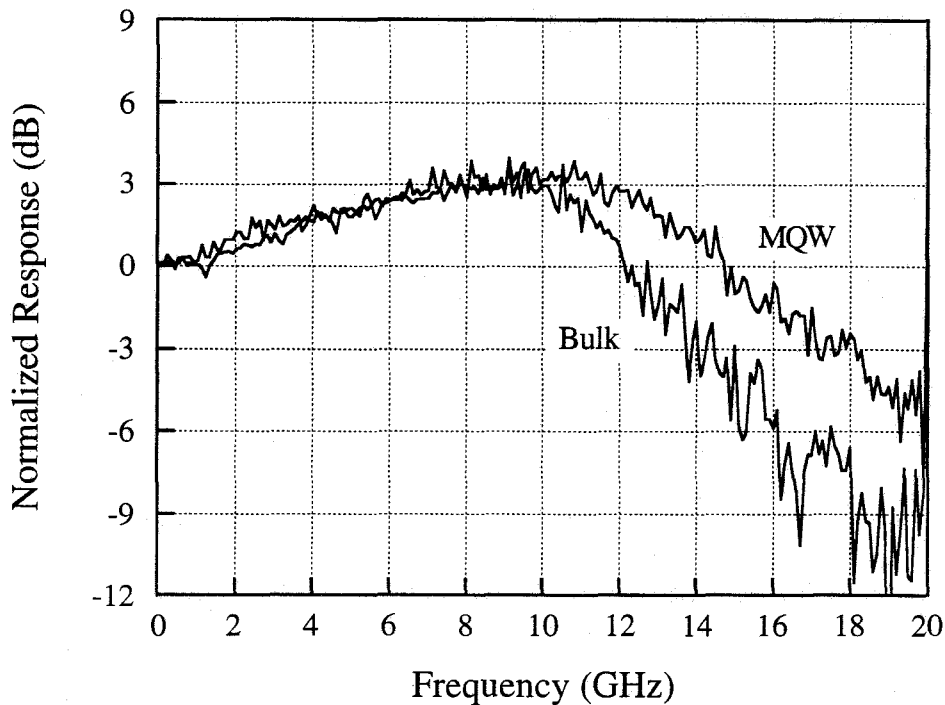
Figure 5.11　Direct comparison of modulation bandwidths of cavity length optimized bulk and MQW lasers. $L_{bulk} = 250 \, \mu m$. $L_{MQW} = 355 \, \mu m$.

degenerate energy bands, and lower internal loss, respectively. The modulation responses of both lasers for the case of largest 3 dB bandwidth are shown in Figure 5.11. The maximum modulation bandwidths, $f_{3dB\,max}$, were measured to be 14 and 17 GHz for the bulk and MQW structures, respectively. In Figure 5.12 the resonance frequency is plotted as a function of the square root of the output power. The slope was measured to be 1.85 and 2.18 $GHz/mW^{1/2}$ for bulk and MQW lasers, respectively, indicating a slightly higher differential gain for the MQW structure.

From the observed increase in modulation bandwidth for the MQW laser, one might conclude that a MQW laser is inherently faster than one with a bulk active area. This would not be entirely correct, however. As we have seen in the preceding

150
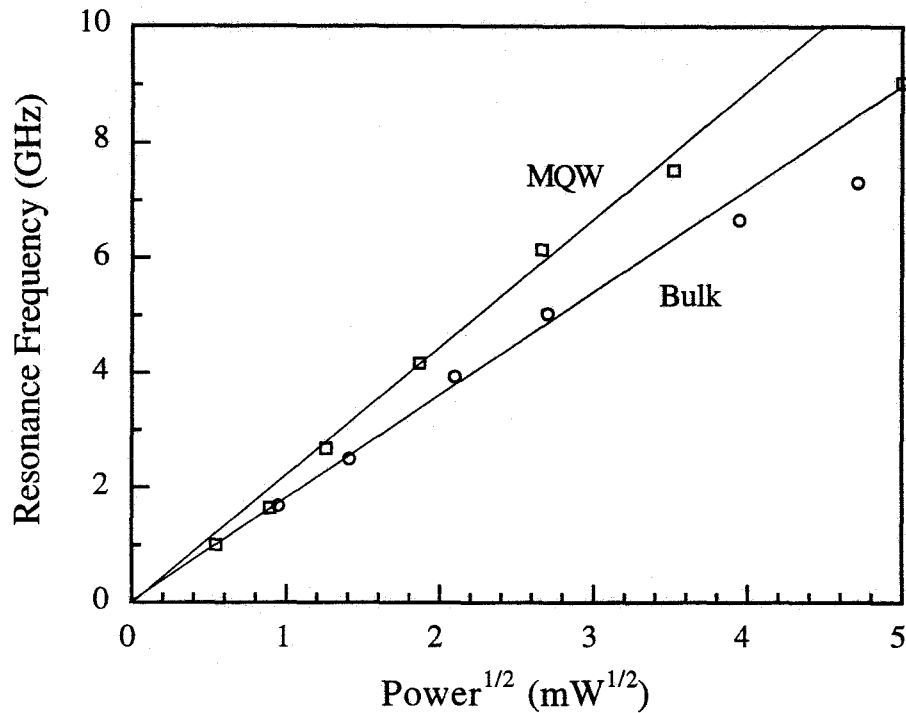
Figure 5.12   Variarion of resonance frequency with square root of optical power for bulk and MQW lasers.

section and in Chapter 2, bulk and MQW lasers must be optimized separately. It may be possible, through doping of the active area, different cavity lengths or even different base structures to optimize a bulk laser to the point where its bandwidth exceeds that of the MQW lasers presented here. Nonetheless, MQW lasers are *potentially* faster than bulk lasers due to their inherent advantages with respect to threshold and differential gain. Realizing this advantage, however, may be difficult due to the many drawbacks encountered with quantum wells.

The comparison made here indicates that strained quantum well lasers do offer a slight performance advantage over bulk lasers. However, at least for the InGaAsP/InP material system, the difference is not great. At present, the difference

between the world's record bulk and MQW devices is only 1 GHz [3, 4]. A clearer indication of a difference between bulk and quantum well structures may await a materials system with more favorable electronic properties, improved growth and regrowth techniques, or better technology for overcoming the drawbacks of quantum well structures.

References

1.   K. Y. Lau and A. Yariv, <u>Lightwave Communications Technology</u> (W. T. Tsang, Ed.), Academic Press, New York, 1985, pp. 70-152.

2.   Private communication with Dr. Tawee Tanbun-Ek, AT&T Bell Laboratories, Murray Hill, NJ, 2 February 1993.

3.   E. Meland, R. Holmstrom, J. Schlafer, R. B. Lauer, W. Powazinik, "Extremely High Frequency (24 GHz) InGaAsP Diode Lasers with Excellent Modulation Efficiency," *Electron. Lett.*, vol. 26, pp. 1827-1829, 1990.

4.   P. A. Morton, R. A. Logan, T. Tanbun-Ek, P. F. Sciortino Jr., A. M. Sergent, R. K. Montgomery, and B. T. Lee, "25 GHz Bandwidth 1.55 μm GaInAsP *p*-Doped Strained Multiquantum-Well Lasers," *Electron. Lett.*, vol. 28, pp. 2156-2157, 1992.

Chapter 6

Conclusion

The design and fabrication of high-speed, long wavelength lasers is a task with many parts. We have outlined a complete approach which optimizes both the extrinsic and intrinsic devices.

The important problem of minimizing parasitic resistances in order to increase the parasitic and thermal limits of high-speed device operation has been addressed. The task of finding a contact metallization compatible with the InGaAsP/InP system for the demanding operating conditions of today's high performance optoelectronic devices remains a difficult one. In contrast to GaAs and related materials, this technology is still immature, and the understanding of the contact metallurgy and carrier transport mechanisms, and the correlation between the microstructure and electrical properties are far from satisfactory. Nonetheless, the three metallization schemes presented in Chapter 4 go a long way toward meeting the goals of (a) very low contact resistance, (b) long term microstructure stability over a wide temperature range, (c) structural integrity over the operating range of the device, and (d) ability to form an integral part of a robust, reproducible fabrication process. AuBe provides the best results for long-wavelength materials, such as InGaAsP (λ = 1.14 μm). Pd/Zn works well for narrower bandgap materials, such as InGaAs, where the doping level is below 1×10^{19} cm^{-3}, and also provides excellent reproducibility. Ti/Pt is the preferred metallization for InGaAs contact layers containing doping in excess of 1×10^{19} cm^{-3}. A more detailed understanding of as well as atomic level control over

the nature of the metal/InP-based interfaces is required for further advances in this field.

A potentially important source of resistance, which has been generally overlooked until recently, is the interfacial resistance due to the p-isotype heterobarrier between the narrow bandgap contact and wide bandgap cladding layers of semiconductor laser diodes. A significant barrier to hole transport is present in the InGaAs/InP system. The height and width of this barrier is dependent on the doping level on both sides of the interface and the abrupt or graded nature of the heterojunction. We have shown theoretically and experimentally that the specific interfacial resistance, r_i, can be reduced by increased doping on one or both sides of the interface, and by grading the bandgap of the junction. The carrier transport across this interface becomes increasingly important as device dimensions shrink. Grading of this interface may be necessary for the optimum performance of high-speed p-i-n photodetectors and VCSELs is to be realized.

Reducing the device parasitics requires a knowledge of their sources. We have determined that the majority of parasitic capacitance of a CMBH laser comes from regions near the active area. Further, we have found that with Ti/Pt/Au metallizations the contact resistance is a small fraction of the total device resistance. Therefore, other structural parameters must be examined in order to reduce the device resistance further. The parasitic limited bandwidth for an optimized CMBH mounted on a K-connector is 40 GHz.

We have defined a figure of merit for the optimization of lateral and transverse design parameters for high-speed operation, Γ/dwI_{th}. This figure

explicitly ignores the electrical parasitics. However, the thermal effects of parasitic resistance may be included indirectly through the threshold current factor.

A model for the longitudinal optimization of the laser has been developed that includes the temperature and cavity length dependence of the threshold current, leakage currents, the temperature and threshold dependence of the differential gain, the cavity length dependence of the device resistance, and the structural dependence of the internal loss. The gain model used in this calculation accounts for strain in the quantum wells and barriers, valence band mixing, and lineshape broadening. The model predicts different optimum cavity lengths for achieving maximum modulation bandwidth for bulk and MQW lasers. Optimum cavity lengths are predicted to be shorter for bulk than for MQW devices. The model also predicts that, as the cavity length is varied, the maximum modulation bandwidth is found near the minimum threshold current.

An important element in the discussion of carrier transport theory is the concept of transport time. An expression for the carrier transport time through multilayer undoped regions has been derived for the first time. It shows that the transport time across two layers is equivalent to the square of the sum of the square roots of the transport times across each individual layer, or

$$\tau_{tr} = (\tau_{p1}^{1/2} + \tau_{p2}^{1/2})^2.$$

The above expression reduces to the single, uniform layer case when the diffusion constants of each layer are the same. These results apply to all lasers, including all of the undoped lasers fabricated in this study, in which the undoped setback layer spans two different material compositions.

156

The theory of carrier transport as applied to long-wavelength quantum well lasers has been reviewed. The main consequences of carrier transport are (1) transport across the undoped setback layer on either side of the active are leads to a parasitic-like rolloff in the modulation response, (2) the differential gain is reduced by a factor χ, which is proportional to τ_{tr}/τ_e, the ratio of the transport across the undoped region, including the quantum well capture time, to the thermionic emission time from the well, and (3) in the presence of significant carrier transport effects, the K-factor calculated from *RIN* measurements cannot be used to predict the ultimate bandwidth of MQW lasers.

An extension of the theory to multiple quantum well systems has also been reviewed. It was shown that carrier transport can lead to nonuniform carrier distributions among the quantum wells, which can cause gain saturation in some wells and subthreshold carrier densities in others. The overall effect is to reduce the effective differential gain of a MQW system with respect to the case of uniform carrier population. As a consequence, it is necessary to optimize the design of the quantum well width, the barrier width and the barrier height simultaneously in order to promote the uniform distribution of carriers throughout the active area. The optimized parameters have been calculated to fall in the ranges given in Table 6.1.

The effect of carrier doping on the threshold carrier density, threshold current, and differential gain of bulk and quantum well lasers has been explored. Other investigators have shown that *p*-doping the active area of bulk and quantum well lasers has the following effects: (1) a reduction in the threshold carrier density, (2) a reduction in the carrier lifetime, (3) an increase in the threshold current density, (4) an increase in the internal loss, (5) an increase in the internal quantum efficiency, (6) a

157

decrease in the external quantum efficiency, and (7) an increase in the differential gain. The reduction in the threshold carrier density can be understood by examining the density of states and Fermi functions for holes and electrons in bulk and quantum well systems. For unsymmetric conduction and valence bands doping has the effect of "symmetrizing" the bands, much like the effects of biaxial strain. Consequently the threshold current density is reduced and differential gain increased. The increase in differential gain has been shown to improve the resonance frequency of both bulk and MQW lasers.

The effects of doping on carrier transport have been investigated qualitatively. The main effect of adding p-type dopants uniformly to the active area and undoped spacer layer is to reduce the hole and ambipolar transport times. For injection levels greater than the doping level, we conclude that doping has little or no effect on the well-to-well transport times. Nonetheless, uniform p-doping increases the uniformity of carrier injection. Therefore, p-type doping of the active area will improve the overall transport limited modulation bandwidth. In light of the above considerations, we predict that the ultimate high-speed laser structure will incorporate p-type doping in the active area.

From the conventional expression for resonance frequency we have determined that the ultimate high-speed laser structure will be strongly index guided in order to create the highest photon density possible. If it is a regrown structure (as opposed to mass-transported) then it will also incorporate semi-insulating, or possibly large-bandgap, blocking layers due to their reduced parasitic capacitance compared to reverse biased p-n junctions. Furthermore, it will require a structure similar to the CMBH in order to avoid the dual problems of Zn and Fe interdiffusion between p and

158

Si layers and hole injection from the *p* into the SI layer. Finally, it is not likely to contain additional *n* or *p*-type blocking layers, unless they can provide a significant improvement in linearity and maximum output power, thus offsetting the effect of increased device capacitance. The realization of any benefit from increased regrowth complexity depends heavily on the overall quality of the regrowth.

A detailed fabrication process has been developed for each of three different laser structures. The common features are the use of MOCVD for the initial epitaxial growth and the critical semi-insulating InP selective regrowth steps. Due to the demanding requirements of the regrowth step, much attention has been paid to the development of etch processes that will produce smooth, monotonic mesa profiles. Key mounting procedures and designs for the microwave testing of laser diodes have also been described.

We have demonstrated two effects of carrier transport in two different, long-wavelength, MQW lasers: low frequency rolloff due to carrier transport through thick undoped layers, and limited resonance frequency due to reduced effective differential gain. Two distinct mechanisms are potentially responsible for reduced effective differential gain: short thermionic emission time in the quantum wells or non-uniform injection of carriers. A model which incorporates all three transport mechanisms has been used to calculate the frequency response of these particular MQW structures. The results agree well with the measured frequency responses demonstrating the usefulness of transport theory in designing MQW lasers. Thus, we have demonstrated a highly optimized MQW laser design with undoped active area and SCH regions with a 3 dB bandwidth of 17 GHz. This is the highest reported

159

value to date for an undoped, MQW laser operating at 1.55 μm. Further, we have shown that this laser is limited by carrier transport effects and not electrical parasitics.

To demonstrate the effects of doping, two laser with the exact same multi-quantum well active area structure were measured. The first was grown with an undoped active area and undoped setback layer on the p side. The second incorporates a uniform doping in the active and SCH regions and no undoped setback layer. The 3 dB bandwidth of the doped laser was improved to 20 GHz, as compared to 17 GHz for the undoped laser, and was limited by the device packaging. p-doped MQW lasers similar to this have been reported with modulation bandwidths as high as 25 GHz, also limited by device packaging [1]. This is the highest bandwidth of any long-wavelength laser reported to date, bulk or MQW. With improvements in packaging technology should come further improvements in the speed of these lasers.

The variation of 3 dB bandwidth with cavity length has been demonstrated. Bulk lasers were found to have much shorter optimum cavity lengths than MQW lasers, in agreement with the model of Chapter 2. $f_{3dB\,max}$ was found near the same cavity length as the minimum in the threshold current. We conclude that the dominant factor in determining the optimum cavity length is the threshold current. Furthermore, the dominant factor in determining the threshold current is the shape of the gain function, which can be quite different between bulk and MQW lasers. Therefore, the differences in the f_{3dB} dependence on L are a result of the differences in the band structure and gain characteristics between bulk and MQW active areas.

Finally, a direct comparison between bulk and strained MQW CMBH lasers at 1.55 μm reveals that the MQW devices have slightly higher bandwidth than the bulk devices. Due to their potential for high differential gain and low threshold, the

160

ultimate bandwidth of MQW lasers may exceed those of bulk lasers by a significant margin. Currently, however, the modulation performance of both types of lasers in the InGaAsP/InP system are very similar.

Table 6.1 summarizes the attributes of a highly optimized, long-wavelength lasers. While most of the attributes are general, some only apply to the InGaAsP/InP material system, and some others only to lasers emitting at 1.55 µm.

Parameter	Attribute or Range of Values
Structure	Buried heterostructure with SI-InP/n⁺ blocking layers. Wide bandgap (e.g. InGaAlAs) blocking layers also possible.
Active Area	Multi-quantum well.
# of QWs	Undoped, 6 to 8. Doped - ?
Doping	Uniformly p-doped, $1-3 \times 10^{18}$ cm^{-3}.
t_{well}	60 - 100 Å.
λ_{well}	Quaternary, strained.
Strain in Well	>1% compressive or tensile.
$t_{barrier}$	80 - 100 Å.
$\lambda_{barrier}$	1.20 - 1.30 µm quaternary. Strain compensation - ?
p-contact metallization	Ti/Pt/Au

Table 6.1   Likely attributes of ultra-high speed lasers in InGaAsP/InP material system.

As can be seen from the table, much theoretical and experimental work remains to be done. One parameter that should be optimized both theoretically and experimentally is the number of doped quantum wells that give the best modulation performance. Much experimental data has been published for undoped wells, but due

to the reduced transport effects, the optimum number of doped wells may be very different. Further, the optimum doping should be determined both theoretically and experimentally. A theoretical treatment must consider not only aligning the quasi-Fermi levels with the edges of the bands, but also resulting changes to the carrier and photon lifetimes and the threshold.

Strain type, amount of strain, and strain compensation are all areas with much room for exploration with regard to their effect on speed performance. While preliminary studies have been done in all these areas, there is as yet no clear consensus as to what the optimum values for these parameters are.

Finally, new materials systems may hold the key to breaking the current speed barriers. In particular, a wider bandgap material such as InGaAlAs may prove useful in several device aspects. For example, the use of this material for carrier confinement in the quantum wells may increase the thermionic emission time, thus increasing the effective differential gain, as suggested by Ishikawa *et al.* [2]. It may also be placed just outside the SCH region to reduce heterobarrier leakage currents. Lastly, wide-bandgap InGaAlAs may prove very useful as a regrown blocking layer in buried heterostructures to reduce leakage currents.

In conclusion, there are many aspects of long-wavelength lasers that may be improved to obtain higher modulation bandwidths. Some theoretical and experimental methods have been presented here and still others outlined for future investigation. It is clear that research in long-wavelength, semiconductor lasers has a bright and fascinating future.

References

1.   P. A. Morton, R. A. Logan, T. Tanbun-Ek, P. F. Sciortino Jr., A. M. Sergent, R. K. Montgomery, and B. T. Lee, "25 GHz Bandwidth 1.55 μm GaInAsP *p*-Doped Strained Multiquantum-Well Lasers," *Electron. Lett.*, vol. 28, pp. 2156-2157, 1992.

2.   M. Ishikawa, R. Nagarajan, T. Fukushima, J. Wasserbauer, and J. E. Bowers, "Long Wavelength High Speed Semiconductor Lasers with Carrier Transport Effects," *J. Quantum Electron.*, vol. 28, pp. 2230-2241, 1992.

Appendix

The Transmission Line Model for Contact Resistance

A.1 Contact Resistance

The general model for ohmic contacts is illustrated in Figure A.1. It assumes that an electrically conductive semiconductor layer is sandwiched between an ohmic metallization and an insulating (or semi-insulating) substrate. This conductive layer is assumed to be thin with respect to the lateral width of the metallization, which is usually assumed to be semi-infinite. The transition layer between the metal and semiconductor has associated with it a resistance called the specific contact resistance, r_c, which is given in units of Ω-cm^2. Although the model assumes this layer to be uniform, in reality it is usually very rough for alloyed contacts. Alloyed contacts in the InGaAsP/InP system suffer from Au spiking which can extend a significant distance into the conductive layer or even go right through it. Hence, the model may seem inappropriate. Nevertheless, for a well designed contact the expressions derived from this model provide an accurate description of the observed behavior.

There are several approaches to solving for the specific contact resistance [1]. We present here perhaps the most physically intuitive model, known as the differential model. In this case the differential quantities are handled analytically. Referring to Figure A.1 we see that the current across a differential length dx is

$$I = \frac{dV}{dR},$$

164

Contact Metal

Reacted Zone

p^+ InGaAs

I_0

$I(x)$

r_c

dx

$x = 0$

Semi-Insulating InP
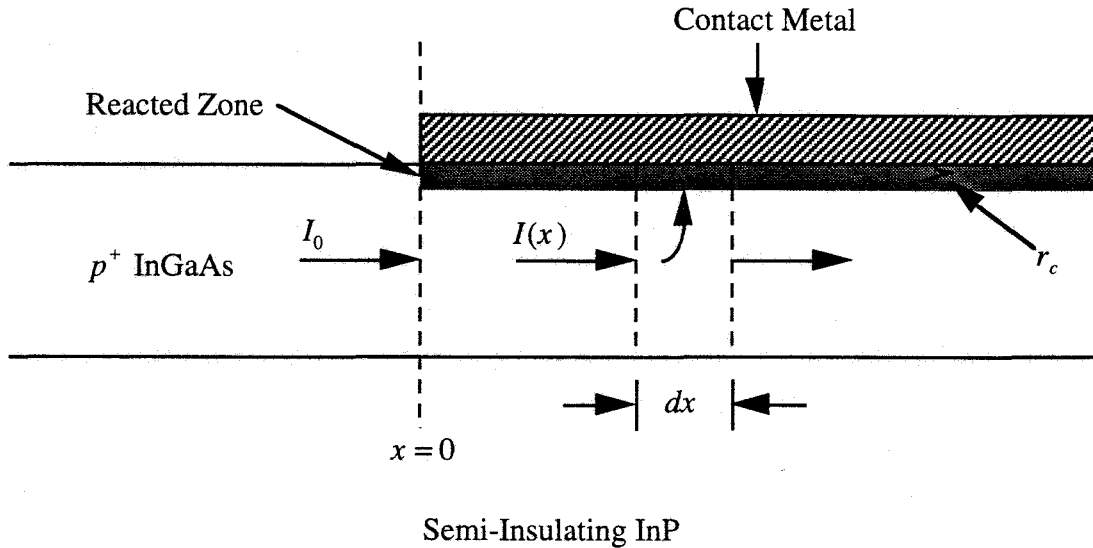
Figure A.1   Physical model for treating planar, ohmic contacts. The material under the contact is characterized by a bulk resistivity, ρ; the transition between the bulk material and the ohmic contact is characterized by the specific contact resistance, r_c. After Williams [1].

where

$$dR = \frac{R_{sc}dx}{W}.$$

R_{sc} is the sheet resistance in Ω/square of the conducting layer and W is the width of the contact. The current that flows into the contact is

$$dI = \frac{V}{(r_c/Wdx)}.$$

Combining the first three equations gives

$$\frac{r_c}{R_{sc}}\frac{d^2V}{dx^2} - V(x) = 0.$$

The general solution is

$$V(x) = c_1 e^{x/L_t} + c_2 e^{-x/L_t},$$

where

$$L_t^2 = r_c / R_{sc}.$$

Assuming a semi-infinite contact, the boundary conditions are

$$V(0) = V_0 \text{ and } V(\infty) = 0.$$

This leads to the specific solution of

$$V(x) = V_0 e^{-x/L_t}.$$

In a similar way we can obtain the current,

$$I(x) = I_0 e^{-x/L_t},$$

where $I_0 = V_0 W L_t / r_c$.

The contact resistance, R_c, is defined as V_0/I_0. Thus,

$$R_c = \frac{\sqrt{r_c R_{sc}}}{W}.$$

A.2 Measurements

It must be emphasized again that there are really two values of sheet resistance that are of interest: the sheet resistance of the InGaAs material between the ohmic contacts and the sheet resistance of the material under the ohmic contacts. Because of the alloy process, the two will not be the same. The sheet resistance between the contacts will be simply designated R_s. The sheet resistance of the material under the contact will continue to be designated R_{sc}.

The basic technique to measure contact resistance of planar ohmic contacts employs a test pattern composed of differently spaced ohmic contacts as illustrated in Figure A.2. Ohmic contacts are formed on a semiconductor surface and separated by a distance L. The contacts have a width, W, and the pattern is isolated to restrict current to flow only across the distance L. The resistance between two such contacts is the

166
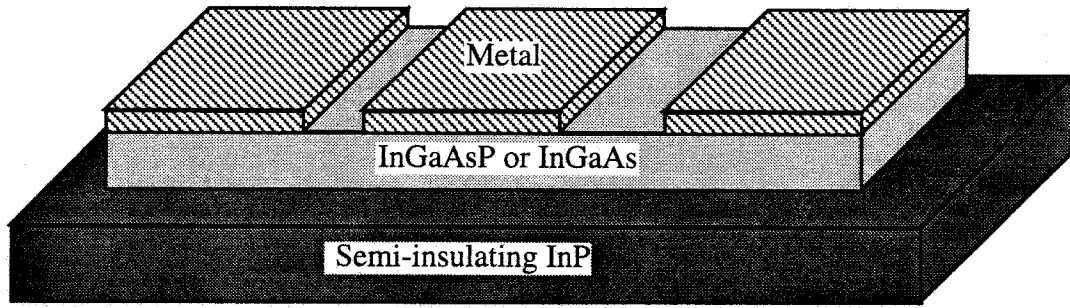
Figure A.2   Structure used for the transmission line model measurement of specific contact resistance. r_c

two contact resistances plus the resistance of the semiconductor between the two contacts,

$$R = 2R_c + \frac{R_s}{W}L$$

$$= \frac{2R_{sc}L_t}{W} + \frac{R_s}{W}L.$$

Therefore, assuming sheet resistance is constant, a plot of measured resistance as a function of spacing, L, will yield a straight line as shown in Figure A.3. The slope of the line gives R_s/W and the intercept with the R axis gives the value $2R_c$. Setting $R = 0$ we can find the L-axis intercept as

$$-L_x = \frac{2R_{sc}L_t}{R_s}.$$

In general for alloyed contacts, R_{sc} will be different from R_s. In this case an additional measurement is needed to determine R_{sc}. Technically, this information can be supplied by an appropriate "end resistance" measurement. R_{sc} can then be determined from

$$R_{sc} = \frac{R_s L_x}{2d_{end}}\sinh\left(\frac{2R_{end}W}{R_s L_x}\right),$$

where d_{end} is the finite length of the contact. But the end resistance measurement is valid only if d_{end} is not greatly larger than L_t. Note that for reasonable values of r_c

167
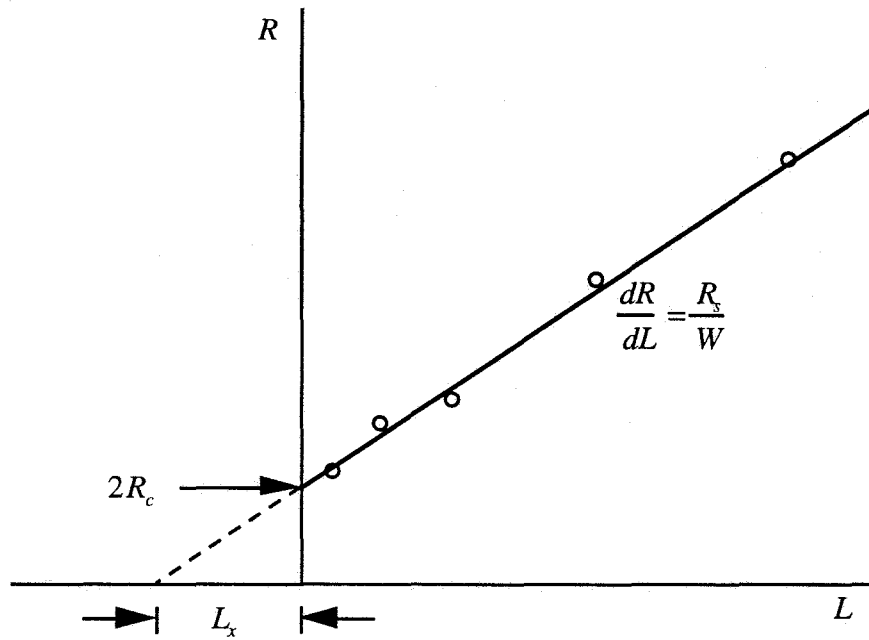
Figure A.3   A plot of measured resistance as a function of contact separation (using the test pattern

of Figure A.2) yields sheet resistance, contact resitance, and other parameters. After

Williams [1].

and R_s, the transfer length is on the order of one or two microns. Thus, for most

realistic ohmic metals, an end resistance measurement requires a prohibitively small

contact. As a practical matter, then, it is convenient to (falsely) assume $R_{sc} = R_s$,

(unless the contacts are unalloyed, in which case the assumption is valid). The L-axis

intercept then becomes

$$-L_x = 2L_t.$$

The expression for r_c then simplifies to

$$r_c = R_s L_t^2$$

$$= W \frac{R_s}{W} \left(\frac{L_x}{2} \right)^2$$

$$= \frac{W(2R_c)^2}{4(R_s/W)}.$$

168

In the last two expressions we have used quantities that may be read directly from the plot of R vs. L.

The measurement technique described above is sensitive to measurement error. Minor variations in the contact spacing will translate the line laterally, resulting in error in the calculation of both $2R_c$ and L_x. Inaccuracy in the resistance measurements or failure to subtract the probe-to-probe resistance translates the line vertically, also resulting in errors. Irregular contact edges can cause large errors in the measured resistance value, especially for narrow contact spacings. For these reasons several precautions should be taken to ensure the best possible accuracy:

1) Every spacing on every test pattern should be measured individually.

2) The test pattern should be completely isolated so that current flow is only possible between pads.

3) The contact itself should be of sufficient thickness to avoid resistive effects across the pad.

4) The test patterns should be examined individually, and those with irregular edges or obvious defects should not be used.

For some metallization schemes, the aforementioned difficulties in determining R_{sc}, coupled with experimental error, make it exceedingly difficult to determine r_c accurately using this method. In general, claims of specific contact resistances obtained from transmission line measurements of less than about 1×10^{-6} Ω-cm^2 should be examined critically.

References

1.   R. E. Williams, Gallium Arsenide Processing Techniques, Artech House, 1984, pp. 245-253.